SEARCHING FOR THE QUANTUM CHROMODYNAMIC CRITICAL POINT

A Senior Honors Thesis

Presented to

the Faculty of the Department of Physics

University of Houston

In Partial Fulfillment

of the Requirements for the Degree

Bachelor of Science

By

Debora Mroczek

April 2020

Acknowledgements

I would like to first thank my thesis advisor, Prof. Claudia Ratti. Without her kindness and devotion to her students, this work would not haven been possible. From the moment she took me into her group as a freshman, she never failed to be the mentor I needed – whether that required academic, professional, or personal advice.

I want to acknowledge Dr. Paolo Parotto, who set aside countless hours for our research meetings over the course of two years. This thesis is largely the result of our work as team, and I am thankful that I got to execute Paolo's ideas.

I would also like to thank Prof. Jacquelyn Noronha-Hostler, who has been a fantastic mentor for the last few years. I look forward to completing my Ph.D. as her student. I know there is infinitely more that I can learn from her.

Thank you, Prof. Eric Bittner, for teaching me that having fun and enjoying the process is just as important as the science itself. He also taught me a thing or two about computational quantum chemistry that may or may not have been essential to my career thus far.

I would like to acknowledge Prof. Morten Hjorth-Jensen for the months he dedicated to helping me with this work and for always reminding me to "go where [my] heart is."

Lastly, I would like to thank my cats, Chester and Luke, who are nearly co-authors in this work for the excessive amount of times they sat on my laptop keyboard, and my senior honors thesis "Accountabilibuddies" for the laughs and complete lack of accountability that resulted from our friendship.

This material is based upon work supported by the National Science Foundation under grant no. PHY-1654219 and PHY-1559866, and by the U.S. Department of Energy, Office of Science, Office of Nuclear Physics, within the framework of the Beam Energy Scan Topical (BEST) Collaboration. We also acknowledge the support from the Center of Advanced Computing and Data Systems at the University of Houston.

SEARCHING FOR THE QUANTUM CHROMODYNAMIC CRITICAL POINT

An Abstract of a Senior Honors Thesis

Presented to

the Faculty of the Department of Physics

University of Houston

In Partial Fulfillment

of the Requirements for the Degree

Bachelor of Science

By

Debora Mroczek

April 2020

Abstract

Under extreme temperature and density conditions, the quarks and gluons that are normally confined to nucleons are able to move freely in a state known as the quark-gluon plasma (QGP). Currently, droplets of QGP can be created experimentally using heavy-ion collisions at the Relativistic Heavy Ion Collider (RHIC) at Brookhaven National Laboratory and at the Large Hadron Collider (LHC) at CERN. It is known from first principle quantum chromodynamics (QCD) calculations that the transition from nuclear matter to the QGP is a crossover if the system has a net baryon density of zero, which has been consistent with experimental results. One of the key questions in the field is whether QCD exhibits a first-order phase transition at large baryon densities. In this scenario, a critical point would mark the end of the crossover phase transition and the beginning of the first order line.

In this thesis, I detail my study of the implications of the presence of a critical point on the QCD phase diagram. In the first part of this work, I construct a family of equations of state matching lattice calculations at low baryon density, and including a critical point in the correct universality class. I then employ the equation of state I developed in the analysis of a possible critical point signature that can be detected experimentally at RHIC. I also use a Feed-Forward Neural Network to identify critical point configurations that result in inconsistent thermodynamics.

Contents

List of Figures

List of Tables

Introduction

A few microseconds after the Big Bang, when temperatures reached trillions of degrees Kelvin, the universe was filled with a liquid known as the quark-gluon plasma (QGP). The QGP is made of freely moving quarks and gluons, particles that are normally confined in the form of protons and neutrons and cannot exist in an unconfined state. Currently, droplets of QGP can be created experimentally using heavy-ion collisions at the Relativistic Heavy Ion Collider (RHIC) at the Brookhaven National Laboratory. It is known from the accepted theory of strong interactions, quantum chromodynamics, or QCD, that the transition from nuclear matter to the QGP is a crossover if the system has a net baryon density of zero. So far, these predictions have been consistent with experimental results.

One of the key questions in the field is whether QCD exhibits a sharp phase transition (first-order) at large baryon densities. In this scenario, a critical point would mark the end of the crossover phase transition and the beginning of the first order line. The determination of the phase structure of QCD, along with the existence and location of its critical point, is now one of the most important goals of high-energy nuclear physics research.

Early experimental runs of heavy-ion collisions at RHIC and at the Large Hadron Collider (LHC) at CERN showed that the quark-gluon plasma behaves like a liquid with low viscosity to entropy density ratio. This means that the QGP can be precisely described by relativistic viscous hydrodynamics. These same equations of motion have significant overlap with areas in condensed matter and astrophysics. There have been increasing efforts from both theory and experiment to explain QGP dynamics.

From the theory perspective, finite lattice QCD calculations and hydrodynamic simulations of heavy-ion collisions are the best available tools to interpret and predict experimental outcomes. The phase diagram for QCD is typically given in terms of temperature and baryon chemical potential, μ_B. Although lattice QCD is a first-principle approach, it cannot be solved at finite chemical potential. That means all the information that can be extracted from lattice calculations about the QGP corresponds to the line at vanishing μ_B. Hydrodynamic simulations provide an effective way of describing the evolution of the system created in a heavy-ion collisions, but they require an Equation of State (EOS) that can close the system of equations of the system. The EOS needs to reflect all theoretical knowledge currently available. Besides, it needs to incorporate a critical point, so that its effect on experimental observables can be studied.

The first phase of the Beam Energy Scan (BES-I) program at RHIC showed hints of a first-order phase transition [1], which prompted improvements to detectors and statistics for the second phase of the program, BES-II, scheduled for 2019-2021. With results from the second phase of the Beam Energy Scan program underway over the next 5 years, it is imperative that our theoretical tools are ready to interpret the

data.

The focus of my undergraduate research, presented in this thesis, was developing methods to quantify the effects of the proposed critical point of quantum chromodynamics on the overall thermodynamic properties of heavy-ion collision systems, and to identify tools that can aid in the constraint of the location, size, and shape of the critical region.

This thesis is structured as follows:

Chapter 1 deals with the historical development of QCD as well as its Lagrangian and main features of the theory.

Chapter 2 is a summary of the experimental efforts in heavy-ion physics that resulted in the detection of the QGP. It also describes the results from BES-I that motivated this work.

Chapter 3 presents my work in developing an Equation of State for QCD that matches lattice data where applicable and also contains a critical point from the correct universality class.

Chapter 4 details the how the EOS I constructed can be applied to the study of the QCD phase diagram and the thermodynamic properties of the critical region.

Conclusions and Future Work will follow.

Chapter 1

The Big Picture: A Brief History of the Universe

1.1 A Hot Universe

In the 1920's, Hubble discovered that our universe has been expanding and cooling for approximately 10 billion years. His discovery changed every aspect of how we perceive our universe over the decades that followed. The idea of an immutable, infinite universe was replaced by that of a continuously evolving, incredibly dynamic system. One of the natural conclusions to arise from Hubble's observations is that if the universe is and has been expanding throughout its entire existence, then, at the very beginning of its history, it must have existed in a hot, extremely dense state. We now refer to this state as the Big Bang – the event that brought the universe itself and all of its contents into existence.

After Hubble's finding, the scientific community of the 1940's began developing a framework to explain the original hot, dense state that started the universe. The case for a hot early universe was solidified in 1962, with the discovery of the cosmic microwave background by Penzias and Wilson [2]. The leftover radiation from the Big Bang's heat they discovered, in turn, motivated further theoretical and experimental efforts.

1.2 Matter Under Extreme Conditions

One of the main challenges that came with looking back into the history of the universe through the study of hot and dense matter was the difficulty in limiting the quantities that our theories predict. In other words, the first question that needed to be addressed at the time was what is exactly the highest temperature that could be understood with the current theory?

In 1966, Sakharov [3] established that the absolute maximum temperature of any substance in equilibrium with radiation is of the order of Planck temperature

$$T_P = \sqrt{\frac{\hbar c^5}{Gk^2}} \approx 10^{32} K \quad (10^{22}\text{MeV}). \tag{1.1}$$

Beyond this value, gravitational interaction between photons becomes significant. However, theorists were still struggling to understand nuclear matter in the range of a few hundred MeV, so dealing with temperatures in the Planck scale was unimaginable. Our ambition to map the thermal history of the universe would have to wait

for a breakthrough in the theories of strong nuclear interaction.

At the time, there were two conflicting approaches to strongly interacting matter. The first model, called Bootstrap, [4, 5] was based on the hypothesis that hadrons are composites of one another. That is, lighter hadron species come together to form heavier hadron species. The Bootstrap model predicted that after some limiting value of temperature, referred to as the Hagedorn temperature ($T_H = 170 - 180$ MeV), any subsequent heating of the system would lead to the creation of more and more massive hadron species, but not to an increase of its temperature. The second model, the quark model [6, 7], hypothesized that hadrons are composite particles made up of smaller constituents called quarks, which would be confined inside hadrons. Some even predicted that there could be "leftover quarks" from the Big Bang roaming freely through the universe [8]. Unfortunately, the best theories on strong interaction in the 1960's were still not equipped to deal with temperatures beyond 100 MeV.

The first breakthrough came in 1973 with the discovery of the phenomenon of asymptotic freedom in the theory of elementary particle interactions by Gross, Wilzek [9], and Politzer [10]. The nobel prize-winning insight immediately motivated the study of its implications for hot and dense matter. Two groups, Collins and Perry, and Cabibbo and Parisi arrived at two distinctly fascinating predictions. Collins and Perry were the first to interpret the implications of assymptotic freedom in terms of hadrons [11]. They realized that, since the interaction between quarks weakens as the distance between them gets smaller, after a certain threshold these quarks would no longer be confined inside hadrons. They called this state superdense matter, which characterized any density above the nuclear one, and concluded that matter in a

superdense state would consist of a "quark soup." Cabibbo and Parisi went on to reinterpret this prediction in terms of a phase transition. The abstract of their work [12], published in 1975, reads

> *The exponentially increasing spectrum proposed by Hagedorn is not necessarily connected with a limiting temperature, but it is present in any system which undergoes a second order phase transition. We suggest that the observed exponential spectrum is connected to the existence of a different phase of the vacuum in which quarks are not confined.*

Though succinct, the abstract contains two groundbreaking ideas. The first is that the Hagedorn temperature is not a limit, but a *transition*. The second is that this phase transition is associated with quarks breaking free from hadrons as asymptotic freedom is approached. The realization that strongly interacting matter has different phases spurred theorists on to develop a robust theory of strong interactions and subsequently motivated the planning and construction of the largest experiments science has ever built over the 1980's. In the late 1970's, the cloudiness around the thermal history of the universe and its elementary components began to fade.

1.3 Quantum Chromodynamics

The determination of asymptotic freedom as a fundamental property of strong interaction dynamics was the result of theorists' search for a mathematical framework

that could simultaneously include such behavior and account for the known properties of nuclear matter. Some refer to the work done by Gross, Wilzek, and Politzer as the beginning of Quantum Chromodynamics (QCD) [13], the current accepted theory of strong interactions. Formally, QCD is classified as a non-Abelian gauge field theory. In order to understand what this means in terms of physical quantities, we must inevitably go through a few definitions and key equations.

The first question one might ask is which particles are subject to strong interactions? The strong force only acts on hadrons, which we now define to be any particle composed of quarks. Amongst hadrons, we have baryons, which are systems of quarks (qqq), and mesons, which are quark-anti-quark pairs ($q\bar{q}$). In terms of spin, baryons are classified as fermions (half-interger spin), while mesons are categorized as bosons (integer spin).

1.3.1 Abelian Gauge Field Theories

QCD is a non-Abelian gauge field theory. Since the non-Abelian case is more nuanced, we will first analyze the properties of another fundamental force, one that falls under the Abelian case, so that we can later derive the theory of strong interactions without going over the more general properties of gauge field theories. This approach is based on Ref. [13] and Ref. [14].

In general, gauge field theories satisfy the requirement that the theory itself is invariant under local gauge transformations. The *elements* of the theory are fields and, together with an *operation*, these elements form a *group*. An Abelian group has

the property that elements of the group commute under the group operation. Take for instance real numbers under multiplication. Here, real numbers are the group elements and multiplication is the group operation. The group, $G(\mathbb{R}, \times)$, is Abelian because $a \times b = b \times a$, where $a, b \in \mathbb{R}$.

An example of an Abelian gauge field theory is electrodynamics – the theory that describes interactions between charged particles and electric/magnetic fields. In the case of electrodynamics, group elements are fermion fields of mass m and charge Qe, where $Q = -1$ for electrons, 1 for protons, and likewise for other charged particles. Classically, the well-known Maxwell's equations for electromagnetic fields $\mathbf{E}$ and $\mathbf{B}$ are

$$\nabla \times \mathbf{E} + \frac{1}{c}\frac{\partial \mathbf{B}}{\partial t} = 0, \quad \nabla \cdot \mathbf{B} = 0, \tag{1.2}$$

$$\nabla \times \mathbf{B} + \frac{1}{c}\frac{\partial \mathbf{E}}{\partial t} = \frac{1}{c}Qe\mathbf{J}, \quad \nabla \cdot \mathbf{E} = Qe\rho, \tag{1.3}$$

where $Qe\mathbf{J}$ is the free current and $Qe\rho$ is the total charge for a charge distribution ρ.

Next, we want to convert Maxwell's equations to relativistic notation. We will use the metric $g_{\mu\nu}$ in the Minkowski space $\{x_\mu : \mu = 0, 1, 2, 3\}$, where

$$g_{00} = +1, g_{11} = g_{22} = g_{33} = -1, \text{ otherwise} = 0$$

The contravariant space-time coordinate and energy momentum 4-vectors are given by

$$x^\mu = (ct, \mathbf{r}) \quad p^\mu = (E/c, \mathbf{p}),$$

where t is time, $\mathbf{r}$ is the space coordinate, E is the energy and $\mathbf{p}$ is the momentum

vector. It follows that the covariant vectors are

$$x^\mu = g_{\mu\nu}x^\nu = (ct, -\mathbf{r})$$

$$p^\mu = g_{\mu\nu}p^\nu = (E/c, -\mathbf{p})$$

From these basic definitions we can see that the dot product $p \cdot x$ is

$$p \cdot x \equiv p^\mu x_\mu = g_{\mu\nu}p^\mu x^\nu = Et - \mathbf{p} \cdot \mathbf{r}.$$

From this point forward the convention is that repeated indices are summed. Another important definition is the space and time differential operator

$$\partial^\mu \equiv \frac{\partial}{\partial x_\mu} = \frac{\partial}{\partial t} - \nabla$$

$$\partial^2 = \partial^\mu \partial_\mu = g_{\mu\nu}\partial^\mu \partial^\nu = \frac{\partial^2}{\partial t^2} - \nabla^2.$$

Lastly, we define Dirac gamma matrices to be 4×4 matrices of the form

$$\gamma = \begin{bmatrix} \mathbf{A} & \mathbf{0} \\ \mathbf{0} & \mathbf{B} \end{bmatrix}.$$

There are four gamma matrices in total

$$\gamma^0 = \begin{bmatrix} \mathbf{I}_2 & \mathbf{0} \\ \mathbf{0} & -\mathbf{I}_2 \end{bmatrix}, \quad \gamma^i = \begin{bmatrix} \sigma_i & \mathbf{0} \\ \mathbf{0} & -\sigma_i \end{bmatrix},$$

$$\gamma^5 = \begin{bmatrix} \mathbf{0} & \mathbf{I}_2 \\ -\mathbf{I}_2 & \mathbf{0} \end{bmatrix},$$

where σ_i are the three Pauli matrices. Furthermore, γ^5 satisfies $\gamma^5 = i\gamma^0\gamma^1\gamma^2\gamma^3$ and anticommutes with all γ^μ, such that

$$\{\gamma^5, \gamma^\mu\} = 0.$$

In general, gamma matrices satisfy the anticommutation rule

$$\{\gamma^\mu, \gamma^\nu\} = 2g^{\mu\nu}$$

and the Hermitian conjugate obeys the relation

$$\gamma^{\mu\dagger} = \gamma^0\gamma^\mu\gamma^0.$$

With these definitions in mind, we can combine Eqs. 1.2 and 1.3 in relativistic form as

$$\partial^\mu \mathbf{F}_{\mu\nu} = \frac{1}{c} Qe J_\nu, \quad \mathbf{F}_{\mu\nu} = \partial_\mu A_\nu - \partial_\nu A_\mu, \tag{1.4}$$

where $J^\mu = (c\rho, \mathbf{J})$ is the electromagnetic current four-vector and $A^\mu = (\phi, \mathbf{A})$ is the electromagnetic four-potential.

Now let us introduce charged fermions, which can be expressed as Dirac fields using the relativistic version of Schroedinger's equation for free fields (the Dirac equation):

$$(i\gamma^\mu\partial_\mu - mc/\hbar)\psi = 0$$

Next, we need to obtain Dirac's equation in the presence of an arbitrary electromagnetic field. Whatever solution we get must reproduce Lorentz's equation for the

force on a charged particle due to an electromagnetic field, $\mathbf{F} = Qe(\mathbf{E} + \mathbf{p} \times \frac{1}{mc}\mathbf{B})$. Using this criterion the Hamiltonian of the system is found to be [15]

$$H = c\sqrt{(\mathbf{p} - Qe\mathbf{A}/c)^2 + m^2c^2} + Qe\phi, \tag{1.5}$$

where ϕ is the scalar electromagnetic potential. Notice that the Hamiltonian for the free case is $H_0 = c\sqrt{\mathbf{p}^2 + m^2c^2}$. Hence, in the quantum mechanical version we replace ∇ by $\nabla - iQe\mathbf{A}/\hbar c$ and ∂_0 by $\partial_0 + iQe\phi/\hbar c$. That means that the Dirac equation in the presence of an electromagnetic field is simply

$$\left[i\gamma^\mu\left(\partial_\mu + iQ\frac{e}{\hbar c}\mathbf{A}_\mu\right) - \frac{mc}{\hbar}\right]\psi = 0 \tag{1.6}$$

It follows from Eq. 1.6 that the quantity $\bar{\psi}\gamma_\mu\psi$ is a conserved current,

$$\partial^\mu(\psi^\dagger\gamma_0\gamma_\mu\psi) \equiv \partial^\mu(\bar{\psi}\gamma_\mu\psi) = 0, \tag{1.7}$$

and therefore it corresponds to the electromagnetic current in Eq. 1.4,

$$J_\mu = \bar{\psi}\gamma_\mu\psi. \tag{1.8}$$

.

We now have all the elements we need to describe the motion of charged particles in an electromagnetic field (Eqs. 1.4, 1.6, and 1.8). We also know from the action principle that these equations must be a direct result of the Euler-Lagrange equations from a suitable Lagrangian. This Lagrangian density [1] is given by [13]

$$\mathscr{L} = -\frac{1}{4}F^{\mu\nu}F_{\mu\nu} + \bar{\psi}[i\gamma^\mu(\partial_\mu + iQe\mathbf{A}_\mu) - m]\psi. \tag{1.9}$$

[1] In field theories the Lagrangian is replaced by the Lagrangian density, which is a function of the fields and their derivatives and their space-time coordinates.

An important feature of this particular Lagrangian density is that it is invariant under a phase shift by a constant θ of the field ψ, i.e.

$$\psi' \rightarrow e^{-iQ\theta}\psi \tag{1.10}$$

The transformation in Eq. 1.12 is called the Abelian (because the charge Q commutes with the field) global (since θ does not depend on x) transformation. This particular transformation is an element of a set of transformations that constitutes the unitary group in one dimension, U(1). A major theorem in field theory, the Noether theorem, establishes that the invariance under such transformations implies that there exists a conserved current in the theory, which we derived to be Eq. 1.8.

What if we want to define a transformation for which the parameter θ does depend on x? In this case, the Lagrangian is only invariant if we also introduce a similar transformation for $\mathbf{A}_\mu$,

$$\mathbf{A}^\mu \rightarrow \mathbf{A}^\mu + \frac{1}{e}\partial^\mu\theta \tag{1.11}$$

These transformations are called Abelian *local* gauge transformations, since the parameter θ depends on the *local coordinate*, x. Like quantum electrodynamics, QCD is invariant under local gauge transformations, which is why it is classified as a gauge field theory. Next, we will explore how QCD differs from quantum electrodynamics, and understand why it constitutes a non-Abelian gauge field theory.

1.3.2 Non-Abelian Gauge Field Theories

Consider a fermion field $\psi(x)$ with mass m belonging to an N-dimensional, arbitrary group G (we will specify the group later). The field components – and group elements – are $\psi_n(x), n = 1, 2, 3, ..., N$. Furthermore, the group generators, $T^a, a = 1, 2, ..., n$, are subject to the commutation relation

$$[T^a, T^b] = if^{abc}T^c, \tag{1.12}$$

where f^{abc} are the structure constants and are antisymmetric in all indices. The constants a, b, and c characterize the algebra of the group. Hence, if we consider a group element U of G, $U = exp(-iT^a\theta^a)$, where θ^a accounts for any parameters that depend on x, the transformation property of $\psi(x)$ is

$$\psi'_n = U_{nm}\psi_m. \tag{1.13}$$

Here, the only difference so far is the x-coordinate dependence and the fact that Q was replaced by T^a. Hence, we can try the following Lagrangian for the free fermion field

$$\mathscr{L} = \bar{\psi}_n(i\gamma^\mu\partial_\mu - m)\psi_n. \tag{1.14}$$

We have shown that this Lagrangian is invariant under the transformation in Eq. 1.13 if θ^a has no x-coordinate dependence. In the electrodynamics case, we can make the Langrangian invariant under local transformations by replacing the derivative with its covariant form. For the case of a fermion field interacting with a gauge

field A_μ^a [2], we can try a similar approach, using the following form for the covariant derivative,

$$D_\mu = \partial_\mu - igT^a A_\mu^a, \tag{1.15}$$

where g is the coupling strength between the fermion and gauge fields. D_μ is a tensor with components

$$(D_\mu)_{mn} = \delta_{mn}\partial_\mu - igT^a_{mn}A^a_\mu. \tag{1.16}$$

Now we need to show that the corrected Lagrangian

$$\mathscr{L} = \bar{\psi}_n(i\gamma^\mu(D_\mu)_{mn} - m\delta_{mn})\psi_n \tag{1.17}$$

$$= \bar{\psi}(i\gamma^\mu D_\mu - m)\psi \tag{1.18}$$

is invariant under the non-Abelian local gauge transformation in Eq. 1.13. We impose that the gauge fields obey the transformation rule

$$T^a A'^a_\mu = U(T^a A^a_\mu - \frac{i}{g}U^{-1}\partial_\mu U)U^{-1} \tag{1.19}$$

and note that because D_μ is the covariant derivative it is also true that

$$(D_\mu\psi)' = U(D_\mu\psi). \tag{1.20}$$

Therefore,

$$(D_\mu\psi)' = (\partial_\mu - igT^a A'^a_\mu)\psi' \tag{1.21}$$

$$= U(\partial_\mu + U^{-1}\partial_m u U - igU^{-1}T^a U A'^a_\mu)\psi \tag{1.22}$$

$$= U(D_\mu\psi), \tag{1.23}$$

[2]The gauge field A_μ^a is the non-abelian equivalent of the photon field A_μ in electrodynamics.

and Eq. 1.19 is satisfied. From this, we can conclude that $\bar{\psi}D_\mu\psi$ is invariant under the non-Abelian local gauge transformation in Eq. 1.13 and hence the Lagrangian must also be invariant under the transformation.

However, the Lagrangian in Eq. 1.18 only accounts for the interaction between the fermion and gauge fields, and is missing a kinetic term purely from the gauge fields themselves. Unfortunately, the example in electrodynamics does not help in this case. In Ref. [13] the author uses the infinitesimal form of the transformation in Eq. 1.13 to derive the kinetic term and show that it is invariant. The result is the general form of the Lagrangian of QCD, which is invariant under the non-Abelian local gauge transformations in Eq. 1.13 and Eq. 1.19.,

$$\mathscr{L} = -\frac{1}{4}F^a_{\mu\nu}F^{a\mu\nu} + \bar{\psi}(i\gamma^\mu D_\mu - m)\psi, \tag{1.24}$$

where $-\frac{1}{4}F^a_{\mu\nu}F^{a\mu\nu}$ is the gauge field kinetic term.

1.4 Features of the QCD Lagrangian

Perhaps the most remarkable element of the Lagrangian of QCD is that it includes interactions among the gauge field themselves. This is seen explicitly in the term

$$gf^{abc}A^b_\mu A^c_\nu \tag{1.25}$$

from the Lagrangian element $F^a_{\mu\nu}$. At the time the theory of quantum chromodynamics was derived, this was an entirely new feature in field theory. Furthermore, the gauge group in question turned out to be the color SU(3) group, a subgroup of the U(3) group, which is comprised of all 3×3 unitary matrices. The fermion

fields ψ correspond to quarks (the fundamental elements of the color SU(3) group), while the gauge fields A^a_μ represent gluons, the force carriers in strong interactions (elements of the color SU(3) group in the adjoint representation).

Over the next sections, we will introduce the physical quantities and properties that are key to our understanding of matter under extreme conditions and how they emerge from the theory of QCD, especially its Lagrangian. The first step is understanding the degrees of freedom required by the accepted formulation of QCD.

1.4.1 The Color SU(3) Group and Discrete Symmetries

The color degree of freedom (or color charge) was introduced in QCD to give the color SU(3) group a physical interpretation. The need to have different color constituents in the theory arose from an inconsistency between what was known from baryon spin and baryon wave functions.

As presented in Table 1.1, there are six known flavors of quarks [16], which differ on their mass, isospin, and flavor content. Because baryons are three-quark states, quarks inevitably have a spin of $\frac{1}{2}$. For $\frac{1}{2}$-spin baryons, the resulting baryon wave function is in agreement with Fermi-Dirac statistics, which requires the wave function to be antisymmetric. However, without the color degree of freedom, $\frac{3}{2}$-spin baryons exist in a state that is symmetric in space, spin, and quark flavor. This dilemma was resolved by introducing the color charge, which takes three possible values, $a = 1, 2, 3$, conventionally called red, green, and blue. Each quark carries exactly one value of color charge. With the inclusion of this new index, the baryon wave functions are

totally antisymmetric.

Table 1.1: All six known quark flavors with respective electric charge, spin, baryon number, and mass.

Quark	Charge (e)	Isopin	Baryon Number	Mass (MeV)
up (u)	2/3	1/2	1/3	2.16
down (d)	-1/3	-1/2	1/3	4.67
charm (c)	2/3	0	1/3	1270
strange (s)	-1/3	0	1/3	93
top (t)	2/3	0	1/3	$172.9 \cdot 10^3$
bottom (b)	-1/3	0	1/3	4180

The addition of this new degree of freedom was supplemented with the requirement that only color singlet states exist in nature. That is, all composite particles are color neutral. This requirement results in singlet states that are precisely mesons $q\bar{q}$ and baryons $\varepsilon^{abc} q_a q_b q_c$. The color SU(3) hypothesis quickly succeeded in explaining and predicting experimental results of historical significance for QCD, such as the prediction of the $\pi_0 \to \gamma\gamma$ decay rate [17, 18] and new baryonic states, such as the Ω^-, which was discovered at Brookhaven in 1964 [19].

Some interesting symmetries arise from the algebraic structure of QCD. Perhaps most famously, the baryon octets and decuplet, illustrated in Figure 1.1. These symmetries not only allowed theorists to make predictions regarding missing states (e.g., the Ω^-, which was missing from the J = 3/2 decuplet) – there are fundamental physical properties of strong interactions that can be derived from these exact symmetries. Local gauge invariance accounts for the renormalizability of QCD, but it is only one of the transformations under which the QCD Lagrangian is invariant. Parity, charge conjugation, and time reversal are also symmetries associated with QCD which are in agreement with observations of strong interaction processes [20].

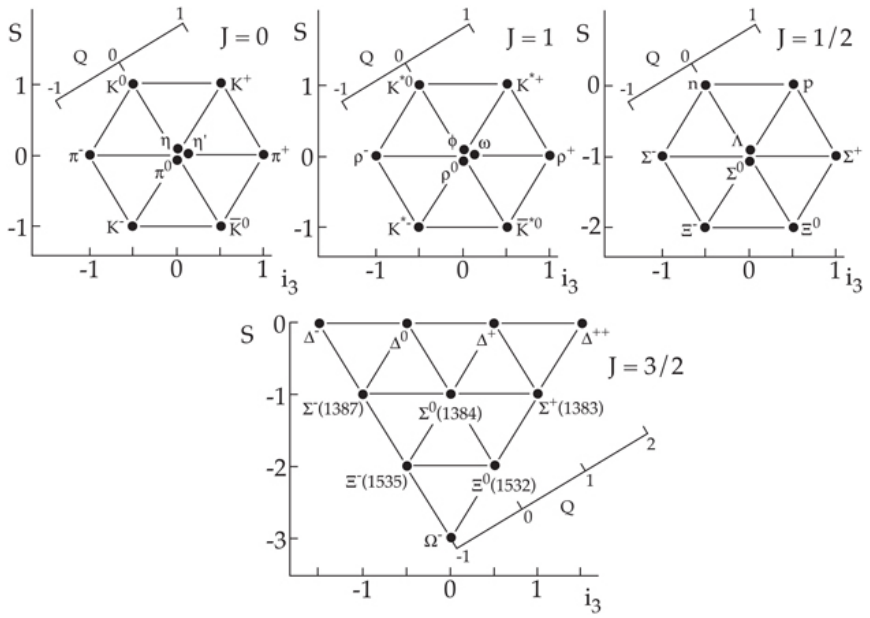

Figure 1.1: Baryon octets and decuplet displayed with respect to isospin (I_3), strangeness (S), and charge (Q), grouped by total angular momentum (J) [21].

1.4.2 Confinement and Asymptotic Freedom

The property of quark confinement follows directly from the exact symmetry associated with the color charge. That is, all hadron states are color singlets i.e., quarks are confined to color neutral mesons and baryons that cannot be separated into individual quarks or combined to form colored states. While confinement can be somewhat easily understood in terms of the color degrees of freedom, the need for asymptotic freedom is more nuanced and can be approached from different perspectives.

The governing principle behind early collider experiments was that, in order to gain insight on the elementary structure of a particle, a structureless object needs to be used as a probe. For instance, in order to probe the inside of a proton one could use a beam of electrons. Let's consider an elastic collision between a proton

Figure 1.2: Diagram of elastic scattering between a proton and an electron.

and an electron, $ep \rightarrow ep$, as shown in Figure 1.2. If we consider the proton to be a point-like particle, the differential cross-section in the laboratory frame, ignoring recoil effects, is given by

$$\left(\frac{d\sigma}{d\Omega}\right)_M = \frac{\alpha^2 cos^2(\theta/2)}{4E^2 sin^4(\theta/2)}, \tag{1.26}$$

where $\alpha = e^2/4\pi$, E is the energy of the electron, and θ is the scattering angle in the laboratory frame. Eq. 1.26, known as the Mott cross-section, shows significant scattering across a wide region in θ, which is expected due to our assumption of a point-like nature for the target.

This behavior is not what was observed experimentally and considering what we know about the structure of protons, the actual cross-section is given by [22, 23]

$$\frac{d\sigma}{d\Omega} = \left(\frac{d\sigma}{d\Omega}\right)_M \left[G_M(Q^2)\frac{Q^2}{2M^2}tan^2(\theta/2) + \frac{G_E^2(Q^2) + G_M^2(Q^2)Q^2/4M^2}{1 + Q^2/4M^2}\right]\frac{E'}{E}, \tag{1.27}$$

where M is the proton mass,

$$Q^2 = 4EE'sin^2(\theta/2) \tag{1.28}$$

is the momentum transfer, E' is the energy of the scattered electron, G_M and G_E are the magnetic and electric form factors defined by

$$G_M(Q^2) = F_1(Q^2) + 2MF_2(Q^2) \tag{1.29}$$

$$G_E(Q^2) = F_1(Q^2) + F_2(Q^2)Q^2/2M \tag{1.30}$$

$$\langle N|j_\mu(0)|N\rangle = \bar{u}[F_1(Q^2)\gamma_\mu + F_2(Q^2)i\sigma_{\mu\nu}q^\nu]u, \tag{1.31}$$

with $j_\mu(x)$, representing the electromagnetic current, $|N\rangle$ the proton state, $\sigma_{\mu\nu} = i[\gamma_\mu, \gamma_\nu]/2$, u is the Dirac spinor for the nucleon, and q^ν is the momentum transferred from the electron to the proton. Despite the convoluted form, these equations express that $G_M(Q^2)$ and $G_E(Q^2)$ are decreasing functions of Q^2 if the proton extends in space. The implication for Eq. 1.27 is that the rate of scattering at large angles is suppressed. Thus, at lower energies, we expect results for the differential cross-section and the form factors $G_M(Q^2)$ and $G_E(Q^2)$ to reflect electrons scattering elastically from an object of finite size. Indeed, what was observed in experiments is that the form factors can be approximated by the dipole form

$$G_M(Q^2)/\mu = G_E(Q^2) = \frac{1}{(1 + \frac{Q^2}{0.7})^2}, \tag{1.32}$$

where $\mu = 2.79$ is the magnetic dipole moment for the proton.[3] From these values it was possible to calculate the mean square charge radius for the proton,

$$\langle r^2 \rangle = \int d^3x r^2 j_0(x) = -6\frac{\partial G_E(0)}{\partial Q^2} = 0.67 \times 10^{-26} cm^2. \tag{1.33}$$

The takeaway from proton-electron elastic scattering is that the proton is not a point-like particle, but an object that extends in space to a finite size which can be calculated using the magnetic and electric form factors.

[3] μ is in terms of the proton Bohr magnetons and Q^2 is in GeV^2.

However, for higher Q^2, we expect these functional forms to reflect the inner structure of the proton, as the electron beam should have enough energy to probe the quarks inside the target in a process known as deep inelastic scattering.

As discussed in section 1.2, it was expected from field theory models that charges could change their effective size depending on whether they are probed at large or small distances (or, equivalently, large energies). These changes were described by Symanzik's β-function [24],

$$Q^2 \frac{\partial \alpha_s(Q^2)}{\partial Q^2} = \beta(\alpha_s(Q^2)), \tag{1.34}$$

in which the effective size of the coupling strength between quark and gluon fields, α_s, is a function of the energy of the collision.

In 1973, Gross, Politzer and Wilczek succeeded in showing that chromodynamics, with colored quark and gluon fields that obey SU(3) color symmetry, resulted in a negative β-function [25]. This β-function not only indicated that quarks and gluons were asymptotically free at small distances, but it also led to the conclusion that they become confined at large distances. In the years that followed, several electron-nucleon scattering experiments confirmed this prediction, as shown in Figure 1.3.

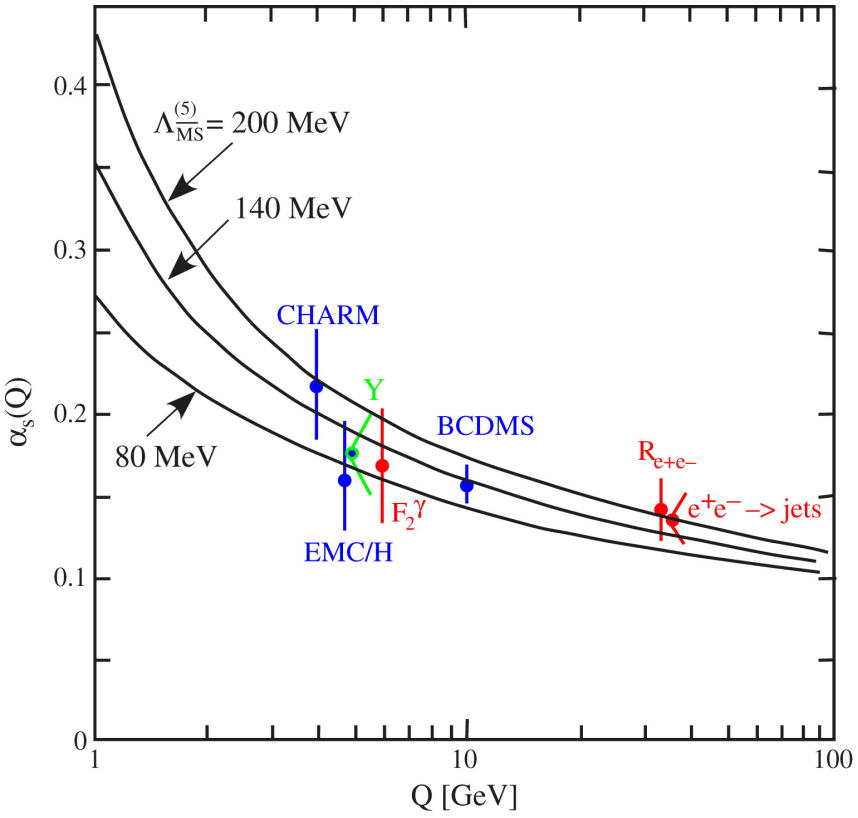

Figure 1.3: Summary of experimental results in 1989 from deep inelastic lepton-nucleon scattering combined with electron-positron annihilation data in contrast with theoretical predictions for coupling strength [26].

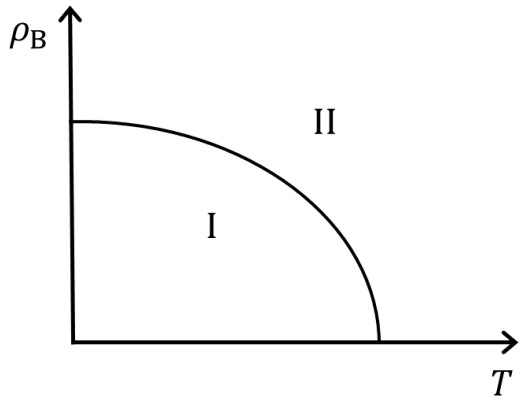

Figure 1.4: Adaptation of the QCD phase diagram proposed by Cabibbo and Parisi in terms of temperature (T) and baryonic density (ρ_B).

1.4.3 The QCD Phase Diagram

The scattering behavior observed from nuclear matter at different energies was the first hint that QCD presented a rich phase structure. The earliest attempt to express the seemingly conflicting principles of confinement and asymptotic freedom in terms of a phase diagram was proposed by Cabibbo and Parisi in 1975 [12], as shown in Figure 1.4. The interpretation was that there was a transition line that clearly separated confined nuclear matter (I) from a quark-gluon plasma phase (II) corresponding to asymptotically free quarks and gluons.

One of the main theoretical challenges surrounding the study of QCD at large baryon densities is that the first-principle theory discussed in this chapter cannot be solved using standard lattice techniques at finite baryonic densities. To a large extent, the early phase structure proposed by Cabbibo and Parisi still holds. The "modern" representation of the QCD phase diagram is shown in Figure 1.5. Despite decades of theoretical development and experimental programs, the phase structure

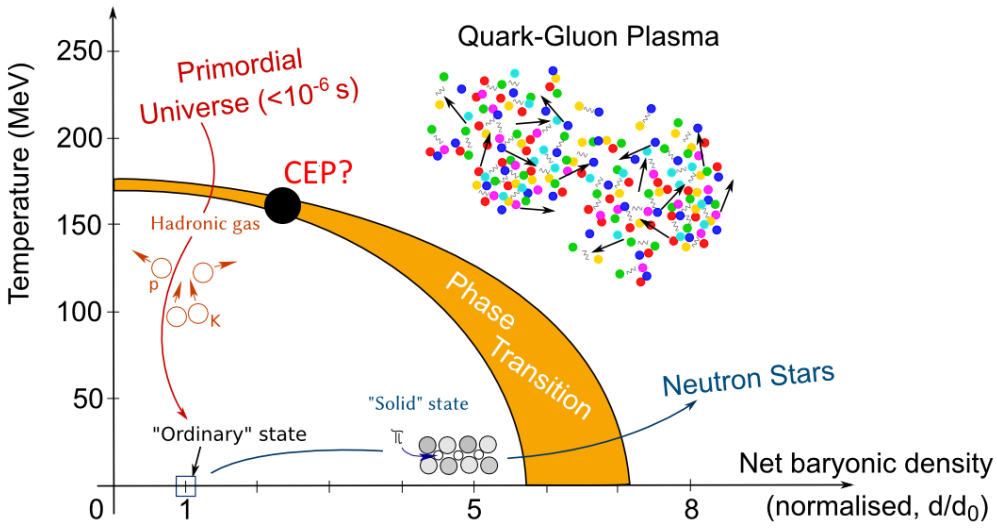

Figure 1.5: Conventionally accepted representation the QCD phase diagram in terms of temperature and baryonic density [27]. CEP stands for critical end point, i.e. critical point.

of QCD remains mostly an open question.

Chapter 2

Experimental Overview of Heavy-Ion Collisions

2.1 Circumstantial Evidence: A First Glimpse of the QGP

The realization that asymptotic freedom is a feature of QCD and, subsequently, that QCD exhibits a high-temperature phase of weakly interacting quarks and gluons, marked the beginning of a new era in both theoretical and experimental high-energy physics. By the end of the 1970's, theorists agreed on the prediction that this state of "collectivized" quarks and gluons would form at extremely high temperatures, around an energy density of 1 GeV/fm^3 [28]. The only way to test these predictions was to somehow create such highly energetic conditions experimentally.

It would take almost four decades to confirm the existence of the QGP. In the late 1980's, the two world-leading facilities in particle physics, CERN (Counseil Europeen pour la Recherche Nucleaire), in Geneva, Switzerland, and Brookhaven National Laboratory, in New York, announced they would attempt to create the QGP [29, 30, 31]. In 2000, CERN concluded its first heavy-ion program run at the Super Proton Synchrotron (SPS), which began in 1994, and published circumstantial evidence for the creation of a new state of matter in lead (Pb + Pb) collisions [32].

2.1.1 QGP Signatures

The difficulty in confirming the creation of the QGP stems from the nature of the strong force. When and if created, the QGP itself would have a very transient existence, as the system would only exist in the required state of energy density for a short amount of time before cooling down into a hadronic state. In addition, because of color confinement, single quarks and gluons can never escape the collision and reach the detectors – they will always recombine into color neutral hadrons. Consequently, hadrons account for the vast majority of particles that reach the detectors, regardless of whether or not QGP is formed during the collision. Therefore, evidence for or against the creation of the QGP had to be extracted from a careful analysis of the observed final state of hadrons.

The first indirect evidence for the creation of the QGP in Pb–Pb collisions at CERN was the explosive nature of systems observed by the detectors. In general, after the lead atoms collide with each other, the resulting energy gives rise to many

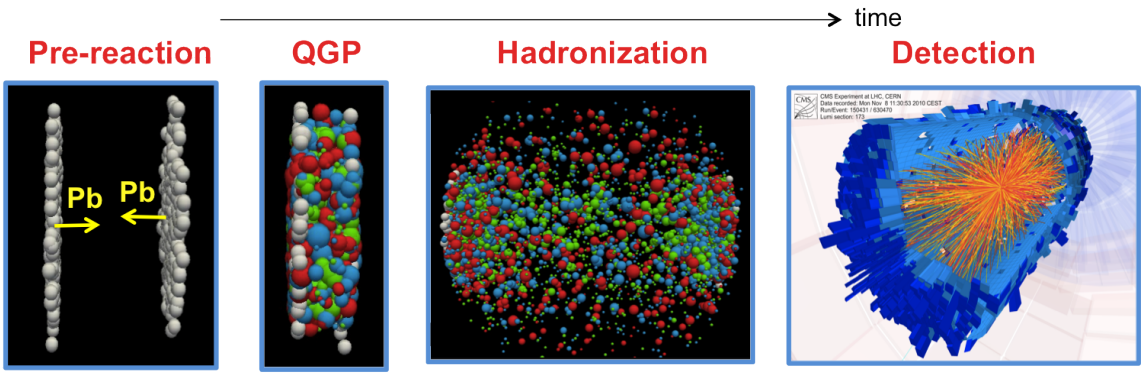

Figure 2.1: Evolution of a Pb+Pb collision illustrating the different stages of the system [33].

secondary interactions before any particles can escape from the collision. This is known as the fireball. When the fireball has expanded by a factor of 30-50, the interactions finally cease, and the composition of the hadrons that will reach the detector is fixed. This state of the collision is known as the chemical freeze-out. Because these particles were first created in a highly energetic state, their composition carries a "memory" of the early collision stage. This information can be extracted through the analysis of relative particle abundances and momentum distributions. SPS looked at more than 20 different hadron species and carefully analyzed two-particle correlations and momentum distributions. They found that the fireball expanded with a rate of over half the speed of light. Such an explosive expansion could only be the result of immense pressure in the early collision stages. In addition, measurements of the angular momentum distribution matched theoretical calculations corresponding to an energy density of ~ 1 GeV/fm^3, which is exactly the QCD prediction for the transition temperature [34, 35, 36]. Other interesting features were recorded by experiments during the lead beam program at CERN, such as the enhancement

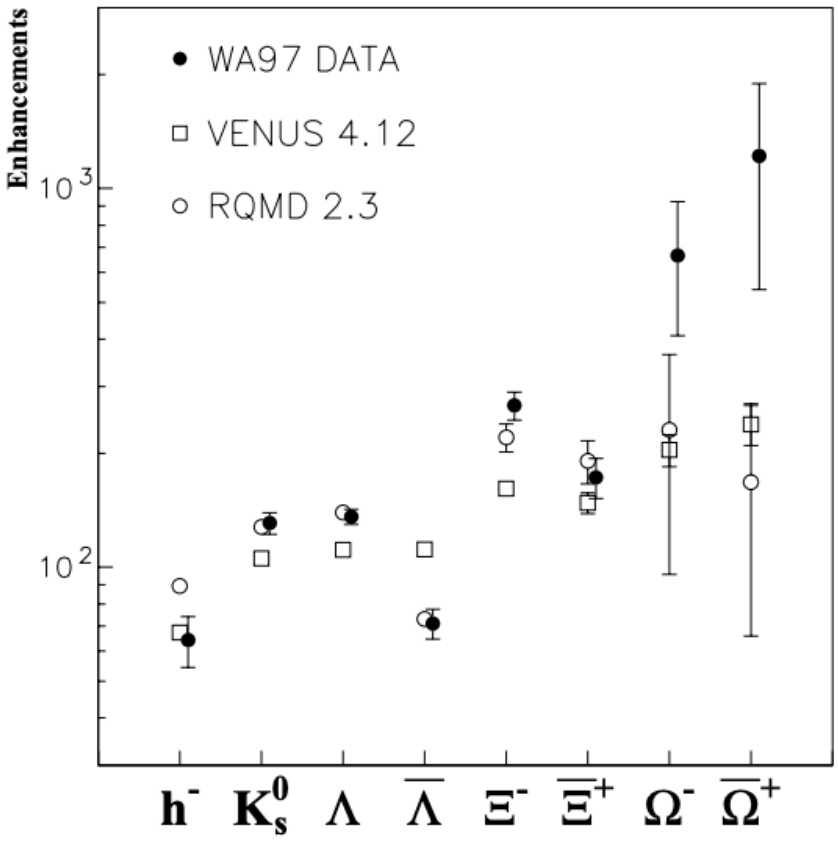

Figure 2.2: Strangeness enhancement: experimental data from SPS run WA97 (black dots) compared to theoretical predictions, VENUS (open squares) and RQMD (open circles) models [42].

of particles containing strange quarks [37, 38, 39], shown in Figure 2.2, and the suppression of particular charmonium (particles containing charm and anti-charm quarks) states [40, 41], both of which matched theoretical predictions for possible QGP signatures.

For most theorists and experimentalists, the picture was clear – two colliding nuclei create a huge amount of energy, which materializes in the form of strongly interacting quarks and gluons. This dense state, which has an initial energy density

of about 3-4 GeV/fm^3, suppresses the formation of charmonium states, enhances strange particle abundance and begins to drive the explosive expansion of the fireball. As the plasma cools down it expands and becomes more dilute. Once the system reaches an energy density of 1 GeV/fm^3 (T≈155 MeV) quarks and gluons go through the hadronization process and the final hadron abundance is fixed. Later, at an energy density of about 50 MeV/fm^3 (T=100-120 MeV) the fireball undergoes a chemical freeze-out (hadrons stop interacting), at which point it expands with more than half the speed of light.

2.2 Au+Au Collisions at the Relativistic Heavy-Ion Collider

Though SPS found convincing circumstantial evidence for QGP formation, it is commonly accepted that the discovery of the QGP took place at the Relativistic Heavy Ion Collider (RHIC) in 2005 following five consecutive years of measurements of Au+Au collisions [43]. Key measurements were taken across four major experiments – BRAHMS, PHOBOS, STAR, and PHENIX. Since the four experiments were designed with different detectors, each one of them was able to offer a unique perspective and evidence for QGP formation in Au+Au collisions at RHIC.

BRAHMS, which stands for Broad RAnge Hadron Magnetic Spectrometers, offered great momentum resolution and hadron identification capabilities. Because of these features, the BRAHMS collaboration was able to deduce from the post-collision

charged particle count that the energies required to produce such high multiplicities much exceeded that of hadronic matter. They found that "initial energies surpassed the energy density of a nucleus by a factor of 30, the energy density of a baryon by a factor of 10, and the energy density for QGP formation that is predicted by lattice QCD calculations by a factor of 5 [44]."

PHOBOS, a collection of silicon detectors, was designed to count the total number of produced particles with precision and study the angular momentum distributions of these products. The goal was not only to understand these two features of heavy-ion collisions, but also to look for fluctuations in particle production and angular distribution. The PHOBOS collaboration found evidence for the formation of "a high energy density system" that could not be accounted for in hadronic degrees of freedom [45], in agreement with the findings published by the BRAHMS collaboration.

Similarly, the STAR collaboration concluded from their experiments that "theory-experiment comparison suggested that central Au+Au collisions at RHIC produce dense, rapidly thermalizing matter characterized by initial energy densities above the critical values predicted by lattice QCD for establishment of a quark-gluon plasma (QGP)" which presented "nearly ideal fluid flow, marked by constituent interactions of very short mean free path, established most probably at a stage preceding hadron formation" [46]. In other words, not only was there evidence that QGP was being produced in these collisions, but experimental data also implied that regardless of what pre-hadronic state was being produced, its constituents behaved like a nearly perfect liquid, and were able to seemingly move past each other. A similar conclusion

was reached by the BRAHMS collaboration.

Lastly, the PHENIX collaboration, which analyzed measurements of charged particle multiplicities, transverse energy, yield ratios and spectra of identified hadrons in a wide range of transverse momenta (p_T), elliptic flow, two-particle correlations, non-statistical fluctuations, and suppression of particle production at high p_T, concluded that the high density state being produced in the same kinds of collision (central, high beam energy) could not be explained in terms of the dynamics of color-neutral hadrons [47].

Surprisingly, experimentalist across all four collaborations were not only seeing evidence of parton-like behavarior, but there was also strong indication that this new state of matter being created had the properties of "perfect fluid." Figure 2.3 from the STAR report [46] illustrates the dependence on the elliptic flow, v_2, of charged π's, K, p, and Λ as a function of transverse momentum, p_T. These measurements were in eerie agreement with hydrodynamics results for a thermalized, ideal fluid expansion. Furthermore, the predictions that seemed to best fit experimental data were based on an equation of state that was consistent with lattice QCD calculations including a phase transition at 165 MeV.

With all four distinct experiments reaching identical conclusions, the case for deconfinement was stronger than it had ever been. The reports released by the BRAHMS, PHOBOS, STAR, and PHENIX collaborations also outlined the improvements necessary from both theory and experiment that would eventually lead to sufficient evidence that quark-gluon plasma, and not another high-density nuclear state, was being created at RHIC. Though the PHOBOS and BRAHMS programs

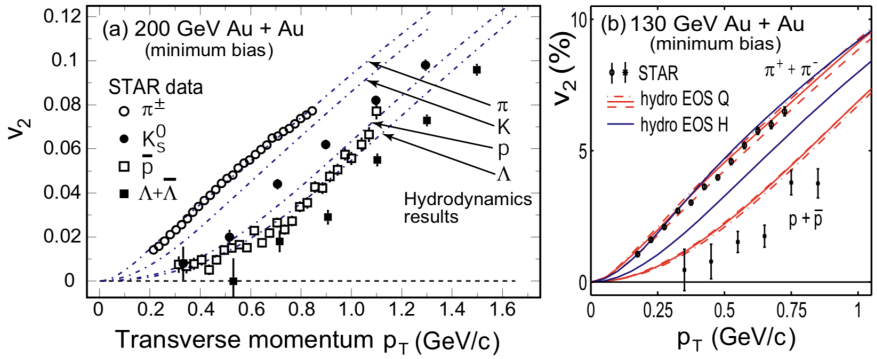

Figure 2.3: (a) STAR results of the transverse momentum dependence of the elliptic flow parameter in 200 GeV Au+Au collisions for $\pi^{\pm}, K^0_s, p$, and Λ [48]. Hydrodynamics calculations [49, 50] assuming early thermalization, ideal fluid expansion, an equation of state consistent with LQCD calculations including a phase transition at $T_C = 165$ MeV (EOS Q), and a sharp kinetic freezeout at a temperature of 130 MeV, are shown as dot-dashed lines. Only the lower p_T portion ($p_T \leq 1.5$ GeV/c) of the distributions is shown. (b) Hydrodynamics calculations of the same sort as in (a), now for a hadron gas (EOS H) vs. QGP (EOS Q) equation of state [51, 49], compared to STAR v_2 measurements for pions and protons in minimum bias 130 GeV Au+Au collisions [52].

officially ended in 2005 and 2006, respectively, STAR and PHENIX continued to make measurements through the following generation of experiments at RHIC.

2.3 The Beam Energy Scan Program

For the first five years of measurements, RHIC operatared very close to its maximum collision energy, around 200 GeV. After careful analysis, the consensus among the four experiments that participated in the first runs was that a new state of matter with partonic degrees of freedom was created at center of mass energies $\sqrt{s_{NN}} = 62 - 200$ GeV. However, most of the questions that motivated the construction of RHIC in the first place, mostly regarding the structure of the QCD phase diagram, remained unanswered [53, 54]. Luckily, a large range of collision energies available at RHIC had not yet been explored. With that in mind, the STAR collaboration proposed a new program – the Beam Energy Scan (BES) – with the goal of probing higher density regions of the QCD phase diagram.

In 2010, the STAR collaboration released results from the BES trial run, which suggested that the QGP quickly achieves local thermal equilibrium and that the transition from the QGP to hadronic matter is a crossover, i.e. a smooth, continuous transition at high collision energies (low baryon densities) [55, 56]. In contrast, several theoretical models predicted that the transition becomes first-order at lower temperatures and high baryon densities, conditions that correspond to lower collision energies [57, 58, 59, 60, 61, 62, 63, 64, 65]. If these theoretical predictions were correct, a critical point would mark the exact location in the phase diagram where

Table 2.1: BES-I: Number of expected events and run time for different collision energies.

$\sqrt{s_{NN}}$ (GeV)	μ_B (MeV)	Rate (Hz)	Event Count	Run Time (days)
5.0	550	0.8	Beam development	7
7.7	410	3	4M	36
11.5	300	10	4M	15
17.3	229	33	15M	13
27	151	92	33M	10
39	112	190	24M	4

this change occurs, presumably at intermediate temperatures and baryon chemical potentials.

The Beam Energy Scan program sought to answer: 1) Can evidence of a critical point (CP) be detected? 2) Can a first-order phase transition be detected? and 3) How does the medium created in the collisions change as $\sqrt{s_{NN}}$ is lowered? 4) How does the QGP change when multiple conserved charges are considered?

The theoretical models at the time suggested that the proposed critical point location could fall within RHIC beam energies [66, 67, 68, 69], so BES proposed a scan of the region between $\sqrt{s_{NN}} = 5 - 39$ GeV in an initial run, BES-I, which would inform a second run, BES-II, that would provide more data on areas of particular interest. As shown in Figure 2.4 [70], the proposed range for BES-I bridged the gap between SPS and RHIC data in terms of temperature, T, and baryon chemical potential, μ_B, while focusing on lower collision energies, where the probability of identifying a CP was thought to be highest. Table 2.1 outlines the run plan for BES-I.

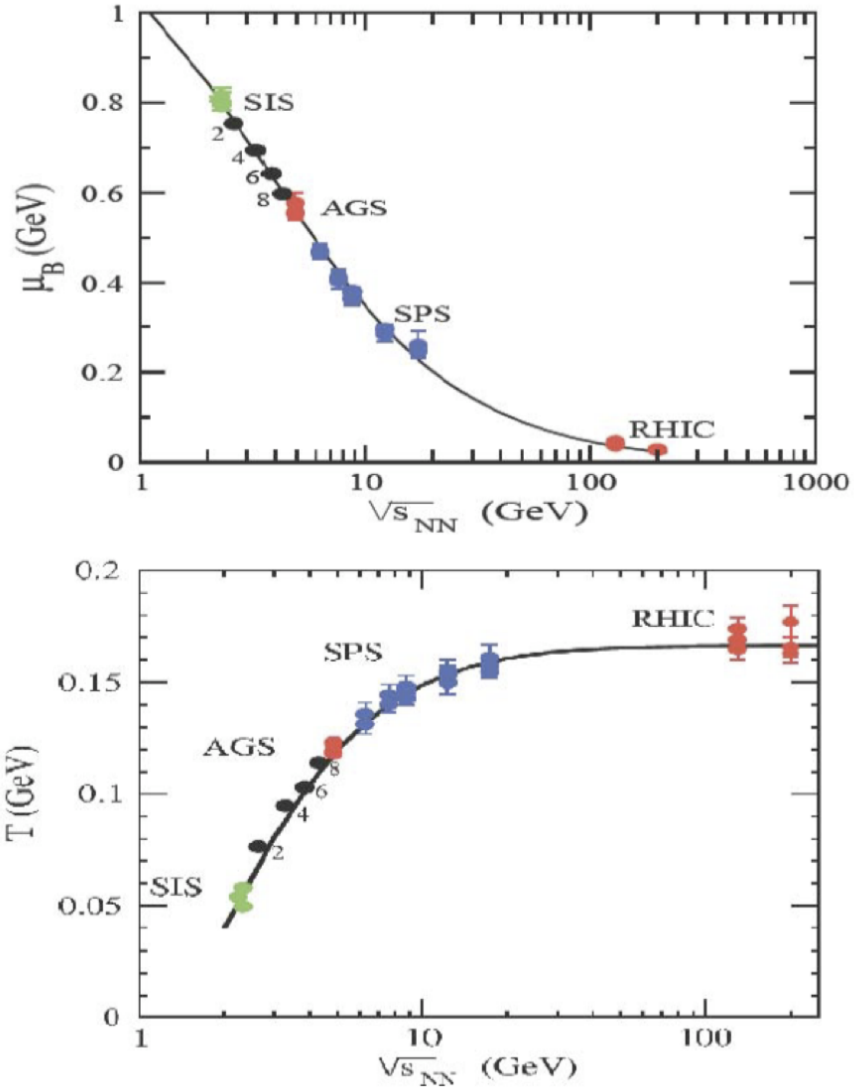

Figure 2.4: The calculated chemical freeze-out temperature and chemical potential as functions of collision energy. The black curves are phenomenological parameterizations of the data points displayed.

2.3.1 Locating the Critical Point: Fluctuations

First-principle lattice QCD calculations showed that the derivatives of the partition functions with respect to baryon, charge, and strangeness chemical potential were expected to show large fluctuations as a function of temperature [71]. In particular, the moments of the charge, baryon, and strangeness chemical potential can be obtained from the derivatives of the pressure with respect to the chemical potential, normalized by the correct power of the temperature:

$$\chi_{i,j,k}^{B,Q,S} = \frac{\partial^{i+j+k}(P/T^4)}{\partial(\mu_B/T)^i \partial(\mu_Q/T)^j \partial(\mu_S/T)^k}$$

These fluctuations can in turn be related to moments of event-by-event net-particle multiplicity distributions in heavy-ion collisions [72]. Figures 2.5 and 2.6 show χ_2^{BQS} and χ_4^{BQS} fluctuations as functions of the temperature for vanishing baryon chemical potential with a phase transition at $T_c = 200$ MeV. The baryon number fluctuations are expected to diverge at the critical point and were therefore the most obvious candidate for CP signatures.

In order to detect critical behavior due to changes in charge, baryon, and strangeness fluctuations, the STAR collaboration proposed measurements of fluctuations in the expected transverse momentum, $\langle p_T \rangle$, the K/π, p/π, and K/p ratios, and elliptic flow, v_2, in addition to high moments of the net-proton yield, which can provide insight on baryon number fluctuations.

The relationship between distribution moments and fluctuations is as follows,

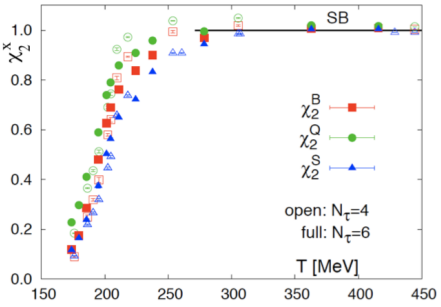

Figure 2.5: Second order fluctuations of baryon number, electric charge and strangeness for $\mu_B = 0$ and $T_c = 200$ MeV [71].

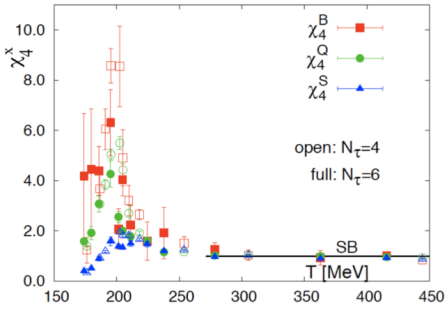

Figure 2.6: Fourth order fluctuations of baryon number, electric charge and strangeness for $\mu_B = 0$ and $T_c = 200$ MeV [71].

$$\text{Mean: } M = \chi_1 \qquad \text{Variance: } \sigma^2 = \chi_2$$

$$\text{Skewness: } S = \frac{\chi_3}{\chi_2^{3/2}} \qquad \text{Kurtosis: } \kappa = \frac{\chi_4}{\chi_2^2}$$

These relations establish the foundation for comparison of experimental data to theoretical predictions. Since the QGP presented fluid-like properties, relativistic hydrodynamic simulations of heavy-ion collisions were the main theoretical tool available to bridge the gap between theory and experiment. Models coupled with a hydrodynamic stage, such as Ultra relativistic Quantum Molecular Dynamics (UrQMD), which allowed theorists to carry out full simulations of nucleus-nucleus collisions and make predictions for various experimental observables. Figure 2.7 displays the comparison of predictions from two theoretical models to data from STAR and SPS for the standard deviation of the K/π ratio as a function of collision energy.

This kind of phenomenological analysis was what the STAR team hoped would confirm the existence and location of the QCD critical point, and they expected that

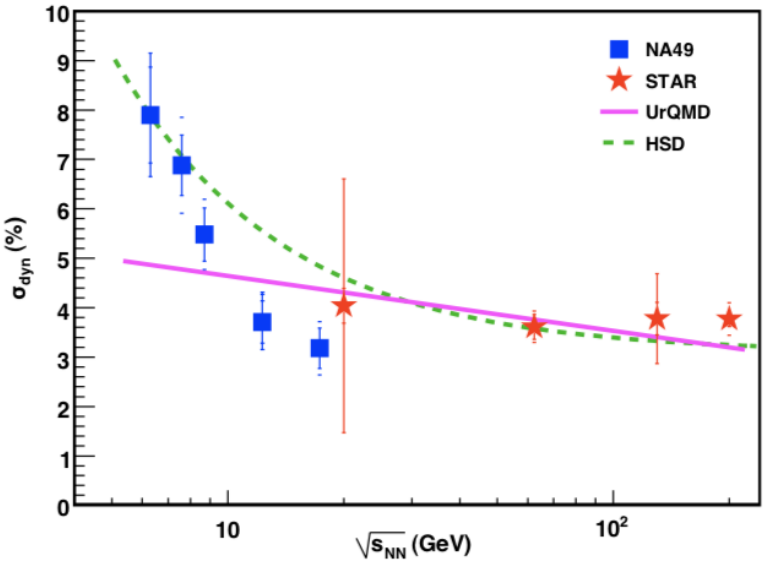

Figure 2.7: Comparison of the predictions of the Hadron String Dynamics (HSD) and UrQMD models to the experimental data from STAR and SPS-NA49 for the standard deviation, σ, of the K/π ratio as a function of collision energy. Data from [73, 74]

the Beam Energy Scan program would result in such discovery.

2.3.2 Results from BES-I

Phase I of the BES program collected data between the years 2010 and 2014. Collisions were recorded at $\sqrt{s_{NN}} = 7.7, 11.5, 14.5, 19.6, 27, 39, 62.4$, and 200 MeV, which significantly increased the range of baryonic chemical potentials covered at RHIC to $\mu_B = 20 - 420$ MeV at the point of chemical freeze-out [75]. Figure 2.8 shows the conjectured phase diagram for QCD, including the range of baryonic chemical potential covered by different major experiments, and highlights the higher μ_B values surveyed by BES-I in contrast to previous and future programs.

In terms of locating the critical point, BES-I succeeded at detecting non-monotonic variation with collision energy in $\kappa\sigma^2$ of the net-proton number with a 3.0σ significance for the most central Au+Au collisions, one of the suggested signatures for the critical point [78].

The first step in the process was measuring the event-by-event net-proton ($N_p - N_{\bar{p}}$) distributions, shown in Figure 2.9 for the most central collisions in the transverse momentum range $0.4 < p_T(GeV/c) < 2.0$ at different collision energies. The wealth of data collected for the net-proton distributions allowed for the calculations of cumulants (C_n) of up to fourth order as a function of $\sqrt{s_{NN}}$, where

$$C_1 = M \qquad C_2 = \sigma^2$$

$$C_3 = S\sigma^3 \qquad C_4 = \kappa\sigma^4$$

shown in Figure 2.10 as a function of collision energy for both central (head-on) and

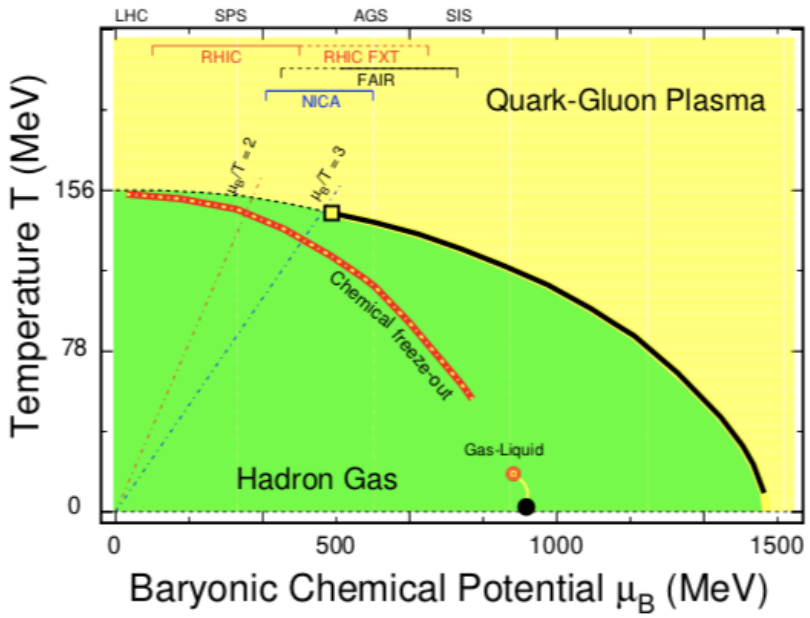

Figure 2.8: QCD phase diagram. The boundary between hadron gas and the QGP is indicated by the solid line for a first-order phase transition beginning at large μ_B and small T and ending at the proposed critical point. The crossover transition is indicated by the dashed line. The regions of $\mu_B/T \leq 2$ and 3 are shown as red and blue dot-dashed lines, respectively. These lines are of significance because comparison between lattice calculations and RHIC data strongly disfavors a critical point in the region $\mu_B/T \leq 2$ [76, 77].

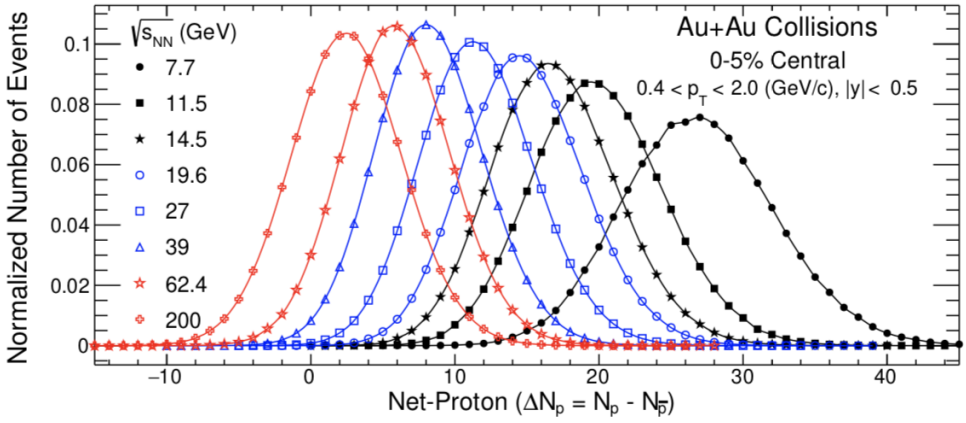

Figure 2.9: Event-by-event net-proton number distributions for central Au+Au collisions at different nine collision energy values measured by the STAR collaboration. The distributions are normalized to the total number of events at each collision energy. The statistical uncertainties are smaller than the symbol sizes and the lines are to guide the eye [78].

peripheral collisions.

Large values for higher order cumulants C_3 and C_4 of the net-proton distribution of central collisions are an indication that the distributions deviate significantly from the standard Gaussian. This was considered by the STAR collaboration to be the first evidence of augmented fluctuations due to the presence of a critical point, as predicted by theoretical models [79, 80]. On the other hand, cumulant values for peripheral collisions were close to zero. This could be due to the fact that peripheral collisions may not reach a state that is hot and dense enough to drive a phase transition. In terms of dependence, C_1 and C_3 decrease monotonically with $\sqrt{s_{NN}}$, while C_2 and C_4 vary non-monotonically with collision energy. In order to eliminate first-order volume variations and relate cumulants to baryon number susceptibilities, the following ratios were calculated [81],

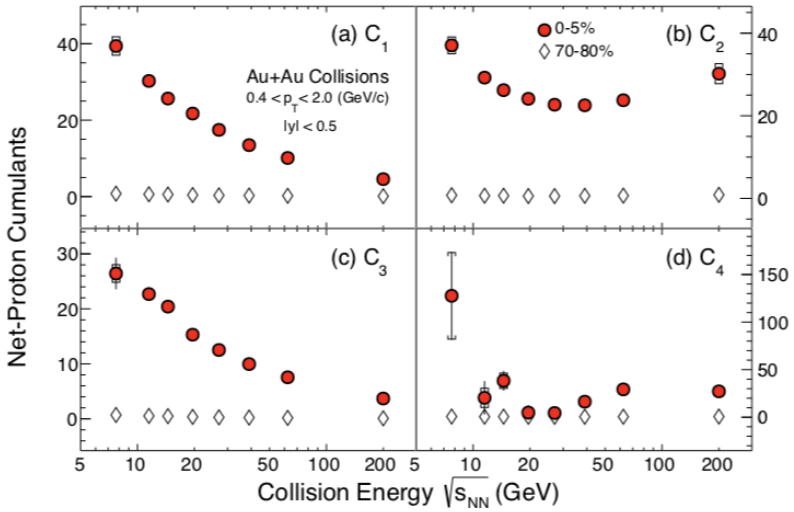

Figure 2.10: Cumulants of the net-proton distributions for central (0-5%) and peripheral (70- 80%) collisions as a function of collision energy. The vertical bars represent the statistical uncertainties and the caps correspond to the systematic uncertainties [78].

$$\frac{C_3}{C_2} = S\sigma = \frac{\chi_3^B}{\chi_2^B}, \qquad \frac{C_4}{C_2} = \kappa\sigma^2 = \frac{\chi_4^B}{\chi_2^B}.$$

Figure 2.11 shows the net-proton $S\sigma$ and $\kappa\sigma^2$ values for both central and peripheral collisions, as well as UrQMD [82] and hadron resonance gas model [83] predictions which did not include a critical point. As expected, peripheral collisions vary monotonically with $\sqrt{s_{NN}}$, with $\kappa\sigma^2$ values below unity (statistical baseline). In central collisions, there is a clear non-monotonic pattern in $\kappa\sigma^2$ with respect to collision energy, with values dipping below unity and then rising above unity again as collision energy increases. In order to determine the significance of this deviation, the data for $\kappa\sigma^2$ was modeled by a polynomial function of order three in the $\sqrt{s_{NN}}$ range of 7.7 - 62.4 GeV, where the non-monotonic behavior is predominant. The

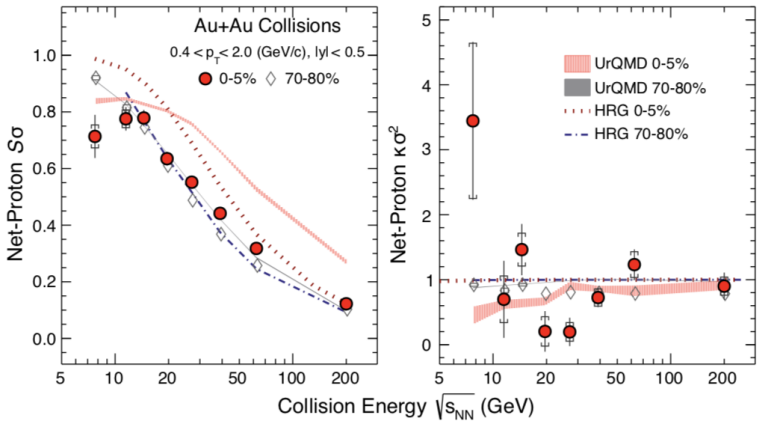

Figure 2.11: $S\sigma$ on the left and $\kappa\sigma^2$ on the right as a function of collision energy for net-proton distributions measured in Au+Au collisions. Both central and peripheral collisions are shown. The error bars and caps show statistical and systematic uncertainties, respectively. The vertical-dashed (central) and dash-dotted (peripheral) lines correspond to results from a hadron resonance gas (HRG) model. The orange (central) and black (peripheral) shaded bands are the results from a UrQMD calculation, which do not include a phase transition or a critical point [78].

polynomial is in the form $\Sigma_n P_n(\sqrt{s_{NN}})^n, n = 0, 1, 2, 3$, the exact values for p_n can be found in Ref. [78].

The uncertainties for the derivatives of this polynomial were calculated based on the polynomial fitting and the overall significance of the change in the sign of the slope for $\kappa\sigma^2$ as a function of $\sqrt{s_{NN}}$ in the range of 7.7-62.4 GeV is 3σ. The statistical significance of the non-monotonic behavior of net-proton $\kappa\sigma^2$ for central collisions along with the deviation from UrQMD and HRG predictions that did not include a critical point, further solidifies the case for a possible CP signature.

In summary, BES-I resulted in the first measurements of non-monotonic behavior of the net-proton $\kappa\sigma^2$, which was used as a proxy for the net-baryon $\kappa\sigma^2$. These measurements are consistent with QCD-based models that include a critical point.

However, there are many caveats that come with using net-proton counts for this analysis. Firstly, the net-proton distributions obviously do not account for all baryons in the system. Secondly, there are significant interactions that happen between the point of collision and chemical freeze-out. Thirdly, there are finite size effects and acceptance cuts on the experimental side that could significantly affect the moments of the net-proton distribution – especially higher moments such as skewness and kurtosis. Although promising, fluctuation results from BES-I are simply not enough to confirm the existence of a critical point. This clear mismatch between what experiments can measure and what theoretical models can replicate in terms of CP signatures is what motivated the original work described in the next chapter.

Chapter 3

An Equation of State for QCD with a Critical Point

Preliminary results from first phase of the Beam Energy Scan showed hints of a first-order phase transition, which prompted improvements to detectors and statistics for the second phase of the program, BES-II, scheduled for 2019-2021. The determination of the phase structure of QCD, along with the existence and location of its critical point, remains one of the most important goals of high-energy nuclear physics leading up to BES-II.

A key factor that limits the analysis of critical signatures on the theoretical side is the lack of an Equation of State (EOS) that contains a critical point. Hydrodynamic simulations of the fireball created during heavy-ion collisions rely on an Equation of State to dictate the evolution of the system. Therefore, in order to account for critical phenomena, these simulations require an EOS that contains a critical point.

These results are imperative to the analysis of BES-II measurements because they would lead to precise calculations of the variations we expect to see in fluctuations as a function of $\sqrt{s_{NN}}$ and the probability that these signatures would survive final hadronic scatterings, both of which have yet to be carefully calculated.

There is much work that needs to be done in that direction, including adjustments in hydrodynamic calculations near the critical point [84, 85, 86, 87]. Once these modifications are quantified, an EOS that encompasses all current theoretical knowledge on the phase diagram as well as a parametrically chosen critical point would allow for a precise survey of collisions at BES-II energies.

The goal of this work was to produce a family of equations of state for QCD, each one of which contains a critical point in the region covered by BES-II while simultaneously respecting what is known from first-principle lattice QCD calculations up to order four in μ_B. This is the first model to account for both (i) the Taylor expansion of the QCD EOS from lattice calculations to describe a crossover phase transition and (ii) a first-principle model for the critical contribution. Previous studies have considered either the lattice Taylor expansion only [88, 89, 90] or models for the critical behavior in the vicinity of the CP [91, 92, 93], but not both at the same time.

3.1 Taylor Expanded Equation of State from Lattice QCD

The Equation of State for QCD is known with high precision at vanishing baryon chemical potential from lattice calculations with 2+1 (up, down + strange) [94, 95, 96] and 2+1+1 (up/down + strange + charm) [97] quark flavors present in the system. It is possible to extend the EOS at $\mu_B = 0$ to finite chemical potentials using a Taylor expansion about the temperature axis in terms of powers of the ratio μ_B/T [98, 99, 100, 101, 102]. For the pressure, the Taylor expansion is given by

$$P(T, \mu_B) = T^4 \sum_n c_{2n}(T) \Big(\frac{\mu_B}{T} \Big)^{2n}, \tag{3.1}$$

where the constant coefficients are the susceptibilities of the baryon number at vanishing baryon chemical potential,

$$c_n(T) = \frac{1}{n!} \frac{\partial^n P/T^4}{\partial(\mu_B/T)^n} \bigg|_{\mu_B=0} = \frac{1}{n!} \chi_n(T). \tag{3.2}$$

In this expansion, all odd derivatives of the pressure at $\mu_B = 0$ cancel out due to the charge conjugation ($\mu_B = -\mu_B$) symmetry of the QCD partition function.

These coefficients have been calculated at both finite lattice spacing [100, 103, 104] and in the continuum limit [77, 105], where the lattice spacing is approximately zero. Figure 3.1 shows results from $c_n, n = 0, 2, 4, 6$ as a function of temperature from the Wuppertal-Budapest collaboration [88].

The Taylor expansion method provides an alternative to direct first-principle calculations at finite density, which are subject to the fermion sign problem, or

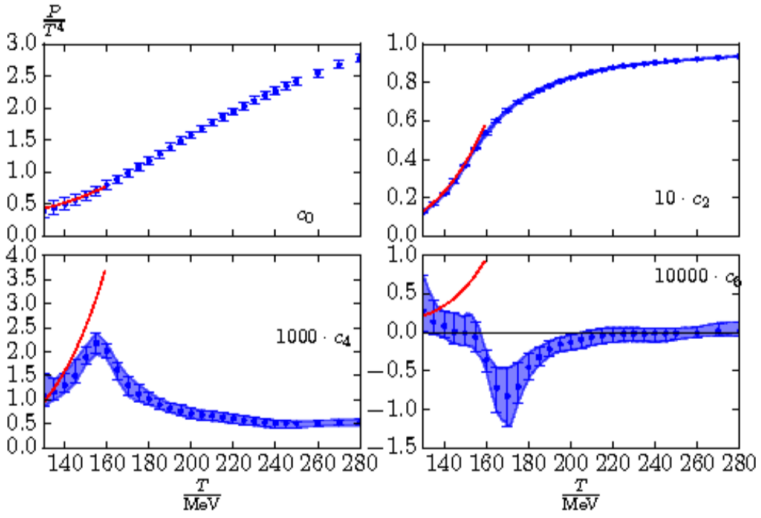

Figure 3.1: $c_n, n = 0, 2, 4, 6$, as functions of the temperature, from the Wuppertal-Budapest collaboration [88].

complex action problem. This is due to the fact that, at finite density, the weight used for importance sampling in Monte Carlo integration over lattice QCD configurations, becomes complex, which makes simulations at finite chemical potential extremely difficult.

The Taylor expansion can be useful in putting constraints on the location of the critical point. If we assume that the critical point is the closest singularity to the $\mu_B = 0$ axis in the complex μ_B plane, the radius of convergence of the Taylor expansion should lead to an indication of the location of the critical point. Because only a few coefficients are known, the only result in that direction is an indication that the region in the phase diagram for which $\mu_B \lessapprox 2T$ in unlikely to contain a critical point [77]. In terms of knowledge of the critical region, that is as much information as the Taylor expansion can provide; since it cannot reproduce a singularity, this

method is not useful in the analysis of the QCD EOS beyond the critical point.

With all this in mind, it is clear that a more sophisticated approach is needed to model the QCD phase diagram at intermediate and high densities. The first issue one runs into is how to account for the correct critical behavior when the critical point itself is still an unknown feature of the theory of quantum chromodynamics.

3.2 A Critical Point from the 3D Ising Model

Though the QCD critical point cannot yet be understood from first-principle methods, it is possible to make inferences about the expected critical behavior based on universality arguments. The principle of universality allows for theories with completely different dynamics to share the same critical behavior, as long as they have the same degrees of freedom and underlying symmetries. The deeper implication is that the critical behavior of a system is dictated by universal features of the theory, not by how its different degrees of freedom interact.

The universality principle allows for theories to be grouped in universality classes. Theories in the same universality class share a set of critical exponents, which characterize the thermodynamics of the system in the vicinity of a critical point. Since QCD is expected to be in the same universality class as the 3D Ising model [106], it is possible to construct an equation of state for QCD with a critical point in the correct universality class and therefore account for the appropriate critical behavior.

The phase diagram for the Ising model of ferromagnets, shown in Figure 3.2,

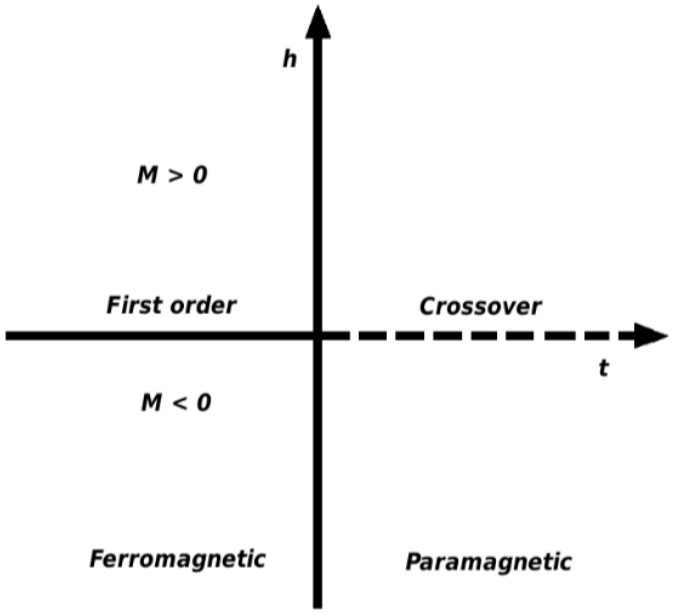

Figure 3.2: Schematic representation of the phase diagram for the Ising model of ferromagnets

is typically represented in terms of the reduced temperature, t, and the reduced magnetic field, h, where

$$t = \frac{T - T_C}{T_C}, \tag{3.3}$$

$$h = \frac{H}{k_B T_C}, \tag{3.4}$$

for which T is the temperature, T_C is the critical temperature, H is the magnetic field, and k_B is the Boltzmann constant.

In this phase diagram, negative t values correspond to a first-order phase transition between negative/positive magnetization (ferromagnetic regime), while positive

t yields a smooth crossover (paramagnetic regime). In the neighborhood of the critical point, the system becomes scale invariant and its underlying properties are no longer important, as relevant thermodynamic quantities scale according to a set of power laws and critical exponents. The following are some of these critical exponents and how they relate to the behavior of the system in the vicinity of the critical point:

- α determines the behavior of the specific heat on the $h = 0$ axis, which scales as $C \sim |t|^{\alpha}$;
- β drives the scaling of the spontaneous magnetization, $M \sim (-t)^{\beta}$;
- γ dictates the behavior of the zero field susceptibility $\chi \equiv \left(\frac{\partial M}{\partial H}\right)_{H=0} \sim |t|^{-\gamma}$;
- δ rules the scaling of the magnetization along the h-axis, $M \sim \text{sign}(h)|h|^{1/\delta}$.

The critical point from the 3D Ising model is the key element in this work. It allows us to account for the correct expected critical behavior in addition to what is known from lattice QCD.

3.3 Methodology: A Family of Equations of State for QCD

The result of this work is a family of equations of state for QCD, which match what we know from lattice QCD results up to fourth order in μ_B, $\mathcal{O}(\mu_B^4)$, in the region where it applies, and include a critical point from the correct universality class. This was accomplished through the following strategy:

I. Choose a location in the phase diagram, (μ_{BC}, T_C), at which to put a critical point;

II. define a suitable parametrization to describe the universal scaling behavior of the Equation of State in the 3D Ising model near the critical point;

III. map the 3D Ising model phase diagram onto the QCD phase diagram via a parametric change of variables;

IV. use the thermodynamics of the Ising model EOS to estimate the critical contribution to the expansion coefficients up to $\mathcal{O}(\mu_B^4)$ from lattice QCD;

V. reconstruct the full pressure, matching lattice QCD up to $\mathcal{O}(\mu_B^4)$ at $\mu_B = 0$ and including the correct critical behavior.

This approach is similar to and based on Refs. [107, 108], but differs from these previous efforts in that the critical contribution is built on top of a first-principle result from lattice QCD, instead of relying on additional modeling.

It is important to highlight that this method assumes that the critical point of QCD is the closest singularity to $\mu_B = 0$ on the real μ_B axis. Only under this assumption are we allowed to construct the EOS as detailed above. Additionally, the placement of the critical point in each equation of state is done by construction, meaning that no inferences or predictions regarding the existence or location of the critical point can be made using the EOS alone. Instead of being a direct path towards determining the properties of a possible QCD critical point, we present a *tool* that can be used in conjunction with hydrodynamic simulations and comparisons

to experimental results to assist in this goal.

3.3.1 Scaling the 3D Ising Model EOS

In order to formulate a suitable parametrization of the Ising model EOS, we introduce the variables R and θ, and define a map between these two variables and the Ising variables (r, h)[1]:

$$M = M_0 R^\beta \theta, \tag{3.5}$$

$$h = h_0 R^{\beta\delta} \tilde{h}(\theta), \tag{3.6}$$

$$r = R(1 - \theta^2), \tag{3.7}$$

where M_0, h_0 are normalization constants, and

$$\tilde{h}(\theta) = \theta(1 + a\theta^2 + b\theta^4),$$

$$a = -0.76201, b = 0.00804.$$

The 3D Ising critical exponents are $\beta \simeq 0.326$ and $\delta \simeq 4.80$, and the possible values for new parameters are $R \geq 0$ and $|\theta| \leq \theta_0 \simeq 1.154$, where θ_0 is the nontrivial zero of $\tilde{h}(\theta)$. Additionally, the values of the normalization constants are such that

$$M(r = -1, h = 0^+) = 1,$$

$$M(r = 0, h) \propto \text{sign}(h)|h|^{1/\delta},$$

which yields $M_0 \simeq 0.605$ and $h_0 \simeq 0.394$. This parametrization accounts for the correct behavior of the magnetization, M, as a function of r and h [107, 108, 109, 110].

[1]The reduced temperature variable is referred to as r from here on.

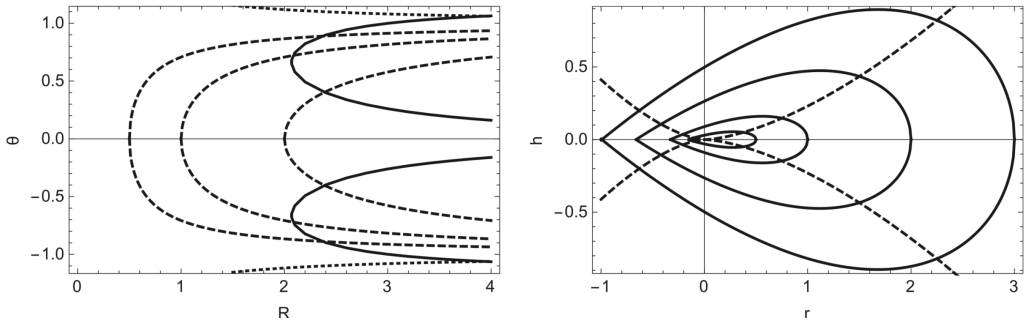

Figure 3.3: Visual representation of the parametrization defined in Eqs. (3.5-3.7.) Left: lines of constant h and r in the $\theta - R$ plane, with solid and dashed lines, respectively. Right: lines of constant θ and R in the $h - r$ plane, with dashed and solid lines, respectively.

Figure 3.3 shows a map of the parametrization defined in Eqs. 3.5-3.7, with lines of constant h and r in the $\theta - R$ plane and lines of constant θ and R in the $h - r$ plane.

The goal is to obtain an expression for the pressure of the system. Starting from our parametrization, the Gibbs free energy density is

$$G(h, r) = F(M, r) - Mh, \tag{3.8}$$

where $F(M, r)$ is the free energy density,

$$F(M, r) = h_0 M_0 R^{2-\alpha} g(\theta), \tag{3.9}$$

where $\alpha \simeq 0.11$ is another critical exponent, for which the relationship $2-\alpha = \beta(\delta+1)$ holds. Hence, we only need to solve for the function $g(\theta)$ to obtain an expression for the Gibbs free energy density. This can be done using the fact that $h = (\partial F/\partial M)_h$, which yields the differential equation

$$\tilde{h}(\theta)(1 - \theta^2 + 2\beta\theta^2) = 2(2 - \alpha)\theta g(\theta) + (1 - \theta^2)g'(\theta). \tag{3.10}$$

The solution is simply

$$g(\theta) = c_0 + c_1(1-\theta^2) + c_2(1-\theta^2)^2 + c_3(1-\theta^2)^3, \tag{3.11}$$

with

$$\begin{aligned}
c_0 &= \frac{\beta}{1-\alpha}(1+a+b), \\
c_1 &= -\frac{1}{2}\frac{1}{\alpha-1}\{(1-2\beta)(1+a+b) - 2\beta(1+2b)\}, \\
c_2 &= -\frac{1}{2\alpha}\{2\beta b - (1-2\beta)(a+2b)\}, \\
c_3 &= -\frac{1}{2(\alpha+1)}b(1-2\beta).
\end{aligned}$$

With all factors determined, the expression for the pressure in the 3D Ising model in terms of the scaling parameters R and θ can be constructed by noticing that the Gibbs free energy density is equivalent to the negative of the pressure, $G = -P$, hence

$$P_{\text{Ising}}(R,\theta) = h_0 M_0 R^{2-\alpha}[\theta\tilde{h}(\theta) - g(\theta)]. \tag{3.12}$$

This expression is dimensionless and completely analytic in (R,θ) in the range of parameter values. However, the map $(R,\theta) \longmapsto (r,h)$ is not globally invertible.

3.3.2 Mapping Ising Variables to QCD Variables

Next, we want to map Ising variables to QCD coordinates. The goal is use Eq. (3.12) to derive the critical contribution to thermodynamic observables. In this map, the critical point of the 3D Ising model ($r = 0, h = 0$) will correspond to the critical

point of QCD, whatever its location may be. Additionally, the lines or first-order phase transition and crossover in the Ising model must match those in the QCD phase diagram.

The simplest map that meets these requirements is a linear map in the form [111]:

$$\frac{T - T_C}{T_C} = w(r\rho \sin\alpha_1 + h \sin\alpha_2), \tag{3.13}$$

$$\frac{\mu_B - \mu_{BC}}{T_C} = w(-r\rho \cos\alpha_1 - h \cos\alpha_2), \tag{3.14}$$

which can be visualized in Figure 3.4. There are six parameters involved in the mapping, two of which, (T_C, μ_{BC}), correspond to the location of the critical point on the QCD phase diagram. The remaining parameters are scale factors, w and ρ, which determine the size and shape of the critical region[2], and the angles that the r and h axes form with lines of constant T, α_1 and α_2.

Now that we have mapped Ising variables to QCD variables, the result is the double map

$$(R, \theta) \longmapsto (r, h) \longleftrightarrow (T, \mu_B). \tag{3.15}$$

In order to apply the thermodynamics we developed for the Ising model to our problem, we need an expression for $T(R, \theta)$ and $\mu_B(R, \theta)$. Unfortunately, because only the second step in our map is globally invertible, this cannot be achieved analytically. Hence, we need to solve the following expressions for each point in the

[2] w is a *global* scaling factor for the variables r and h, so it determines the size and contribution of the critical region with respect to the QCD phase diagram. ρ is a *relative* scaling factor, so it roughly determines the shape of the critical region.

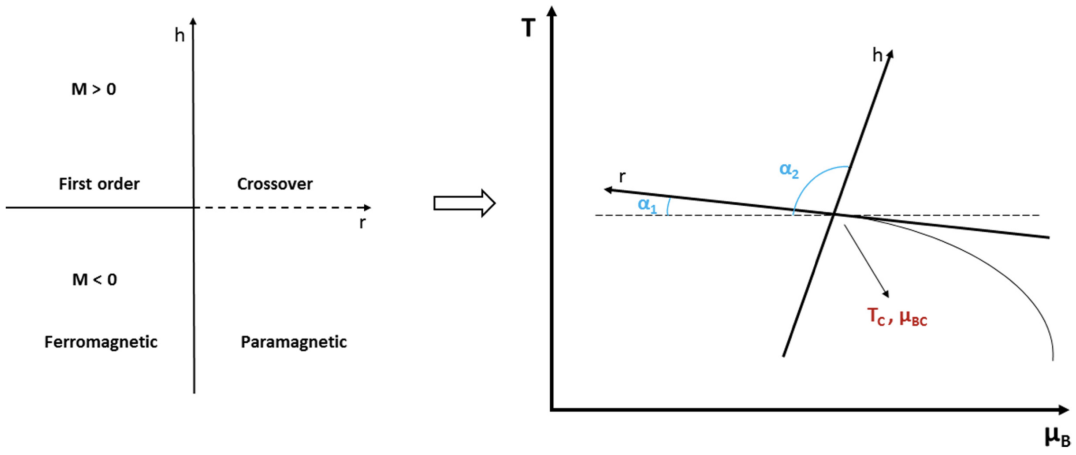

Figure 3.4: Illustration of the non-universal map between Ising and QCD variables.

QCD phase diagram:

$$T(R,\theta) - T_i = 0, \tag{3.16}$$

$$\mu_B(R,\theta) - \mu_{Bi} = 0. \tag{3.17}$$

We proceed by (i) choosing a range of interest for T and μ_B (ii) given a choice of the paramters in the Ising-QCD map, we solve Eqs. (3.16) and (3.17) numerically for a two-dimensional grid in T and μ_B in the desired range, which results in a discrete inverse map $(T, \mu_B) \longmapsto (R, \theta)$. Though this solution is not analytic, it allows us to convert the thermodynamics of the 3D Ising model in terms of (R, θ) to QCD variables, given a choice of parameters for the map (Eqs. (3.13) and (3.14).)

3.3.3 Strategy for Obtaining the Thermodynamic Behavior

Our two starting "ingredients" for the EOS are the lattice coefficients at vanishing baryonic potential and the parametrized Ising contribution. Clearly, we need to

merge those two components in order to produce an equation of state for QCD that satisfies our requirements.

We begin by rewriting the Taylor expansion coefficients in Eq. (3.1) as the sum of an "Ising" contribution coming from the critical point of QCD and a "non-Ising" contribution, which contains any other behavior including other criticality present in the $T - \mu_B$ region of interest. Mathematically, this can be expressed as

$$T^4 c_n^{\text{LAT}} = T^4 c_n^{\text{non-Ising}} + f(T, \mu_B = 0) c_n^{\text{Ising}}, \tag{3.18}$$

where $f(T, \mu_B = 0)$ is a regular function of the temperature and chemical potential, with dimension of energy to the fourth power.

Eq. (3.18) allows us to obtain the non-Ising coefficients, which we use to build a Taylor expansion in μ_B, analagous to the lattice one. The advantage of using the non-Ising coefficients is that the expansion can be pushed to larger values in μ_B, since the contribution from the critical point is removed. The result of this procedure is an expression for the non-Ising pressure of a broad region of the phase diagram. The critical behavior is introduced separately, under the assumption that the critical contribution to the Taylor coefficients from lattice QCD can be obtained by enforcing the correct scaling behavior in the vicinity of the critical point.

The full pressure can obtained by adding the critical contribution at any point in the $T - \mu_B$ plane to the Taylor expansion of the non-Ising pressure:

$$P(T, \mu_B) = T^4 \sum_n c_{2n}^{\text{non-Ising}}(T) \left(\frac{\mu_B}{T}\right)^{2n} + P_{\text{crit}}^{\text{QCD}}(T, \mu_B), \tag{3.19}$$

where the critical pressure is obtained from Eq. (3.12) using the map in Eq. (3.15) and multiplication by the function $f(T, \mu_B)$ in Eq. (3.18):

$$P_{\text{crit}}^{\text{QCD}}(T, \mu_B) = f(T, \mu_B) P^{\text{Ising}}(R(T, \mu_B), \theta(T, \mu_B)). \tag{3.20}$$

Since the choice for the function $f(\mu_B)$ is largely arbitrary, we consider the simplest choice,

$$f(T, \mu_B) = T_C^4. \tag{3.21}$$

At this point, it is important to note that not every choice of parameters will result in a thermodynamically stable model. The only property guaranteed by this procedure is that, for any choice of parameters, the coefficients at $\mu_B = 0$ match what we known from lattice QCD. Ensuring thermodynamic stability requires additional steps, which will be discussed in detail in Chapter 4.

3.3.4 Taylor Coefficients in the Ising Model

In order to obtain the contributions to the expansion coefficients of the pressure from the Ising model, we need to calculate the derivatives of the pressure with respect to baryon chemical potential at fixed temperature:

$$c_n^{\text{Ising}}(T) = \frac{1}{n!} T^n \frac{\partial^n P^{\text{Ising}}}{\partial \mu_B^n}\bigg|_{\mu_B=0} = \frac{1}{n!} \chi_n^{\text{Ising}}(T). \tag{3.22}$$

Though the expression we obtained for the critical pressure is terms of the variables (R, θ), not (r, h) or (T, μ_B), we can use the rules for the derivative of the

inverse and the multivariate chain rule to obtain each term as an analytic function of (R, θ). Once all terms are calculated, we can use Eqs. (3.16) and (3.17) to convert all quantities back to QCD coordinates.

For instance, the following expressions need to be calculated,

$$\chi_n(T, \mu_B = 0) = -T^n \left(\frac{\partial^n G}{\partial \mu_B^n} \right)_T .$$

If we take $n = 1$, the expression can be rewritten as

$$\frac{\chi_1}{T} = \left(\frac{\partial G}{\partial \mu_B} \right)_T = -\left(\frac{\partial G}{\partial r} \right)_h \frac{\partial r}{\partial \mu_B} - \left(\frac{\partial G}{\partial h} \right)_r \frac{\partial h}{\partial \mu_B}, \tag{3.23}$$

where

$$\left(\frac{\partial G}{\partial r} \right)_h = \frac{\partial G}{\partial R} \left(\frac{\partial R}{\partial r} \right)_h + \frac{\partial G}{\partial \theta} \left(\frac{\partial \theta}{\partial r} \right)_h ,$$
$$\left(\frac{\partial G}{\partial h} \right)_r = \frac{\partial G}{\partial R} \left(\frac{\partial R}{\partial h} \right)_r + \frac{\partial G}{\partial \theta} \left(\frac{\partial \theta}{\partial h} \right)_r .$$

Next, we need to find explicit expressions for the dependence of (R, θ) on (r, h). This can be accomplished by (i) using the rule for the derivative of the inverse, which will allows us to express derivatives of (R, θ) with respect to (r, h) as combinations of derivatives of (r, h) with respect to (R, θ), and (ii) using the rule for derivatives of a function with another function held constant.

First, let us define the rule for the derivative of the inverse. Let f_n be the n^{th} derivative of an invertible function that depends only on the variable x, $f = f(x)$,

$$f_n = \frac{d^n f}{dx^n}.$$

The following recursive relationship holds

$$f_1^{2n-1}\frac{d^n x}{dy^n} = P^n, \text{ with } P_{n+1} = f_1 P_n' - (2n-1) f_2 P_n, \tag{3.24}$$

where P_n are the polynomials in $\{f_k\}$ (e.g., $P_1 = 1$) and primed variables are differentiated with respect to x.

Take for example the second order derivative of R with respect to r. Though we do not know the dependence of R on r, using the relationship in Eq. (3.24), we see that it can be expressed as combinations of the derivatives that we do know, namely those of r with respect to R:

$$\left(\frac{\partial^2 R}{\partial r^2}\right)_h = -\left(\frac{\partial^2 r}{\partial R^2}\right)_h \left(\frac{\partial r}{\partial R}\right)_h^{-3}.$$

Lastly, we will use the following relationship for derivatives of a function with another function held constant:

$$\left(\frac{\partial}{\partial x_1}\right)_{y_1} y_2 = \left(\frac{\partial}{\partial x_1} + \left(\frac{dx_2}{dx_1}\right)_{y_1} \frac{\partial}{\partial x_2}\right) y_2. \tag{3.25}$$

In our case, (x_1, x_2) corresponds to (R, θ) and (y_1, y_2) to (r, h). Eq. (3.24) can be applied as follows:

$$\left(\frac{\partial h}{\partial R}\right)_r = \left[\frac{\partial}{\partial R} + \left(\frac{dR}{d\theta}\right)_r \frac{\partial}{\partial \theta}\right] h = \frac{h_0 R^{\beta\delta - 1}}{2\theta} \frac{1-\theta^2}{2\beta\delta\theta\tilde{h}(\theta) + (1-\theta^2)\tilde{h}'(\theta)}. \tag{3.26}$$

We can apply this relationship sequentially to obtain higher order derivatives. Although these derivatives increase in complexity quite rapidly as we get to higher order terms, they remain analytic in terms of the additional variables (R, θ). This allows us to have an expression for any these derivatives at any point in the QCD phase diagram.

3.3.5 Critical Contribution to the Pressure

Recall that because of charge conjugation symmetry, the QCD partition function needs to be an even function of the baryon chemical potential,

$$Z(T, -\mu_B) = Z(T, \mu_B) \tag{3.27}$$

which implies that the pressure is also an even function of μ_B. Thus, our equation of state needs to account for the fact that QCD must present a critical point at $-\mu_{BC}$ as well. The symmetric form of the pressure can be written as

$$P^{\text{crit}}_{\text{QCD}}(T, \mu_B) = \frac{1}{2} f(T, \mu_B) P^{\text{Ising}}_{\text{symm}}[R(T, \mu_B), \theta(T, \mu_B)] \tag{3.28}$$

$$= \frac{1}{2} f(T, \mu_B) \{P^{\text{Ising}}[R(T, \mu_B), \theta(T, \mu_B)] + P^{\text{Ising}}[R(T, -\mu_B), \theta(T, -\mu_B)]\}. \tag{3.29}$$

The definition as presented in Eq. (3.29) does not affect the singular critical behavior at the critical point. It does, however, ensure that odd-power coefficients in the Taylor expansion vanish, which is what we desire. This modification also makes the pressure at the critical point nonzero, whereas without the modification it would, by definition, be zero.

3.4 Parameter Choice

The previous section outlined the strategy used to produce the pressure across a range of temperatures and baryonic potentials in the QCD phase diagram. Now that we have a procedure to generate the EOS, we need to make a choice of parameters for

the Ising-to-QCD map. The choice of parameters is neither completely arbitrary nor irrelevant – it is a key part of the process, and constraining the parameter space can provide insight on physical properties of QCD through comparison with experimental data.

There are two ways to constrain the parameter space: i) applying existing knowledge about the QCD phase diagram and ii) studying the thermodynamic stability of the EOS produced. We will explore the latter in Chapter 4. The former largely reduces the array of acceptable parameters on its own. For instance, the decofinement temperature is $T \simeq 155$ MeV along the temperature axis [56]. In addition, the curvature of the transition line is negative [88, 112, 113], so we can safely infer that the critical temperature must be $T_C \lesssim 155$ MeV, and, as mentioned in Chapter 2, a critical point in the region $\mu_B \lesssim 2T$ seems to be strongly disfavored.

It is also expected that the curvature of the transition line is extremely small, hence the parameter α_1, which determines the angle between the r axis and lines of constant T, needs to be positive and very small. Unfortunately, we cannot make a similar argument for the second angle, which remains largely arbitrary. For simplicity, the results presented from here on are based on parameter sets for which $\alpha_2 - \alpha_1 = \pi/2$, meaning the $r - h$ axes are orthogonal.

In principle, the baryonic chemical potential at the critical point is not restricted by any physical properties. However, we restrain its value to the range of the BES-II program, $\mu_{BC} \lesssim 450$ MeV.

Lastly, we focus on the scaling parameters, w and ρ. These are certainly less

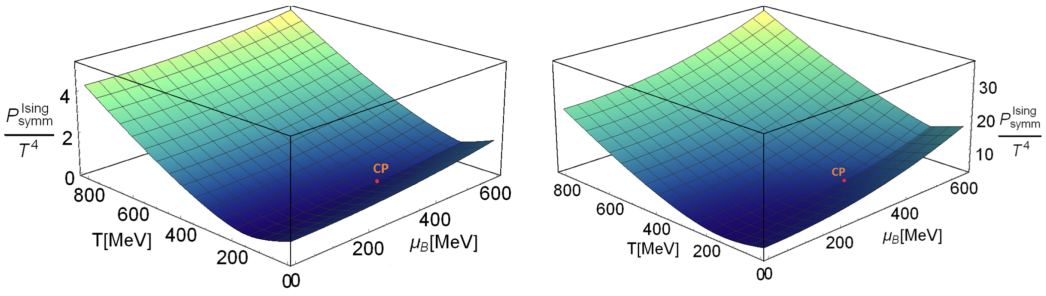

Figure 3.5: The pressure obtained with the mapping from the 3D Ising model and symmetrized around $\mu_B = 0$ for the choice of parameters $T_C \simeq 143.2$ MeV, $\mu_{BC} = 350$ MeV, $\alpha_1 = 3.85^o, \alpha_2 = 93.84^o$ (left), $w = 1$, and $\rho = 2$, and for a smaller value of $w = 0.25$ (right). We can see the singular behavior for $\mu_B > \mu_{BC}$, where the first-order transition occurs. A smaller value of the scaling parameter w corresponds to a larger Ising contribution to the pressure.

intuitive and due to the fact that the size and shape of the proposed critical region are unknown, we need to be careful imposing any restrictions. In general, using the $\mu_B = 0$ axis as reference, the effect of changing w while keeping ρ fixed is equivalent to moving closer or further away from the critical point. Particularly, because derivatives with respect to μ_B are proportional to $1/w$, a smaller w results in a larger Ising contribution to the pressure and its derivatives, i.e., a larger critical region. This effect is displayed in Figure 3.5, where a smaller w extends the critical region, such that the pressure grows faster in the T and μ_B directions. The other scaling parameter, ρ, dictates the behavior of the pressure and its derivatives along the temperature direction, moving away from the critical point. Currently, there are no constraints on how the scaling in the T and μ_B direction compare to one another, so the choice of ρ is mostly arbitrary.

3.4.1 Reducing the Number of Parameters

Given the knowledge presented above, it is possible to reduce the number of parameters in the Ising-to-QCD map from six to four. The transition line with an estimated negative curvature can be approximated by a parabola,

$$T = T_0 + \kappa T_0 \left(\frac{\mu_B}{T_0} \right)^2 + O(\mu_B^4), \tag{3.30}$$

where T_0 is the transition temperature and κ is the curvature of the transition line on the T axis. Using this approximation and a choice of μ_{BC}, T_C can be determined from Eq. (3.30) and α_1 is fixed by

$$\alpha_1 = \tan^{-1} \left(2 \frac{\kappa}{T_0} \mu_{BC} \right). \tag{3.31}$$

With the goal of illustrating the process, consider $\mu_{BC} = 350$ MeV, which is approximately in the middle of the range of chemical potentials covered by BES-II, and the value of κ calculated in Ref. [88]. This choice yields

$$T_C \simeq 143.2 MeV \quad \alpha_1 = 3.85^{\text{o}}. \tag{3.32}$$

Our choice to keep the $r - h$ axes orthogonal means that $\alpha_2 = 93.85^{\text{o}}$. Setting the scaling parameters to $w = 1$ and $\rho = 2$ results in the pressure shown in the left panel of Figure 3.5.

Using this procedure, for any choice of κ and μ_{BC}, T_C and α_1 can be fixed using Eqs. (3.30) and (3.31.)

3.4.2 Parametrization of Lattice QCD Results

In addition to the thermodynamics of the Ising model, we also need the Taylor coefficients from lattice QCD in order to calculate the pressure as defined in Eq. (3.19.) This work uses data from the Wuppertal-Budapest Collaboration [95, 114] for the pressure and its derivatives at $\mu_B = 0$. Unfortunately, the range of temperatures of the available lattice QCD results is too narrow to generate an EOS that meets the requirements of hydrodynamic simulations (30 MeV $\lesssim T \lesssim$ 800 MeV). The available data is also discrete, so some kind of smoothing needs to performed in order to ensure that the derivatives with respect to T and μ_B do not present any pathological or unphysical wiggly behavior.

We solved these issues using the following strategy:

I. For temperatures below the reach of lattice ($T \leq 135$ MeV), data was generated using the Hadron Resonance Gas (HRG) model.

II. The dependence of the pressure and its derivatives on the temperature was parametrized in the desired temperature range.

The zeroth and fourth order susceptibilities were parametrized using a ratio of fifth-order polynomials in the inverse temperature,

$$\chi_i(T) = \frac{a_0^i + a_1^i/t + a_2^i/t^2 + a_3^i/t^3 + a_4^i/t^4 + a_5^i/t^5}{b_0^i + b_1^i/t + b_2^i/t^2 + b_3^i/t^3 + b_4^i/t^4 + b_5^i/t^5}, \tag{3.33}$$

while the second order susceptibility was parametrized using the expression

$$\chi_2(T) = e^{-h_1/t' - h_2/t'^2} \cdot f_3 \cdot (1 + \tanh(f_4/t' + f_5)), \tag{3.34}$$

Table 3.1: Parametrization constants for $\chi_0(T)$, $\chi_4(T)$, and $\chi_2(T)$ in Eqs. (3.33) and (3.34.)

	$\chi_0(T)$	$\chi_4(T)$		$\chi_2(T)$
a_0	7.53891	0.0148438	h_1	0.325372
a_1	6.18858	0.0371572	h_2	0.497729
a_2	5.37961	0.0313008	f_3	0.148987
a_3	7.08750	0.0101907	f_4	6.66388
a_4	0.977970	0.00144661	f_5	5.07725
a_5	0.0302636	0.000159877		
b_0	2.24530	0.0673273		
b_1	6.02568	3.33723		
b_2	15.3737	13.6747		
b_3	19.6331	20.4745		
b_4	10.2400	13.6013		
b_5	0.799479	3.39819		

where $t = T/154$ MeV and $t' = T/200$ MeV [115]. Eqs. (3.33) and (3.34) were calculated from lattice/HRG data in the range $T = 5 - 500$ MeV and extrapolated to the range $T = 5 - 800$ MeV. The parametrization constants are given in Table 3.1.

The comparison of the parametrization to lattice and HRG results is shown in Figure 3.6. The HRG model used to calculate the behavior of the susceptibilities at low T does not take into account interactions and was constructed upon data from the most up-to-date particle list (PDG2016+ [116]) from the Particle Data Group. The smooth curves resulting from parametrizations are $c_n^{\mathrm{LAT}}(T)$ in Eq. (3.18), which were used to calculate $c_n^{\text{Non-Ising}}(T)$. This process is illustrated in Figure 3.7, which shows both contributions, Ising and non-Ising, to the parametrized lattice/HRG curves for the parameter choice $T_C = 143\,\mathrm{MeV}, \mu_{BC} = 350\,\mathrm{MeV}, \alpha_1 = 3.85°, \alpha_2 - \alpha_1 = 90°, w = 1$, and $\rho = 2$.

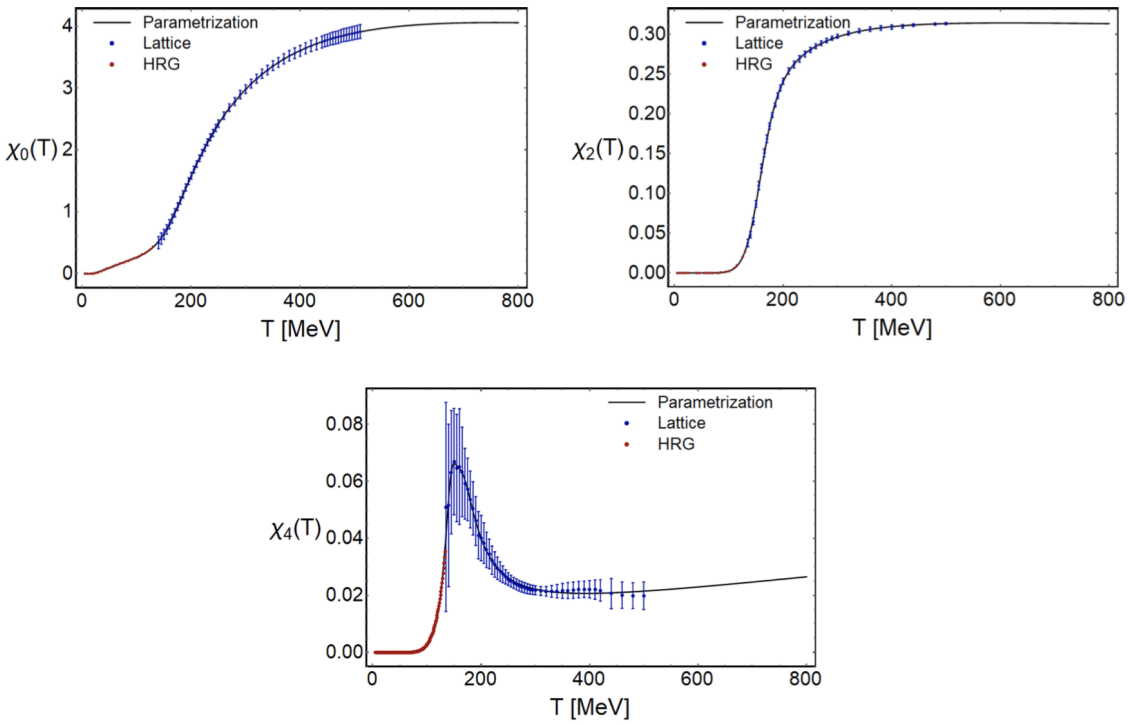

Figure 3.6: Parametrization of baryon susceptibilities from lattice QCD [95, 117] and HRG model calculations for the parameter choice $T_C = 143\,\mathrm{MeV}, \mu_{BC} = 350\,\mathrm{MeV}, \alpha_1 = 3.85°, \alpha_2 - \alpha_1 = 90°, w = 1$, and $\rho = 2$.

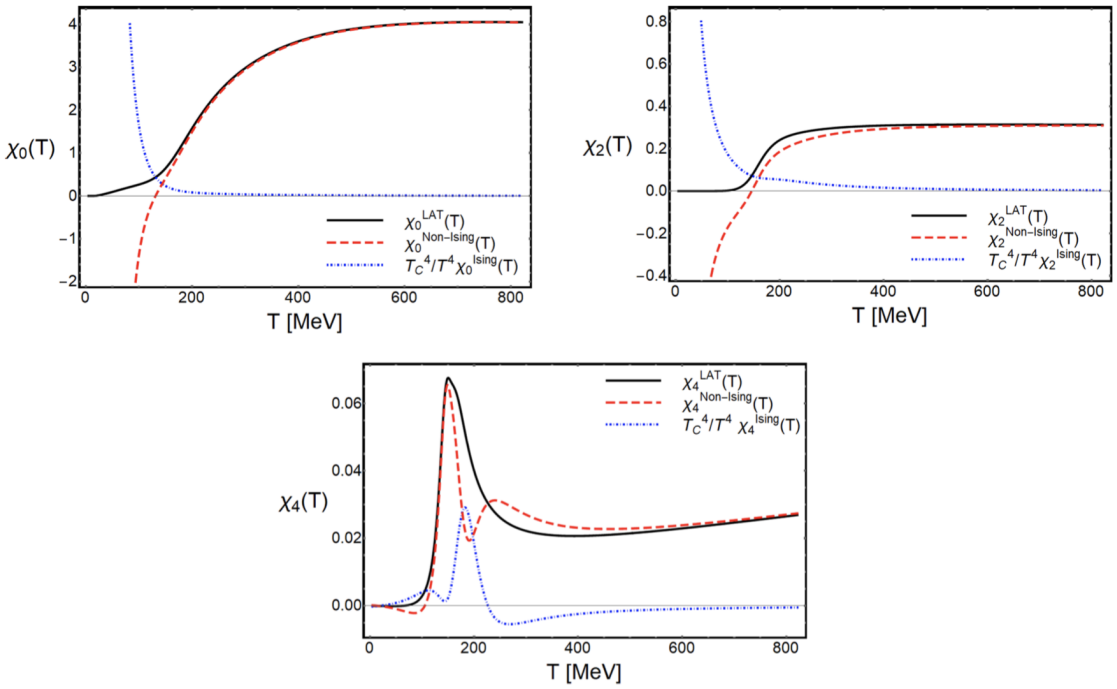

Figure 3.7: Comparison of critical (blue, dot-dashed) and non-Ising (red, dashed) contributions to baryon susceptibilities up to $\mathcal{O}(\mu_B^4)$ with the parametrized lattice data (black, solid).

3.5 Results

Now that all the components in Eq. (3.19),

$$P(T,\mu_B) = T^4 \sum_n c_{2n}^{\text{non-Ising}}(T)\Big(\frac{\mu_B}{T}\Big)^{2n} + P_{\text{crit}}^{\text{QCD}}(T,\mu_B),$$

have been obtained, an EOS can be generated for any choice of 6 or 4 (if the curvature of the transition line is fixed) parameters [118]. The equations of state are in the temperature range 30 MeV $\leq T \leq$ 800 MeV and in the chemical potential range 0 $\leq \mu_B \leq$ 450 MeV.

3.5.1 Correcting the EOS at low T

Unfortunately, because of our choice of $f(T,\mu_B)$, the Ising coefficients at low temperature follow a power law, while the ones from lattice calculations decrease exponentially. As a result, for some value of T, one or more of the non-Ising coefficients drops below zero, which leads to negative values for the pressure if the ratio (μ_B/T) is large enough. This becomes a problem especially in the regions where (μ_B/T) is very large.

To solve this issue, we rely on the fact that, in the region where (μ_B/T) is large, we can safely expect the system to be a hadron resonance gas. We perform a smooth merging of the pressure obtained through the Taylor expansion with the pressure as described by the HRG model using the hyperbolic tangent:

$$\frac{P_{\text{Final}}(T,\mu_B)}{T^4} = \frac{P(T,\mu_B)}{T^4}\frac{1}{2}\left[1+\tanh\frac{T-T'(\mu_B)}{\Delta T'}\right] + \frac{P_{\text{HRG}}(T,\mu_B)}{T^4}\frac{1}{2}\left[1+\tanh\frac{T-T'(\mu_B)}{\Delta T'}\right]. \tag{3.35}$$

Here, $T'(\mu_B)$ is the switching temperature and ΔT is the size of the overlap region, where both pressures contribute to the sum. We set the dependence of the switching temperature on the baryon chemical potential to be a parabola parallel to the transition line in Eq. (3.30):

$$T'(\mu_B) = T_0 + \frac{\kappa}{T_0}\mu_B^2 - T^*, \tag{3.36}$$

where T_0 and κ are the transition temperature and curvature of the transition line on the T axis. We choose $T^* = 23$ MeV and $\Delta T' = 17$ MeV in Eq. 3.35.

This correction eliminates the pathological behavior of the Taylor expansion at low values of T, while conserving the expected correct behavior in the chosen range of the phase diagram.

3.5.2 Full Thermodynamic Description

Now that we have a full description of the pressure, we can compute different thermodynamic observables for a complete description of the equation of state. We calculate the entropy density, baryon density, energy density, and speed of sound (normalized by the correct power of temperature):

$$\frac{S(T,\mu_B)}{T^3} = \frac{1}{T^3}\left(\frac{\partial P}{\partial T}\right)_{\mu_B} \tag{3.37}$$

$$\frac{n_B(T,\mu_B)}{T^3} = \frac{1}{T^3}\left(\frac{\partial P}{\partial \mu_B}\right)_{T} \tag{3.38}$$

$$\frac{\epsilon(T,\mu_B)}{T^4} = \frac{S}{T^3} - \frac{P}{T^4} + \frac{\mu_B}{T}\frac{n_B}{T^3} \tag{3.39}$$

$$c_s^2(T,\mu_B) = \left(\frac{\partial P}{\partial \epsilon}\right)_{S/n_B} \tag{3.40}$$

For the sake of simplicity, we rewrite the expression for the speed of sound in terms of derivatives of the pressure with respect to the temperature or the chemical potential [119]:

$$c_s^2 = \frac{n_B^2 \partial_T^2 P - 2S n_B \partial_T \partial_{\mu_B} P + S^2 \partial_{\mu_B}^2 P}{(\epsilon + P)[\partial_T^2 P \partial_{\mu_B}^2 P - (\partial_T \partial_{\mu_B} P)^2]}. \tag{3.41}$$

Figs. 3.8 show the pressure, entropy density, baryon density, energy density, and speed of sound in the ranges 30 MeV $\leq T \leq$ 800 MeV and $0 \leq \mu_B \leq$ 450 MeV using the parameters $T_C \simeq$ 143.2 MeV, $\mu_{BC} =$ 350 MeV, $\alpha_1 = 3.85^o, \alpha_2 = 93.84^\circ$ (left), $w = 1$, and $\rho = 2$. Figs. 3.9-3.11 show the same quantities for other possible choices of parameters. In Fig. 3.9, we see that choosing a larger w results in a smaller critical region (critical effects hardly appear in first order derivatives), whereas for a smaller w, as in Fig. 3.10, the critical effects are enhanced. Fig. 3.11 shows a different choice of location for the critical point, and we can see that the peaks and troughs associated with the critical point are also shifted.

Finally, although not very evident from the pressure, the critical point generally manifests itself clearly in first-order derivatives (entropy, baryon, and energy density), where the discontinuity due to a first-order phase transition is visible at $\mu_B > \mu_{BC}$. Furthermore, the speed of sound shows a clear dip at the critical point, as well as a (less evident) discontinuity at $\mu_B > \mu_{BC}$.

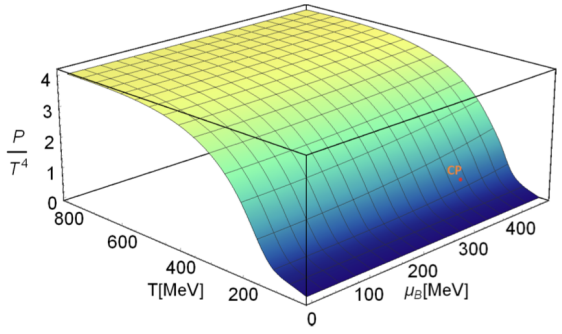

(a) Pressure.

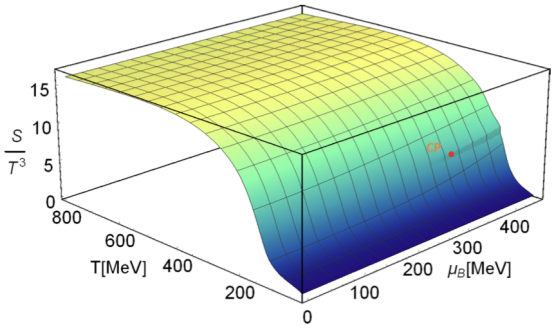

(b) Entropy density.

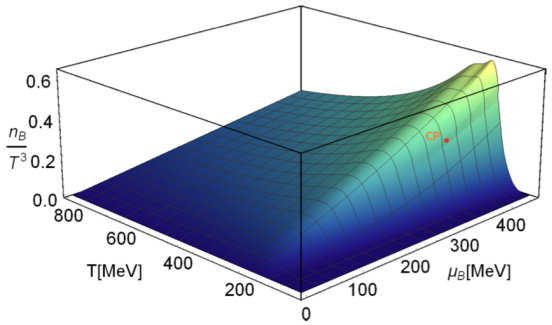

(c) Baryon density.

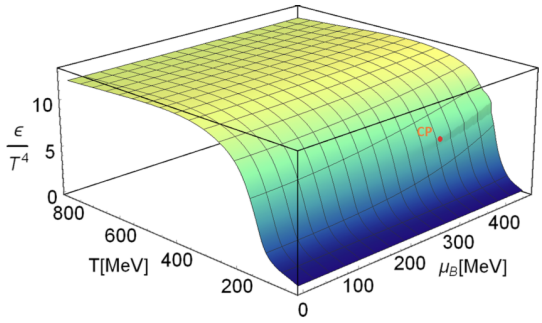

(d) Energy density.

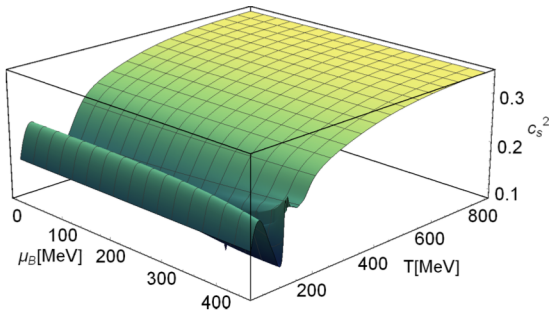

(e) Speed of sound.

Figure 3.8: All five thermodynamic quantities computed from the EOS given the choice of parameters specified in this section, after merging with HRG.

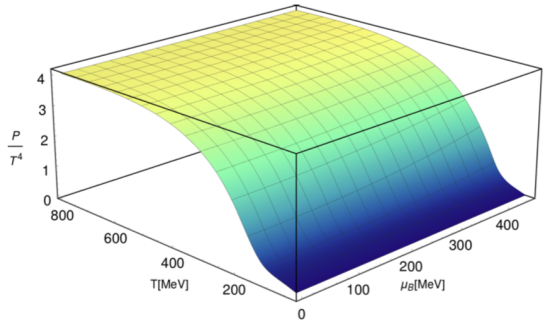

(a) Pressure.

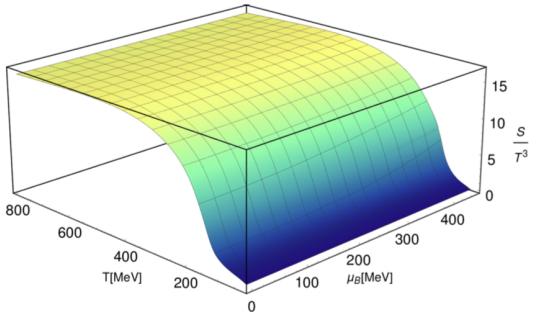

(b) Entropy density.

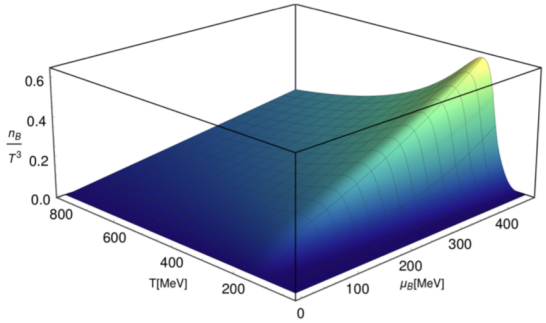

(c) Baryon density.

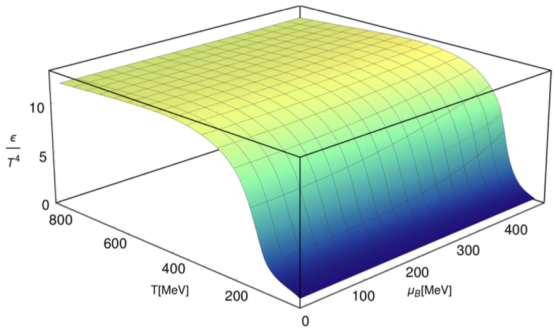

(d) Energy density.

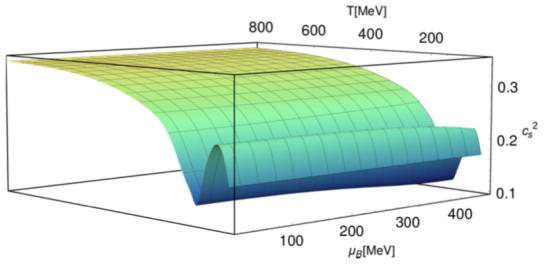

(e) Speed of sound.

Figure 3.9: All five thermodynamic quantities compute from the EOS with parameters corresponding to the same location of the CP and angles presented in Fig. 3.8, but with $w = 4$ and ρ= 1.

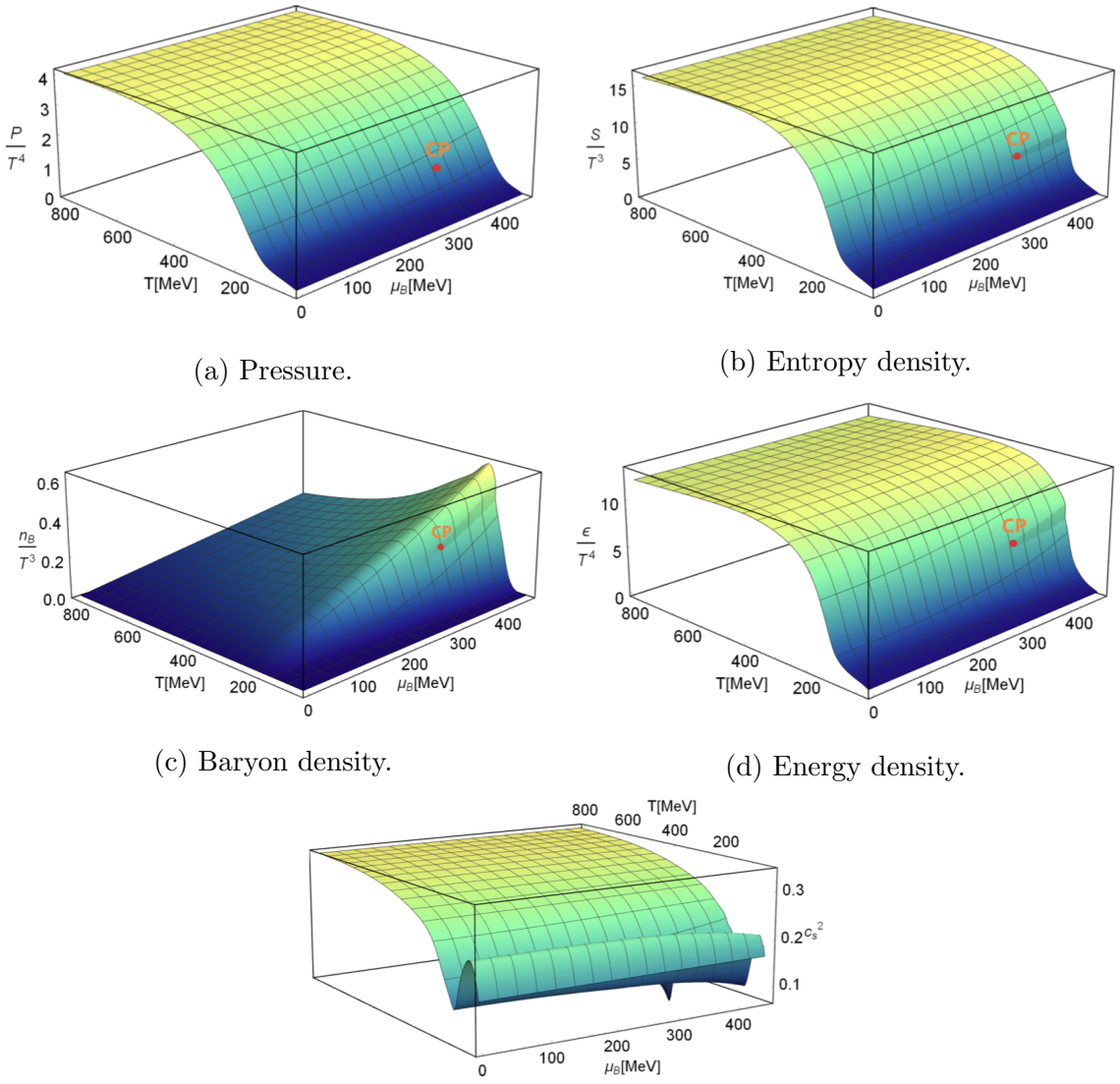

(a) Pressure.

(b) Entropy density.

(c) Baryon density.

(d) Energy density.

(e) Speed of sound.

Figure 3.10: All five thermodynamic quantities compute from the EOS with parameters corresponding to the same location of the CP and angles presented in Fig. 3.8, but with $w = 0.75$ and $\rho = 2$.

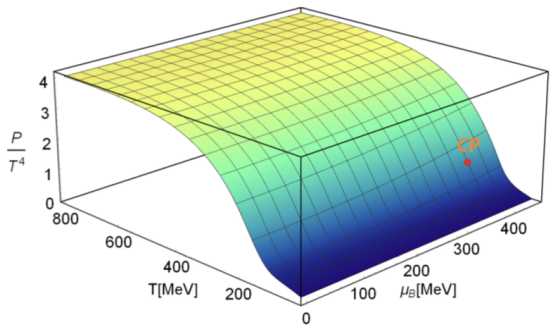

(a) Pressure.

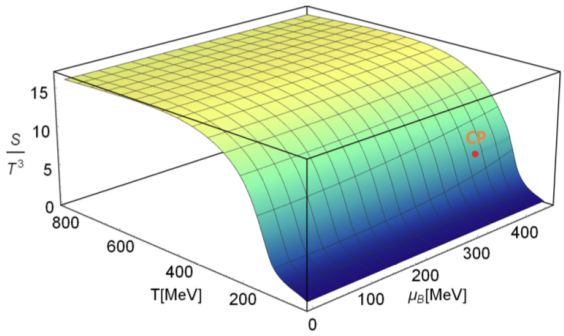

(b) Entropy density.

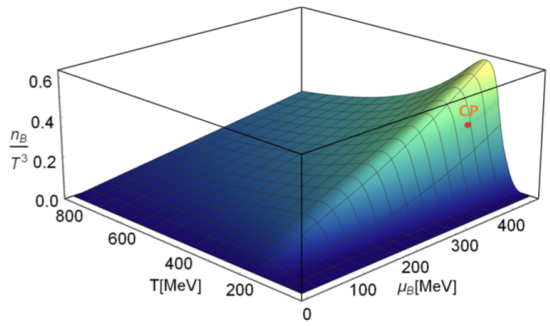

(c) Baryon density.

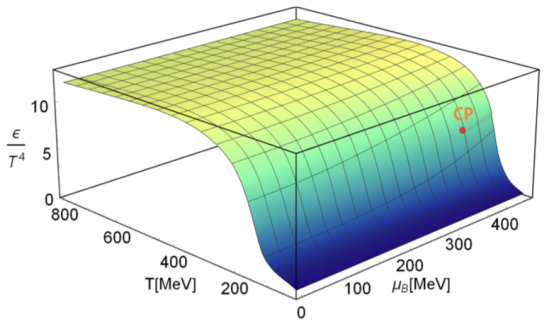

(d) Energy density.

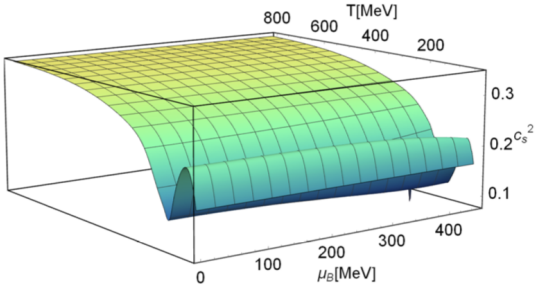

(e) Speed of sound.

Figure 3.11: All five thermodynamic quantities compute from the EOS with parameters corresponding to μ_{BC}= 400 MeV, $\alpha_1 \simeq 4.40^o$, $\alpha_2 - \alpha_1 = 90^o$, and $w = 2$, $\rho = 2$.

Chapter 4

Applications of the Equation of State

Now that an Equation of State with a critical point from the correct universality class is available [120], we can use it to (i) study critical effects on the thermodynamics of heavy-ion systems at different collision energies and temperatures, and (ii) take advantage of thermodynamic stability principles to constrain the size and shape of the critical region. The sections below detail how our EOS was used to provide insight on those two fronts ahead of BES-II results.

4.1 The Kurtosis of the Baryon Number

In Chapter 2, we introduced the idea that baryon susceptibilities diverge at the critical point and are therefore the most promising observable in the search for the

critical point. Particularly, promising data on $\kappa\sigma^2$ for the net-proton number resulted from BES-I, as this quantity clearly displays a dip in collision energies between 5-100 MeV (see Fig 2.11). Though the dip is of large statistical significance, it does not imply presence of a critical point on its own. Other explanations for the dip have been proposed, such as the effect of global conservation of baryon number, which is expected to play a bigger role at low collision energies where the system is smaller [121]. A dip has also been observed in finite μ_B Taylor expansions of lattice kurtosis calculations [76]. Additionally, transport models that do not include any criticality have been able to reproduce the decrease in $\kappa\sigma^2$ in finite densities [122], as shown in Fig. 4.1.

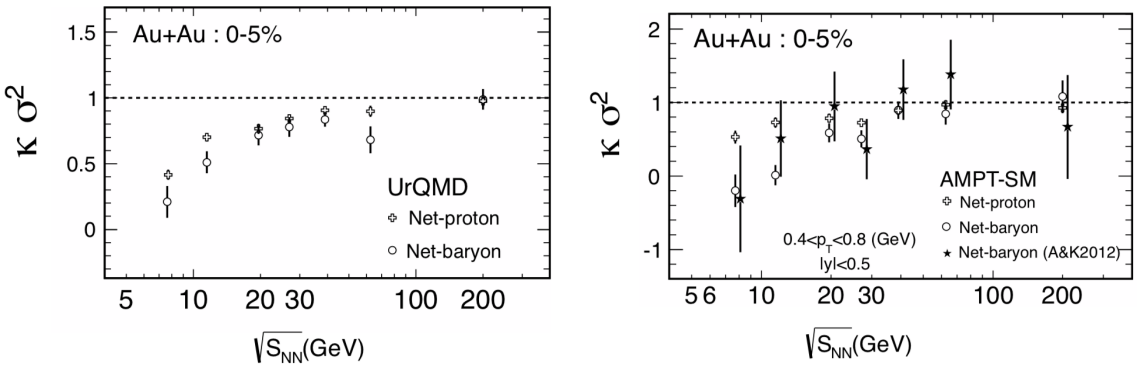

Figure 4.1: Energy dependence of $\kappa\sigma^2$ of net-proton and net-baryon distributions for 0-5% Au+Au collisions from the UrQMD (left) and the AMPT string melting model (right). Plots are from Ref. [122].

4.1.1 Predicting the Behavior of Conserved Charges

In heavy-ion collisions, the three conserved charges are baryon number (B), strangeness (S), and electric charge (Q). At vanishing baryon density, it is possible to calculate the higher order BSQ susceptibilities on the lattice and then use them to reconstruct the lower order ones at small finite baryon densities, which unfortunately has only been accomplished with large numerical uncertainties so far [123, 76, 124]. In addition, there are effective models capable of reproducing lattice QCD results that include a critical point at finite baryon density. Fig. 4.2 shows the predictions for the baryon susceptibilities from a holographic black hole engineering, which found a critical point at $T_C = 89$ MeV and $\mu_{BC} = 724$ MeV, where the peaks in χ_2 and χ_4 are evident near the critical point [125].

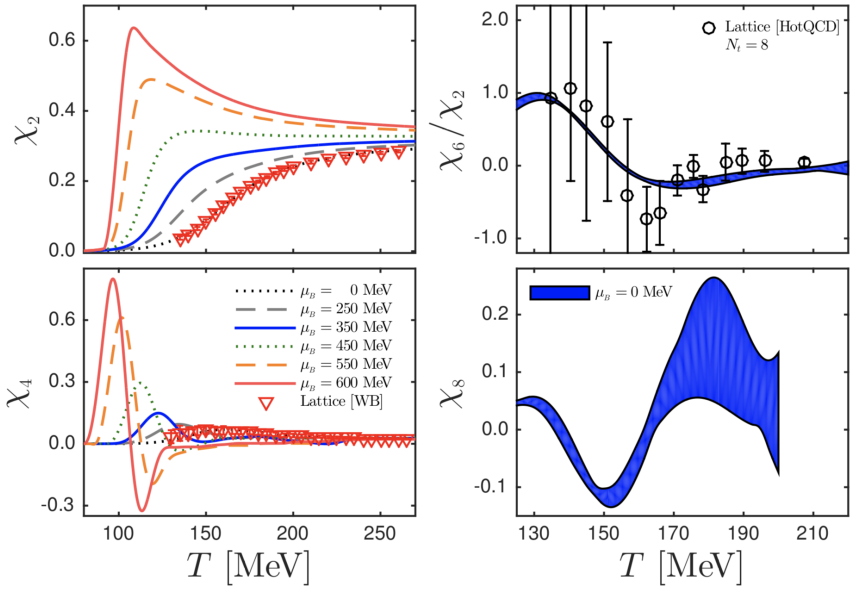

Figure 4.2: Baryon number susceptibilities as functions of the temperature for different values of the baryon chemical potential computed using holographic black hole engineering from Ref. [125].

An alternative is to employ the universality of the critical behavior. This approach has been used in Ref. [126], which proposes the non-monotonic behavior of the kurtosis κ of net-baryon number as a function of $\sqrt{s}$ as a potential critical point signature.

In that same work, it was shown that, up to the fourth order in the derivatives, the leading divergence term comes from the third derivative of the critical mode (the magnetization M) with respect to the magnetic field h at constant reduced temperature t:

$$\kappa(t,h) = \left(\frac{\partial^3 M}{\partial h^3}\right)_t . \tag{4.1}$$

The predicted behavior for κ along a parametrized freeze-out curve is shown in Fig. 4.3 in terms of the reduced temperature. With respect to the baryon chemical potential, the same curve, starting at $\mu_B = 0$ and passing close to the critical point would behave as follows. From its value at $\mu_B = 0$, κ is expected to decrease at increasing μ_B, then move upwards and reach a peak in the vicinity of the critical point.

The non-monotonic behavior of the kurtosis has been the main driving factor in the experimental search for the critical point since a similar signature was measured for $\kappa\sigma^2$ of the net-baryon number distribution during BES-I. Recall once again that the data from the STAR experiment in Fig. 2.11 show $\kappa\sigma^2$ decreasing and then swinging upwards as the collision energy decreases, similar to what is predicted in Ref. [126]

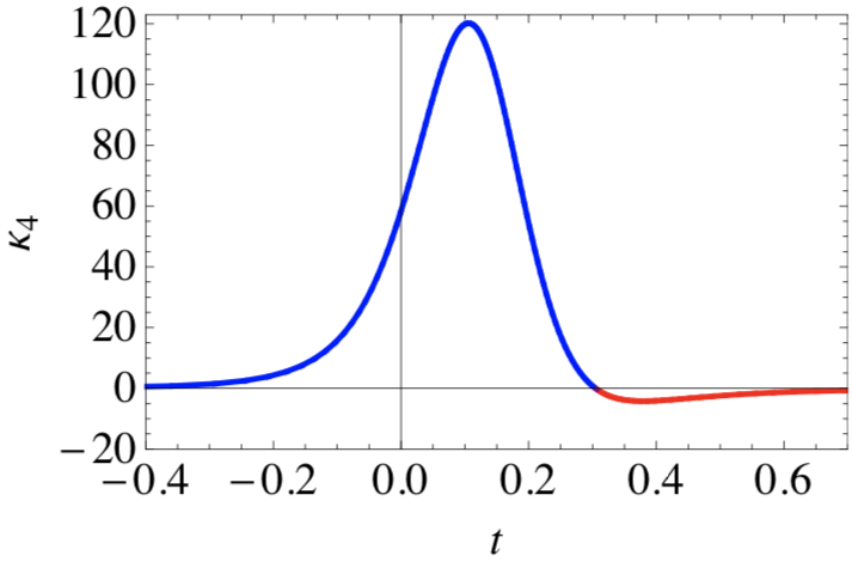

Figure 4.3: The dependence of the kurtosis, κ_4, on the reduced temperature, t, along the vertical dashed green line on the density plot above along an arbitrary freeze-out line from Ref. [126].

4.1.2 Why We Should Reconsider the Dip

Aside from possible explanations for the dip that do not require a critical point, the main caveat to the results obtained in Ref. [126] is that only the leading divergence terms were incorporated in the calculation of the kurtosis near the critical point. However, when mapping the 3D Ising model onto QCD, additional sub-leading terms appear because of the mixing between the two Ising variables, as discussed in Chapter 3.

Using the EOS with a critical point from the 3D Ising model, we found that these mixing terms are strictly sub-leading only in the immediate vicinity of the critical point, but can dominate elsewhere. The resulting overall kurtosis is thus different from what is obtained when only leading terms are considered. After including all

sub-leading expressions from the 3D Ising model critical point, we found that the decrease of the kurtosis along the crossover line leading to the critical point appears at temperature values larger or just barely incorporating the crossover line, making it difficult to observe it experimentally at the chemical freeze-out. However, we find that the divergence of the kurtosis at the critical point leads to a peak that can likely be measured along the freeze-out line. This is also consistent with the model presented in Ref. [125]. Therefore, it is worthwhile to focus experimental efforts not on the dip at intermediate collision energies, but rather on the rapid increase in the kurtosis, which appears to be the common critical signature between different analyses.

4.1.3 Results

From our EOS, we calculated the second and fourth susceptibilities of the baryon number, using the choice of parameters in Table 4.1. The location of the critical point was fixed at $\mu_{BC} = 420$ MeV, which results in $T_C \simeq 138$ MeV and $\alpha_1 \simeq 4.6°$, while several values of the parameters (w, ρ) were studied.

In addition, we consider two different choices for the relative angle between the (t, h) axes. First, we keep the two axes orthogonal ($\alpha_2 - \alpha_1 = 90°$), then we examine the case with the angle between the two axes $\alpha_2 - \alpha_1 = 330°$[1].

The second angle choice is interesting because the h axis is flipped in the map and the angle between the two axes, $\alpha_1 - \alpha_2 = -30°$ is small. This second point has

[1]The second choice is motivated by Ref. [127], which obtained a similar value from a universality-driven treatment of the map between 3D Ising model and QCD in the small quark mass limit.

Table 4.1: The two sets of parameter choices we employ in this work. T_C and α_1 follow from the parametrization of the transition line in Eq. 3.30

	μ_{BC}	T_C	α_1	$\alpha_2 - \alpha_1$	w	ρ
I.	420 MeV	138 MeV	4.6°	90°	$0.75, 1, 2, 4$	$0.75, 1.5, 2$
II.	420 MeV	138 MeV	4.6°	330°	$0.75, 1, 2, 4$	$0.75, 1.5, 2$

very important consequences. From our construction of the EOS, in particular the map from Ising to QCD variables, the closer the Ising axes are to being parallel to each other, i.e. small $\alpha_1 - \alpha_2 = -30°$, the stronger a critical behavior we can expect to observe in the fourth cumulant of the net-baryon number. Additionally, the role of the parameter ρ is enhanced, such that it more directly influences the range in chemical potential over which a variation in the thermodynamics occurs.

We start by investigating the behavior of $\chi_4^B(T, \mu_B) = \partial^4(p/T^4)/\partial(\mu_B/T)^4$ on the region close to the critical point $T = 120 - 180\,\text{MeV}$ and $\mu_B = 390 - 450\,\text{MeV}$. χ_4^B is related to the baryon number kurtosis κ discussed above as $\chi_4^B = \kappa\sigma^4$. In Figs. 4.4 and 4.5 the density plots of $\chi_4^B(T, \mu_B)$ in the $(T,\ \mu_B)$ plane are shown for $w = 0.75, 1.5, 2, 4$ and $\rho = 0.75, 1, 2$ in the case of $\alpha_2 - \alpha_1 = 90°$ and $\alpha_2 - \alpha_1 = 330°$, respectively. The yellow and green areas correspond to positive values (the regions where it is the largest are indicated in yellow) of χ_4^B, while the blue ones correspond to negative ones (darker blue in the regions where it is largest in magnitude). The orange curve shows the QCD transition line from Eq. (3.30.) We note that in Figs. 4.4 and 4.5 we only show the contribution to χ_4^B from the critical point, without the baseline non-Ising terms. Since our procedure stops at order $\mathcal{O}(\mu_B^4)$, the total contribution obtained in our approach differs from the critical one by a constant in μ_B, i.e. a function depending on the temperature only. Thus, a similar plot for the

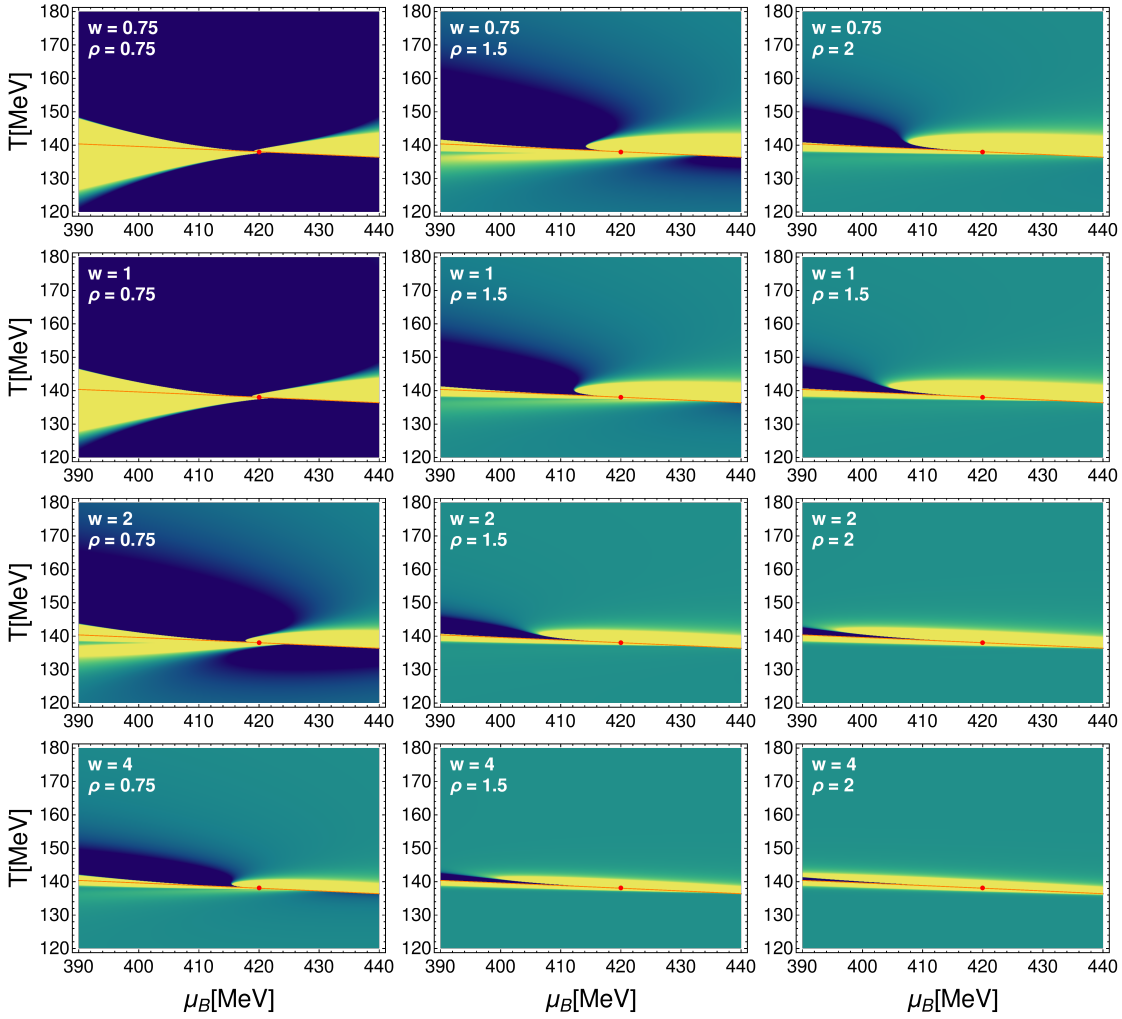

Figure 4.4: Density plots of the critical contribution to $\chi_4^B(T,\mu_B)$ in the (T,μ_B) plane with a critical point located at $(T_C \simeq 138\,\mathrm{MeV}, \mu_{BC} = 420\,\mathrm{MeV})$, and with $\alpha_2 - \alpha_1 = 90°$, for (top to bottom) $w = 0.75, 1.5, 2, 4$ and (left to right) $\rho = 0.75, 1, 2$. The critical point is indicated by a red dot, while the chiral/deconfinement transition line is represented by the solid, orange line. The yellow regions indicate large, positive values, while the dark blue ones indicate large, negative values.

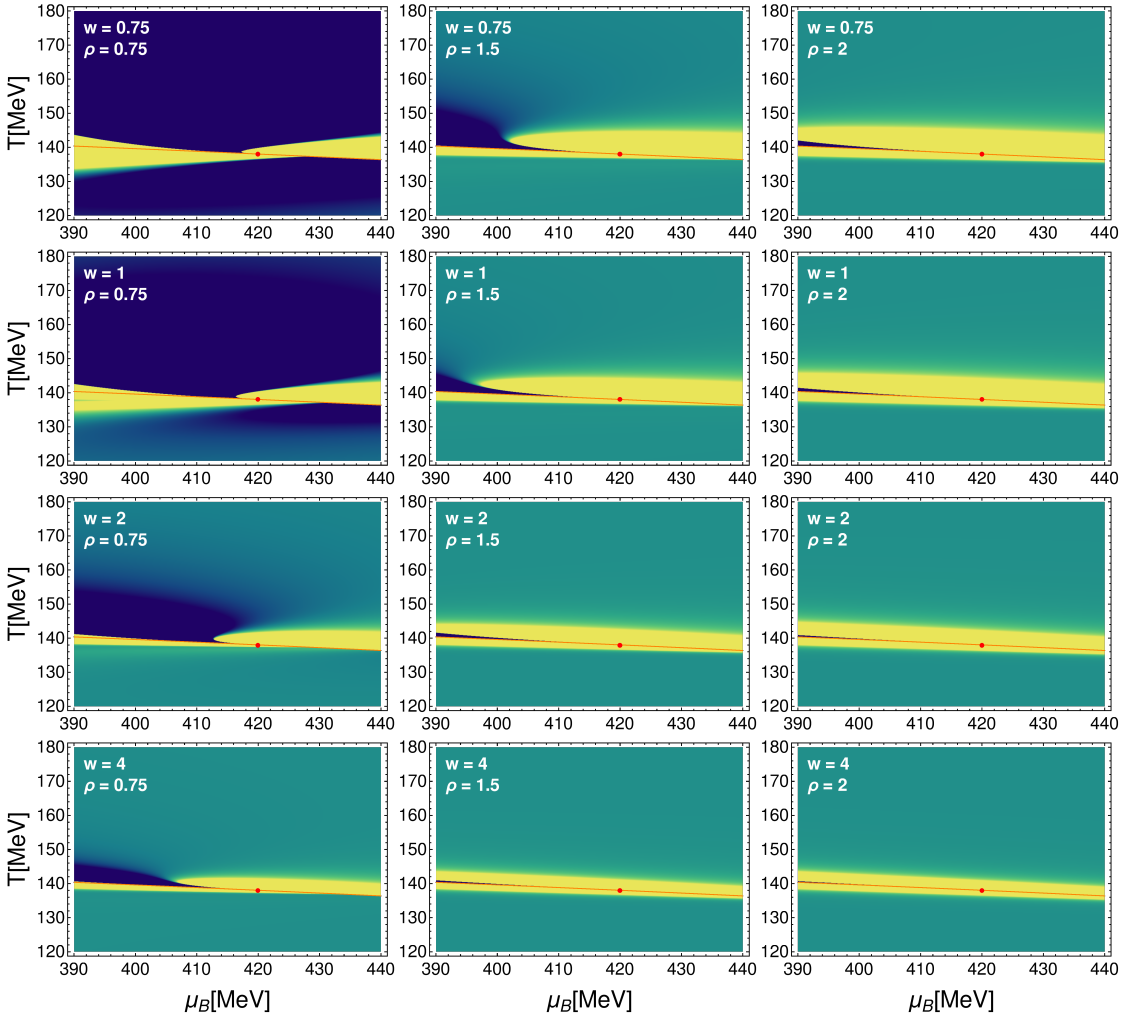

Figure 4.5: Density plots of the critical contribution to $\chi_4^B(T,\mu_B)$ in the (T,μ_B) plane with a critical point located at $(T_C \simeq 138\,\mathrm{MeV}, \mu_{BC} = 420\,\mathrm{MeV})$, and with $\alpha_2 - \alpha_1 = 330°$, for (top to bottom) $w = 0.75, 1.5, 2, 4$ and (left to right) $\rho = 0.75, 1, 2$. The critical point is indicated by a red dot, while the chiral/deconfinement transition line is represented by the solid, orange line. The yellow regions indicate large, positive values, while the dark blue ones indicate large, negative values.

total contribution would show the same features, shifted by a constant.

Although χ_4^B diverges by construction for every choice of parameters, the size of the critical region is still an unknown feature of the theory. Hence, how much the divergence, in both the positive and negative direction, extends in the phase diagram cannot be extracted from universality arguments. Yet, it is critical that we try to determine to what extent it can be detected experimentally. Because the net-proton kurtosis is measured only at the hadron gas phase, if the critical region is small, it is possible that the divergence in the kurtosis would be nullified at the chemical freeze-out.

We see in Figs. 4.4 and 4.5 that, as expected, a smaller value of w leads to a larger critical region for both values of the relative angle $\alpha_2 - \alpha_1$, since $\partial_{\mu_B} \sim 1/w$. We can also see that the main effect of ρ seems to be that of changing the shape of the critical region, resulting in a flattening and twisting of the "lobe-like" structures that are most evident in the case of $w = 0.75, \rho = 0.75$. As discussed previously, the parameter ρ in the Ising-to-QCD map indicates the relative scale between the t (which we called r in Chapter 3) and h directions, so this was also expected. Most importantly, the behavior of this observable is quite the *opposite* of what was originally anticipated in Ref. [126]. The region where the kurtosis turns negative is in fact either at temperatures above the transition line, or at chemical potentials larger than the critical point one.

This demonstrates the importance of accounting for the sub-leading terms that arise from the Ising-to-QCD mapping, as they indeed become relevant outside the immediate vicinity of the critical point. While in the 3D Ising model the leading

divergence comes from a derivative with respect to the magnetic field – see Eq. (4.1) – in QCD we need to obtain the derivative with respect to the baryon chemical potential. Because of the mapping between 3D Ising and QCD, in general these two derivatives are related by:

$$\partial_{\mu_B} \sim A_t\, \partial_t + A_h\, \partial_h \ , \tag{4.2}$$

where A_t and A_h are two quantities which depend on the mapping parameters that are proportional to the cosines of the angles α_1 and α_2. Taking only the leading divergence corresponds to setting $\partial_{\mu_B} \sim \partial_h$, and hence $\partial^4_{\mu_B} \sim \partial^4_h$. The full expression contains many additional terms. Dropping the additional terms is only justified as $A_t \to 0$ and $A_h \to 1$. However, in realistic realizations of the Ising-to-QCD map, one has $A_t \sim 1$, since $\alpha_1 \sim 0$, which alone prevents the additional terms in the derivative from being negligible. Furthermore, in the case $\alpha_2 - \alpha_1 = \pi/2$, we also have $A_h \sim 0$. When $\alpha_2 - \alpha_1 = 330^\circ$ the situation is closer to the expected one. This can be seen in Fig. 4.5, especially for $\rho = 1.5, 2$, where the dark blue (negative) lobe is turned and falls in between the yellow (positive) ones.

Next, we show the behavior of the ratio $\chi^B_4/\chi^B_2 = \kappa\sigma^2$ along parametrized freeze-out lines. This is the observable for which the kurtosis of the net-proton number is used as a proxy. Once again, we consider trajectories which are parallel to the chiral transition line in Eq. (3.30):

$$T(\mu_B) = T_0 + \kappa_2\, T_0 \left(\frac{\mu_B}{T_0}\right)^2 - \Delta T \ , \tag{4.3}$$

where ΔT indicates the shift in temperature from the transition line.

First, we consider $\alpha_2 - \alpha_1 = 90^\circ$, with $(w, \rho) = (0.75, 1.5), (1, 2)$ and $(4, 0.75)$. In

Fig. 4.6 the ratio $\chi_4^B(T,\mu_B)/\chi_2^B(T,\mu_B)$ is shown as a function of μ_B along the lines in Eq. (4.3) with $\Delta T = 4 - 14\,\mathrm{MeV}$ (in intervals of $1\,\mathrm{MeV}$).

Under this set of parameters, we observe a slow decrease with increasing chemical potential – decreasing collision energy – then a rapid increase. This closely matches BES-I results from the STAR collaboration, though the error bars from experimental data are sizeable.

As discussed earlier, the presence of a clear, pronounced peak in the measurements at low collision energies would be an unambiguous signal of the presence of the critical point. However, it is not clear whether the initial decrease can also be attributed to critical behavior. Since our EOS allows us to compute the Taylor expansion for the pressure using only the non-Ising coefficients, we considered the case where there is no contribution from the Ising critical point. The results are shown in Fig. 4.7, where we performed the calculations using the same lines as in Fig. 4.6, but with no critical point. The decrease, or dip, is clearly observed in the case without the critical point, which leads us to the conclusion that it is built into the underlying non-critical behavior.

To further make the case, in Fig. 4.8, we show the same curves that included a critical contribution in Fig. 4.6, but this time subtracting the underlying behavior shown in Fig. 4.7. We see that the decrease is completely erased and that the only signal associated with the presence of the critical point is the sharp increase.

Even when different parameters are chosen, the overall features and behaviors as (w,ρ) is changed remain the same. In Figs. 4.9 and 4.11 we show the plots

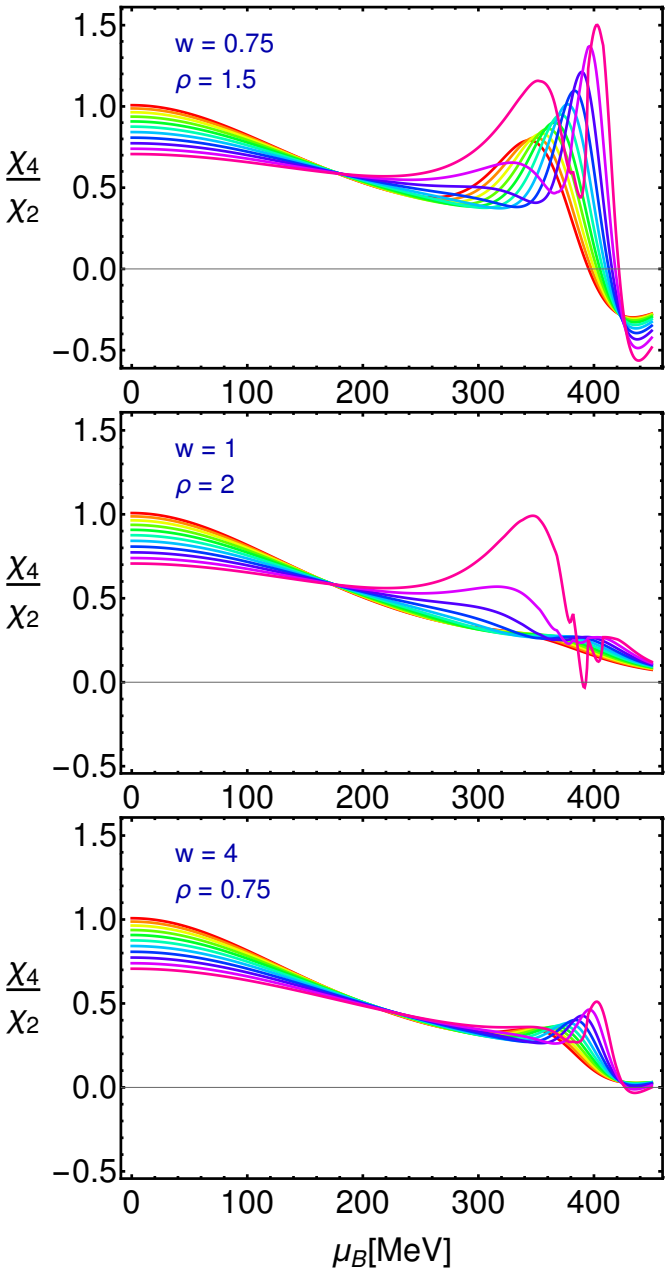

Figure 4.6: Chemical potential dependence of χ_4^B/χ_2^B along lines parallel to the chiral/deconfinement transition one (as defined in Eq. (4.3)), with $\Delta T = 4-14\,\mathrm{MeV}$, for $1\,\mathrm{MeV}$ intervals. The critical point is located at $(T_C \simeq 138\,\mathrm{MeV}, \mu_{BC} = 420\,\mathrm{MeV})$, and $\alpha_2 - \alpha_1 = 90°$. From left to right we have $(w, \rho) = (0.75, 1.5), (1, 2)$ and $(4, 0.75)$.

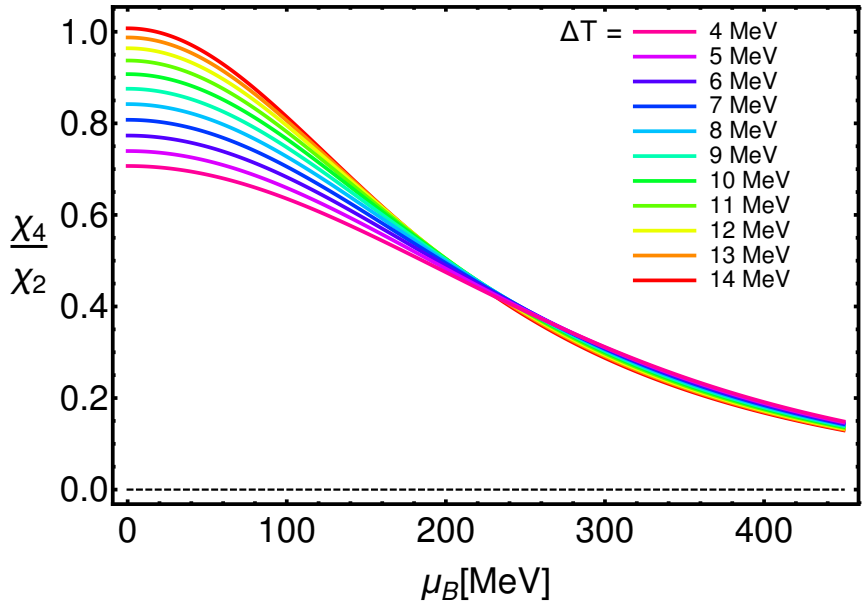

Figure 4.7: Chemical potential dependence of χ_4^B/χ_2^B along the same lines as in Fig. 4.6, in the absence of a critical point. The color coding defined in this Figure is the same as in Fig. 4.6 and will be maintained in all remaining figures shown in this chapter.

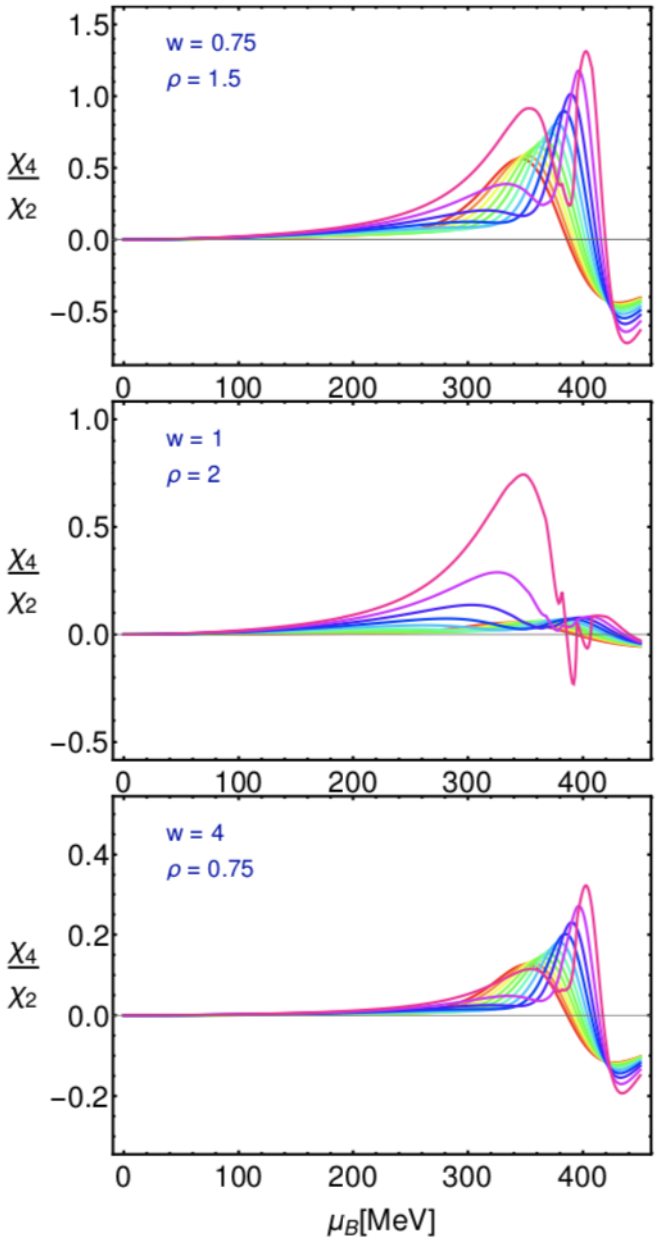

Figure 4.8: Chemical potential dependence of χ_4^B/χ_2^B along lines parallel to the chiral/deconfinement transition one (as defined in Eq. (4.3)), with $\Delta T = 4-14\,\mathrm{MeV}$, for 1 MeV intervals, after subtracting the underlying behavior. The critical point is located at $(T_C \simeq 138\,\mathrm{MeV}, \mu_{BC} = 420\,\mathrm{MeV})$, and $\alpha_2 - \alpha_1 = 90°$. From left to right we have $(w, \rho) = (0.75, 1.5), (1, 2)$ and $(4, 0.75)$.

corresponding to $\alpha_2 - \alpha_1 = 90^\circ$ and $\alpha_2 - \alpha_1 = 330^\circ$, respectively. In Figs. 4.10 and 4.12 we show the same plots, but subtracting the underlying behavior. The plots indicate that when w is increased, while other parameters are kept constant, the effect of the critical point is reduced. In addition, a smaller angle difference enhances such effects.

4.1.4 Implications for BES-II and Future Experiments

What this analysis shows is that clearly we cannot infer the presence of a critical point based solely on the experimental observation of a decrease in $\kappa\sigma^2$ for the net-proton count as function of collision energy. There is evidence that the small dip can be accounted for even when no critical point is present in the system. However, the peak has thus far been a consistent indicator of criticality, and once smaller error bars are obtained at lower collision energies, it would represent a clear signal in favor of the existence of the critical point.

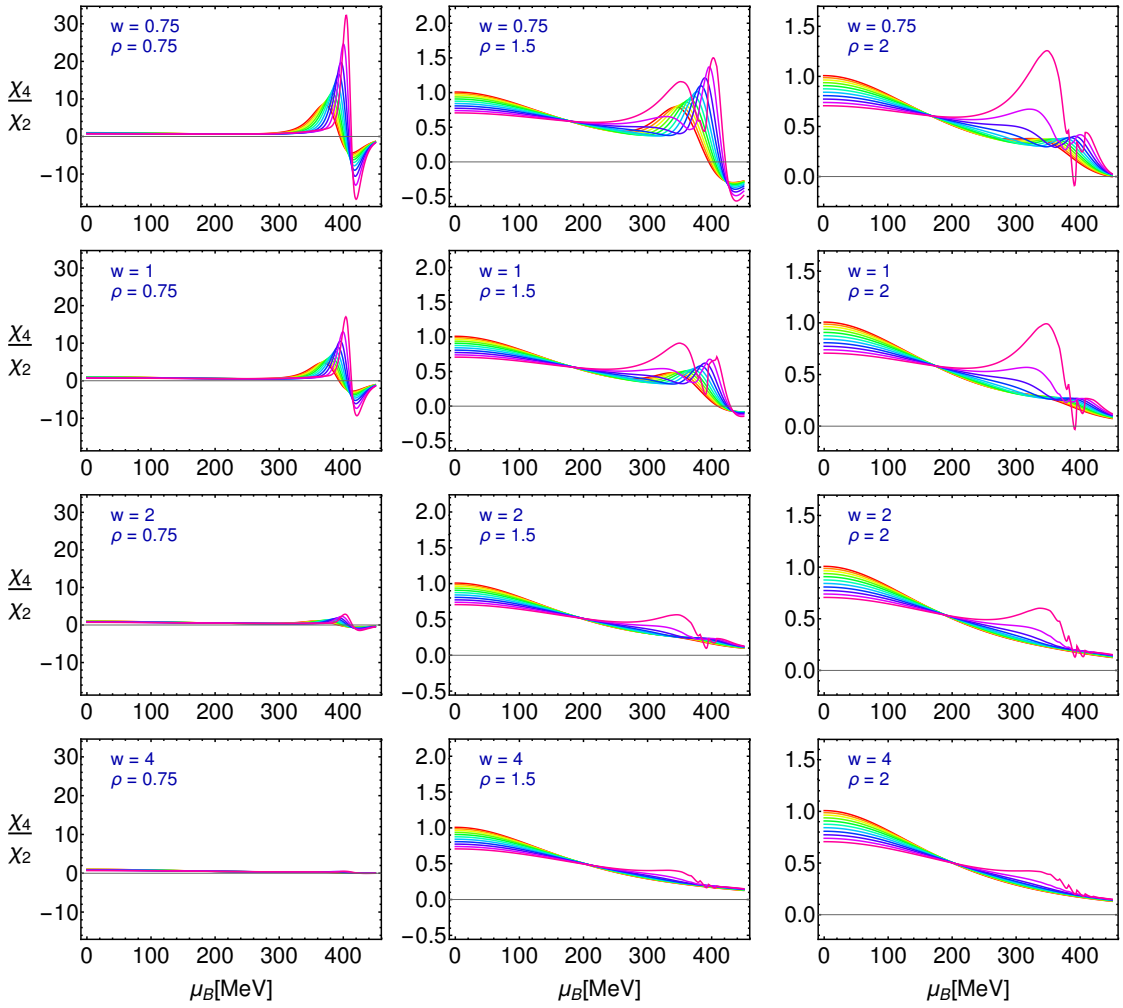

Figure 4.9: Chemical potential dependence of $\chi_4^B(T,\mu_B)/\chi_2^B(T,\mu_B)$ along lines parallel to the chiral/deconfinement transition one (as defined in Eq. (4.3)), with $\Delta T = 4 - 14\,\mathrm{MeV}$, for $1\,\mathrm{MeV}$ intervals. The critical point is located at ($T_C \simeq 138\,\mathrm{MeV}, \mu_{BC} = 420\,\mathrm{MeV}$), and $\alpha_2 - \alpha_1 = 90°$; from top to bottom $w = 0.75, 1.5, 2, 4$, and from top to bottom $\rho = 0.75, 1, 2$.

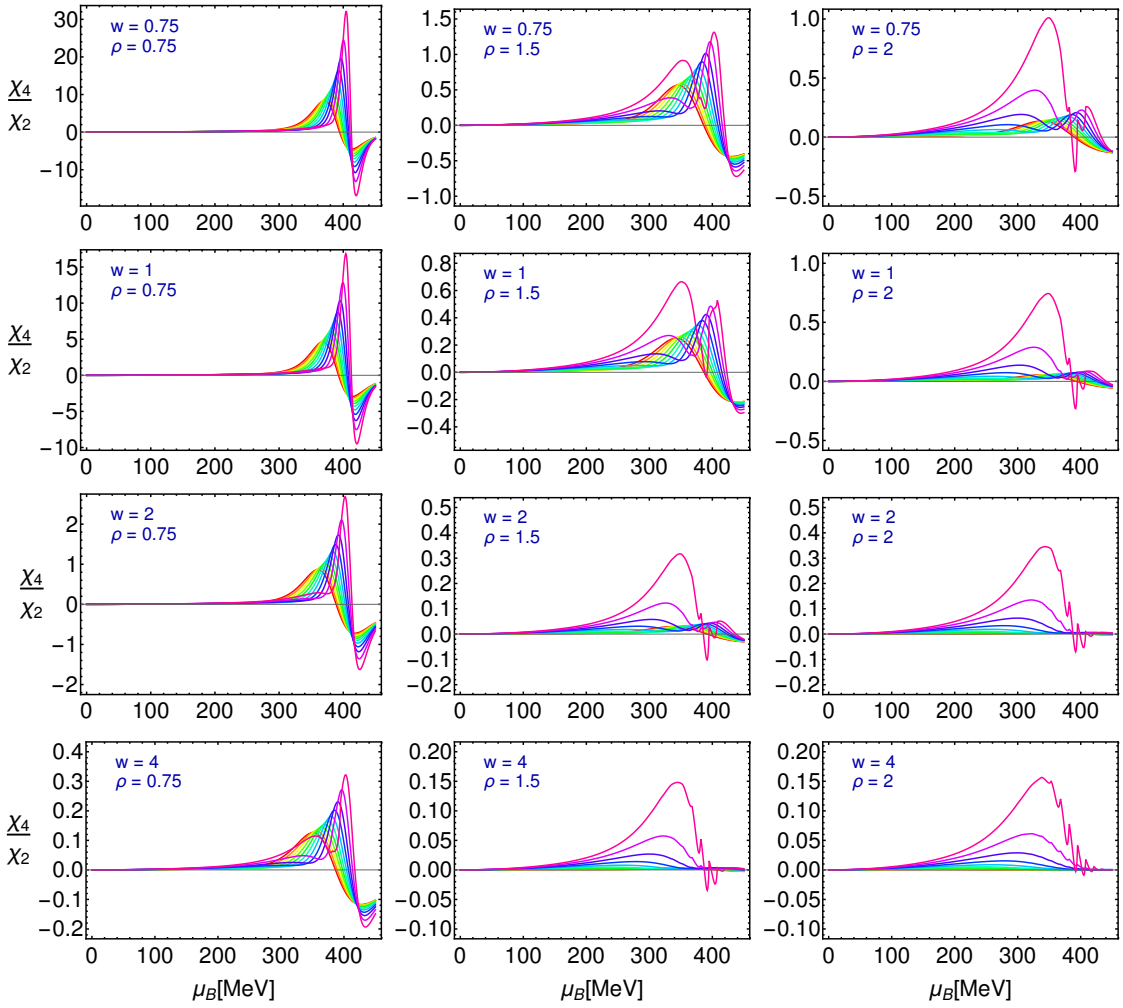

Figure 4.10: Same curves as in Fig. 4.9, with the underlying behavior subtracted.

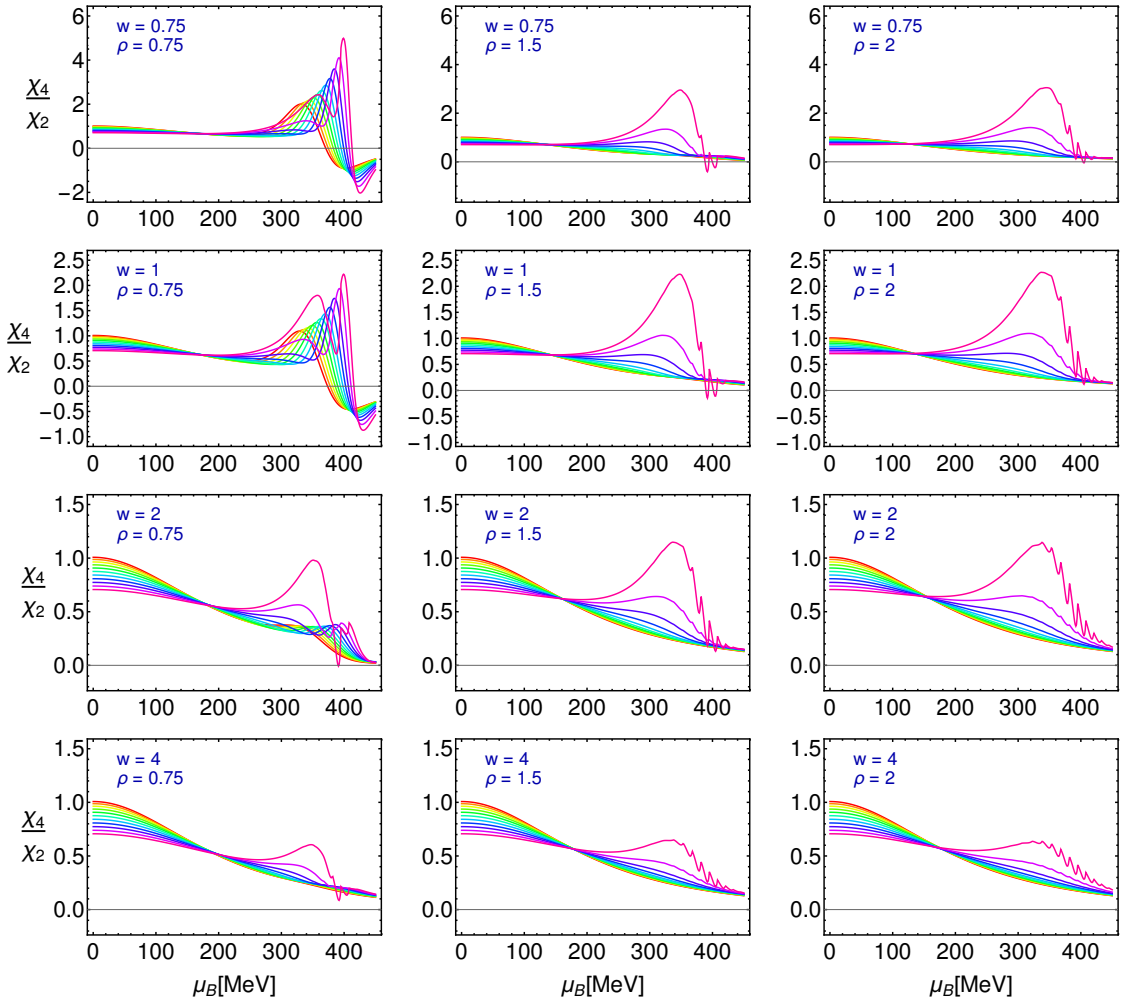

Figure 4.11: Chemical potential dependence of $\chi_4^B(T,\mu_B)/\chi_2^B(T,\mu_B)$ along lines parallel to the chiral/deconfinement transition one (as defined in Eq. (4.3)), with $\Delta T = 4 - 14\,\mathrm{MeV}$, for $1\,\mathrm{MeV}$ intervals. The critical point is located at $(T_C \simeq 138\,\mathrm{MeV}, \mu_{BC} = 420\,\mathrm{MeV})$, and $\alpha_2 - \alpha_1 = 330°$; from top to bottom $w = 0.75, 1.5, 2, 4$, and from top to bottom $\rho = 0.75, 1, 2$.

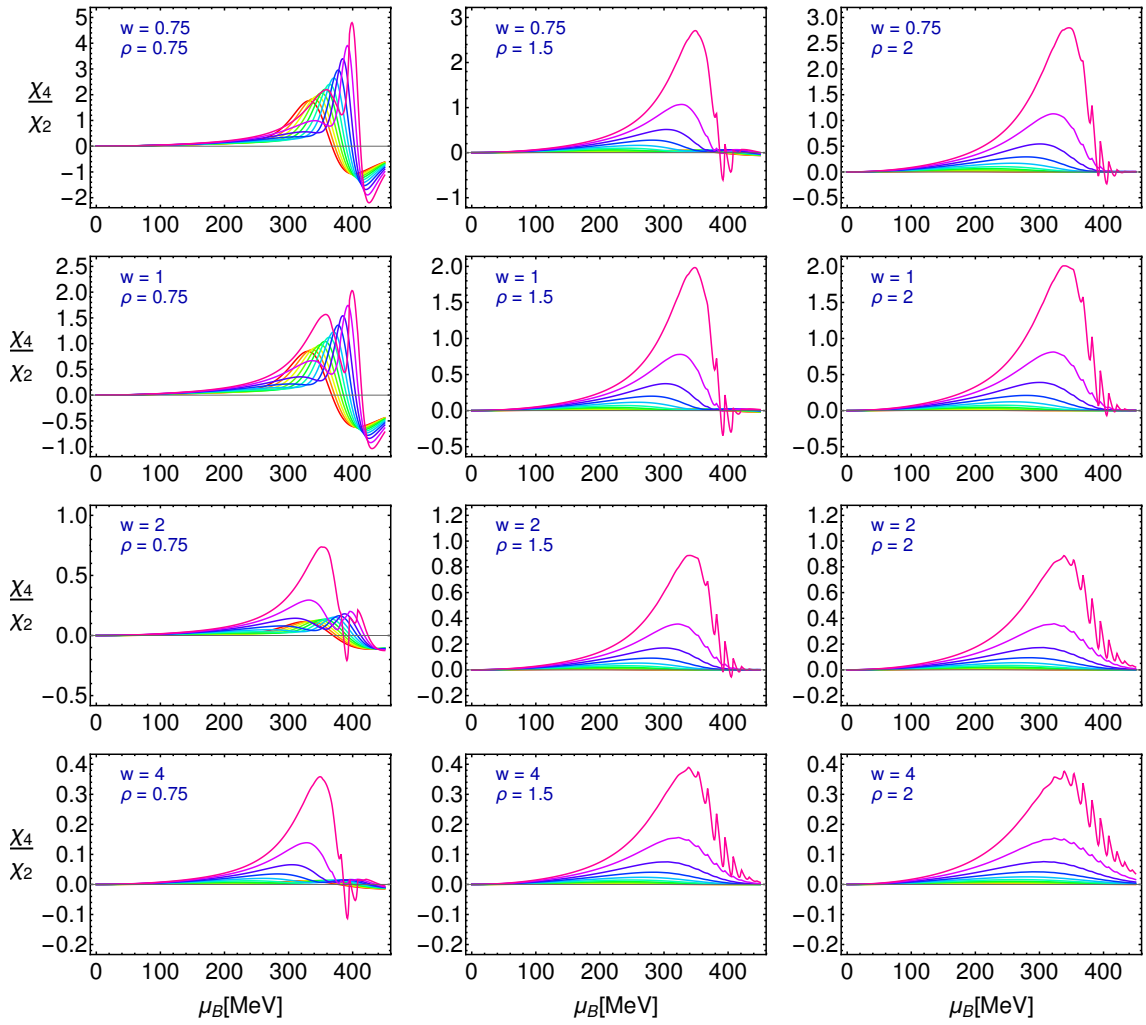

Figure 4.12: Same curves as in Fig. 4.11, with the underlying behavior subtracted.

4.2 Imposing Thermodynamic Stability Using Neural Networks

Recall from Chapter 3, that while some constraints can be placed on the choice of parameters for the Ising-to-QCD mapping in Eqs. (3.13) and (3.14),

$$\frac{T - T_C}{T_C} = w(r\rho \sin\alpha_1 + h \sin\alpha_2),$$
$$\frac{\mu_B - \mu_{BC}}{T_C} = w(-r\rho \cos\alpha_1 - h \cos\alpha_2),$$

there are no arguments that can be made to constrain the scaling parameters w and ρ. An alternative to the lack of lattice or universality arguments on this front is to require the system to be thermodynamically stable. That is not to say that thermodynamic stability is not a requirement *in general*, but by making use of it and performing a systematic scan of the possible values for (w, ρ), while keeping other parameters fixed, we can learn about what values are allowed and which ones are pathological.

In order to test this idea, we fixed the location of the critical point at $\mu_{BC} = 350\,\text{MeV}$ and $T_C = 143\,\text{MeV}$, as well as the angles, $\alpha_1 = 3.85°$ with $\alpha_2 - \alpha_1 = 90°$, and changed the value of (w, ρ) within the interval $(0, 2) \times (0, 4)$ in 0.25 increments for w and 0.5 increments for ρ. The results are shown in Fig 4.13, which indicates that values of (w, ρ) that correspond to larger critical region – i.e. small w – are forbidden and there is an apparent dependence on ρ, so both parameters are relevant for the thermodynamic stability of the EOS.

Though insightful, the process of individually calculating the EOS along with

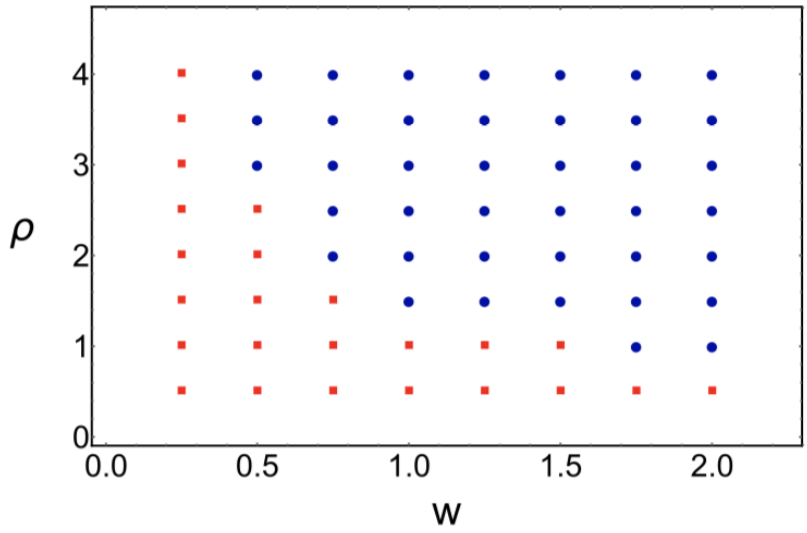

Figure 4.13: Plane of (w, ρ) values. The red squares correspond to pathological parameter choices and the blue circles to allowed values.

every thermodynamic observable and then checking every point for every choice of parameter for pathological behavior is time-consuming and computationally inefficient. An alternative to all this computational labor is to use a machine learning classification algorithm – namely, an Artificial Neural Network (ANN) – that can identify what makes a parameter choice "good" or "bad" and then classify new parameter choices based on whether "good" or "bad" features are detected in the EOS. Another advantage of this method is that, since all thermodynamic observables are derivatives of the pressure, we expect that these features can be detected in the pressure, which would eliminate the need to compute and check the derivatives.

4.2.1 Strategy and Methods

Under the premise that we can identify pathological patterns in the pressure and classify a specific choice of parameters as pathological/acceptable without calculating numerical derivatives, we adopted the following strategy:

i. First, we produce a small subset of equations of state within the (w, ρ) range of interest.

ii. For this small subset, we check every point for every thermodynamic quantity for stability and causality.

iii. Then we tag each set of parameters as "acceptable" or "pathological," and use the *pressure only* as training data for the ANN.

iv. Once the network has been trained using the small subset of parameters, generate an EOS (pressure only) for each value of (w, ρ) within the range of interest.

v. Run the set of pressure data through the ANN, which will classify each choice of parameter as "acceptable" or "pathological," with a prediction confidence between 50-100%.

Neural networks were designed to mimic information flow in the human brain and its billions of neurons that communicate with each other via electric signals. In an Artificial Neural Network, each neuron receives signals from the previous layer – the first one being the input layer – and if a certain threshold is exceeded, that neuron

is activated, and passes on information onto the next layer. A simple mathematical model for an artificial neuron is given by

$$y = f\left(\sum_{i=1}^{n} w_i x_i\right) = f(u). \tag{4.4}$$

Here, the output y of the neuron is the value of its activation function, which have as input a weighted sum of signals $x_i, \ldots, x_n$ received by n other neurons.

An artificial neural network will have layers of connected neurons, which interact with each other via mathematical functions defined between each layer. Most ANN's are comprised of an input layer, an output layer, and hidden layers in between. In the case of classification networks, each hidden layer can contain an arbitrary number of neurons, or nodes, but the input layer must have as many nodes as input signals while the number of nodes in the output layer must match the number of classes. The connection between two nodes is associated with a weight variable w_i.

In general, the goal of a classification NN is to divide the input received into two or more classes of outputs. In order to do that, we must produce a model that systematically assigns inputs into one of these classes. In our case, the two classes are "acceptable" and "pathological," which determine if a set of parameters complies with thermodynamic stability and causality.

The first step in creating an ANN is to pre-process the data, so that only the essential information goes through the network. If we take the (w, ρ) plot shown in Fig. 4.13 in 0.1 increments in both variables, we have a total of 648 combinations of parameters. For each of these parameter choices, the pressure contains data ranging

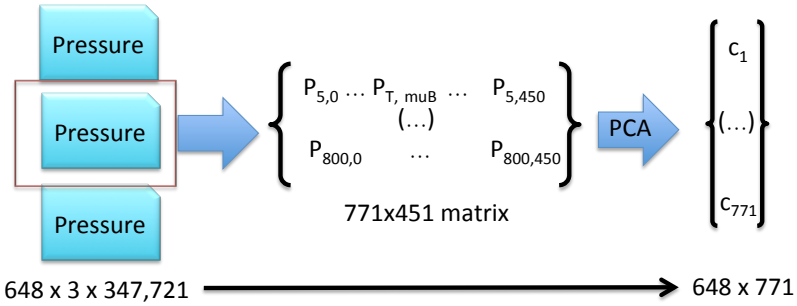

Figure 4.14: Schematics of the data processing.

from $30-800$ MeV in T and $0-450$ MeV in μ_B, which is a total of 347,721 individual points[2]. Feeding 347,721 points to a neural network is just as inefficient as going through the process of checking each thermodynamic observable. Therefore, for each set of parameters, we take the pressure, map it onto a 771×451 matrix, and perform a principle component analysis. We then take the first vector in the baryon chemical potential basis, which generally accounts for $\sim 98\%$ of the variation in the pressure, and use that as the input for the network instead of the full pressure. Using this procedure the input data is reduced from 10GB (648 full pressure files) to about 33KB (648 vectors of dimension 771). The full process is illustrated in Fig. 4.14.

In terms of the design of the NN, the number of hidden layers has to be optimized on an empirical basis. The optimization is done based on the minimization of the loss, which is a function that measures how well the network accomplished its task. The final network design is shown in Fig. 4.15. The input layer has 771 nodes, each corresponding to an entry in the principle component. The input layer is followed by 2 layers of 200 nodes and an output layer containing the two nodes corresponding to

[2]The output from the EOS is given in the form: (μ_B, T, P), so there are actually $3 \times 347,721$ values in each file.

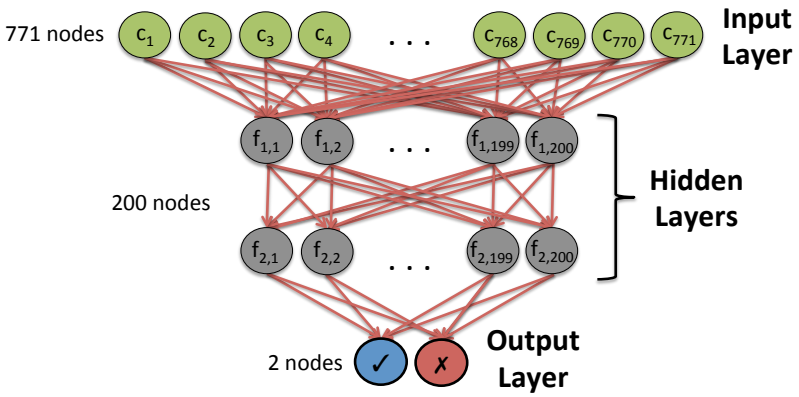

Figure 4.15: Visual representation of the ANN design implemented in the classification of EOS as thermodynamically acceptable or pathological.

pathological and acceptable parameter choices. In our design, each neuron receives input from all preceding neurons but no feedback from the layers ahead of it, making it a fully-connected Feed-Forward Neural Network (FFNN).

The weights for each neuron must be adjusted using a training data set, for which the desired outcome must be known. In our case, the points in Fig. 4.13 were used, since we had already confirmed whether those parameter sets were acceptable or pathological choices.

4.2.2 Results

It is important to note that analysis cannot provide any information regarding why a certain set of parameters is pathological, it can only identify choices that result in either the negativity of thermodynamic quantities or the violation of causality, as determined by pathological features identified by the network in the training data.

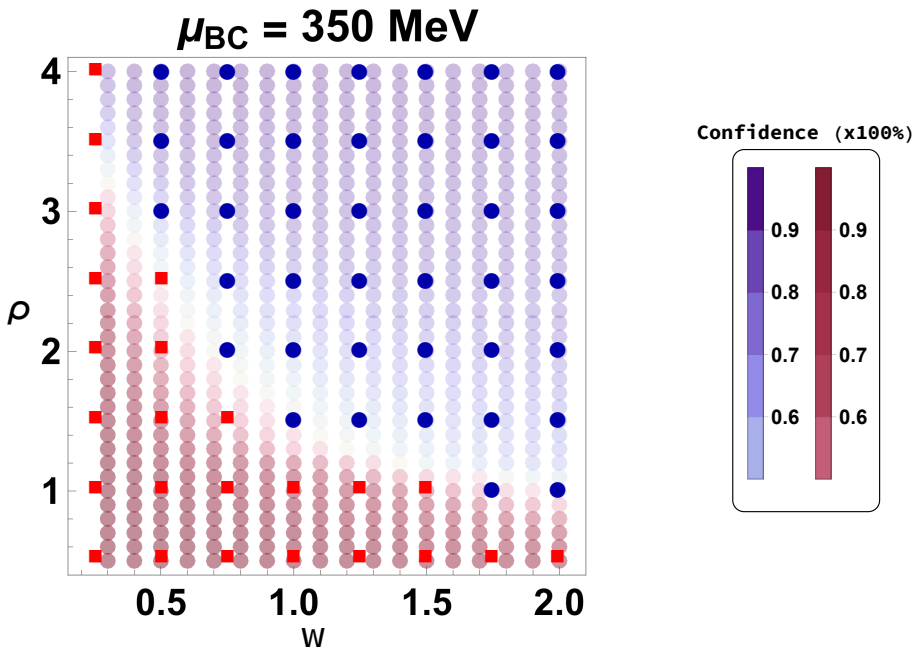

Figure 4.16: Front plane: values of (w, ρ) where red squares correspond to pathological parameter choices and blue circles to allowed values. Background: A finer grid of values in the same (w, ρ) plane classified by the FFNN as pathological (red) or acceptable (blue), where the intensity of either color corresponds the confidence level of the classification as shown in the legend on the right. The other parameters were kept fixed at $\mu_{BC} = 350\,\text{MeV}$, $T_C = 143\,\text{MeV}$, $\alpha_1 = 3.85°$, and $\alpha_2 - \alpha_1 = 90°$.

The finer grid obtained using the FFNN is shown in Fig 4.16 in the background with the same training data from Fig. 4.13 overlaid on top. How confident the network is on the classification is determined by the activation function assigned to the output layer. In our case, the hyperbolic function was used:

$$f(x) = \tanh x. \tag{4.5}$$

The threshold value is 0.5 for the "acceptable" neuron to be activated and -0.5 for the "pathological" neuron to be activated. The plot in Fig 4.16 only shows parameter choices as "acceptable" (blue) or "pathological" (red) if the output value is above ± 0.60, because we consider values between $0.5 - 0.6$ inconclusive. Those points – which are concentrated along the transition between acceptable and pathological choices – are shown in Fig 4.16 in white.

The NN method is a great indicator of the general layout of the acceptable and forbidden regions. However, for points that fall close to the boundary between the two regions, this network design does not give conclusive results. Therefore, it is not a reliable tool to determine whether a *specific* choice of parameters is good or bad. This method should be used as a computationally efficient alternative to determine the *general location* of acceptable and forbidden regions in the context of large parameter scans.

Chapter 5

Conclusions and Future Work

This thesis presented a procedure to construct a family of model equations of state for QCD, each of which features a critical point in the 3D Ising model universality class. An explicit expression for the critical contribution to QCD thermodynamic quantities is obtained via a parametrized change of variables. This EOS can be used in conjunction with hydrodynamic simulations of the fireball created in heavy-ion collisions at energies that are relevant to the ongoing BES-II program. In addition, the EOS can be coupled to hydrodynamic simulations for a Bayesian model-to-data analysis using data from BES-I and, in the future, BES-II. Eventually, we hope to include the other two conserved charges (strangeness and electric charge) in our equation of state, which are just as important in the dynamics of heavy-ion collisions.

We also took advantage of the EOS to study the higher order susceptibilities of the baryon number in QCD in the presence of a critical point in the 3D Ising model universality class. We found that sub-leading terms that arise from the Ising-to-QCD

map contribute significantly to the profile of the baryon number susceptibilities, contradictory to what was expected based on previous works in the field. We established that the decrease in the observable χ_4^B/χ_2^B, which is currently considered a possible critical signature, can be attributed to other factors. We propose that experimental efforts should instead focus on the rapid increase expected at the lower end of BES-II collision energies, which is a consistent feature of χ_4^B/χ_2^B around the critical point.

Lastly, we proposed the use of a Feed-Forward Neural Network to study the structure of the phase space of the EOS in terms of thermodynamic stability and causality principles. The procedure we developed is a computationally efficient way to quickly rule out EOS parameters that violate thermodynamic stability and causality, thus constraining the possible choices of parameters. We illustrate this idea by varying the size and shape of the critical region, while keeping other parameters constant, and we find that a large critical region is generally disfavored. In the future, we hope to produce more training data, and explore the role of other parameters in the thermodynamic stability of the EOS.

Bibliography

[1] Chi Yang, STAR Collaboration, et al. The star beam energy scan phase ii physics and upgrades. *Nuclear Physics A*, 967:800–803, 2017.

[2] Arno A Penzias and Robert Woodrow Wilson. A measurement of excess antenna temperature at 4080 mc/s. *The Astrophysical Journal*, 142:419–421, 1965.

[3] AD Sakharov. Maximum temperature of thermal radiation. *JETP Lett*, 3:288–289, 1966.

[4] Rolf Hagedorn. Statistical thermodynamics of strong interactions at high energies. *Nuovo Cimento, Suppl.*, 3(CERN-TH-520):147–186, 1965.

[5] Johann Rafelski. *Melting Hadrons, Boiling Quarks-From Hagedorn Temperature to Ultra-Relativistic Heavy-Ion Collisions at CERN: With a Tribute to Rolf Hagedorn*. Springer, 2015.

[6] Murray Gell-Mann. A schematic model of baryons and mesons. In *Murray Gell-Mann: Selected Papers*, pages 151–152. World Scientific, 2010.

[7] G. Zweig. An su(3) model for strong interaction symmetry and its breaking. version 1. (CERN-TH-401), 1964.

[8] Ya B Zeldovich and RA Sunyaev. The interaction of matter and radiation in a hot-model universe. *Astrophysics and Space Science*, 4(3):301–316, 1969.

[9] David J Gross and Frank Wilczek. Ultraviolet behavior of non-abelian gauge theories. *Physical Review Letters*, 30(26):1343, 1973.

[10] H David Politzer. Reliable perturbative results for strong interactions? *Physical Review Letters*, 30(26):1346, 1973.

[11] John C Collins and Malcolm J Perry. Superdense matter: neutrons or asymptotically free quarks? *Physical Review Letters*, 34(21):1353, 1975.

[12] Nicola Cabibbo and Giorgio Parisi. Exponential hadronic spectrum and quark liberation. *Physics Letters B*, 59(1):67–69, 1975.

[13] Taizo Muta. *Foundations of quantum chromodynamics: an introduction to perturbative methods in gauge theories*, volume 5. World Scientific Publishing Company, 1987.

[14] John B Kogut and Mikhail A Stephanov. *The phases of quantum chromodynamics: from confinement to extreme environments*, volume 21. Cambridge University Press, 2003.

[15] Wolfgang KH Panofsky and Melba Phillips. *Classical electricity and magnetism*. Courier Corporation, 2005.

[16] M. Tanabashi et al. (Particle Data Group). Particle data group review. *Physical Review D*, 98.

[17] 57 L Montanet, K Gieselmann, RM Barnett, DE Groom, TG Trippe, CG Wohl, B Armstrong, GS Wagman, H Murayama, J Stone, et al. Review of particle properties. *Physical Review D*, 50(3):1173, 1994.

[18] J Steinberger. On the use of subtraction fields and the lifetimes of some types of meson decay. *Physical Review*, 76(8):1180, 1949.

[19] Jerry Gaston. Secretiveness and competition for priority of discovery in physics. *Minerva*, pages 472–492, 1971.

[20] R Keith Ellis, W James Stirling, and Bryan R Webber. *QCD and collider physics*. Cambridge university press, 2003.

[21] Claude Amsler and CG Wohl. Quark model. *The European Physical Journal. C, Particles and Fields.*, 15(1-4):117–120, 2000.

[22] Jeremy Bernstein. Elementary particles and their currents. 1968.

[23] AP Contogouris and J Kripfganz. Scale violations and the quark-gluon correction to the drell-yan formalism. *Physical Review D*, 19(7):2207, 1979.

[24] Kurt Symanzik. Small distance behaviour in field theory and power counting. *Communications in Mathematical Physics*, 18(3):227–246, 1970.

[25] Siegfried Bethke. Experimental tests of asymptotic freedom. *Progress in Particle and Nuclear Physics*, 58(2):351–386, 2007.

[26] Guido Altarelli. Experimental tests of perturbative qcd. *Annual Review of Nuclear and Particle Science*, 39(1):357–406, 1989.

[27] Betty Abelev, J Adam, D Adamová, AM Adare, MM Aggarwal, G Aglieri Rinella, AG Agocs, A Agostinelli, S Aguilar Salazar, Z Ahammed, et al. Multistrange baryon production in pp collisions at s= 7 tev with alice. *Physics Letters B*, 712(4-5):309–318, 2012.

[28] E.V. Shuryak. Theory of hadron plasma. *Sov. Phys. - JETP (Engl. Transl.); (United States).*

[29] Reinhard Stock. Relativistic nucleus-nucleus collisions and the qcd phase diagram. 756(1):1–9, 2005.

[30] H Behrens and J Jänecke. Landolt-börnstein-group i, elementary particles, nuclei and atoms vol. 4. 1969.

[31] HR Schmidt and Jürgen Schükraft. The physics of ultra-relativistic heavy-ion collisions. *J. Phys. G*, 19(CERN-PPE-92-042):1705–1796, 1992.

[32] Ulrich Heinz and Maurice Jacob. Evidence for a new state of matter: An assessment of the results from the cern lead beam programme, 2000. *arXiv preprint nucl-th/0002042*.

[33] Relativistic heavy ion physics. `http://wl33.web.rice.edu/research.html`.

[34] I.G. Bearden et al. Collective expansion in high-energy heavy ion collisions. *Physical Review Letters*.

[35] H. Appelshauser et al.. Hadronic expansion dynamics in central pb+pb collisions at 158 gev per nucleon. *European Physical Journal C*.

[36] M.M. Aggarwal et al. Freeze-out parameters in central 158 a gev ^{208}pb+^{208}pb collisions. *Physical Review Letters*.

[37] E. Andersen et al. Strangeness enhancement at mid-rapidity in pb-pb collisions at 158 a gev/c. *Physics Letters B*.

[38] F. Antinori et al. Production of strange and multistrange hadrons in nucleus-nucleus collisions at the sps. *Nuclear Physics A*.

[39] Strange meson enhancement in pb-pb collisions, author=I.G. Bearden et al., journal=Physics Letters B volume =471 pages6-12 year=1999.

[40] Anomalous j/ψ suppression in pb-pb interactions at 158 gev/c per nucleon, author=M.C. Abreu et al., journal=Physics Letters B volume =410 pages337-343 year=1997.

[41] Observation of a threshold effect in the anomalous j/ψ suppression, author=M.C. Abreu et al., journal=Physics Letters B volume =450 pages356-466 year=1999.

[42] Federico Antinori, WA97 Collaboration, et al. Strangeness enhancement at midrapidity in pb–pb collisions at 158 a gev/c: A comparison with venus and rqmd models. *The European Physical Journal C-Particles and Fields*, 11(1):79–88, 1999.

[43] Roman Pasechnik and Michal Šumbera. Phenomenological review on quark–gluon plasma: Concepts vs. observations. *Universe*, 3(1):7, 2017.

[44] I Arsene, IG Bearden, D Beavis, C Besliu, B Budick, H Bøggild, C Chasman, CH Christensen, P Christiansen, J Cibor, et al. Quark–gluon plasma and color glass condensate at rhic? the perspective from the brahms experiment. *Nuclear Physics A*, 757(1-2):1–27, 2005.

[45] BB Back, MD Baker, M Ballintijn, DS Barton, B Becker, RR Betts, AA Bickley, R Bindel, A Budzanowski, W Busza, et al. The phobos perspective on discoveries at rhic. *Nuclear Physics A*, 757(1-2):28–101, 2005.

[46] John Adams, MM Aggarwal, Z Ahammed, J Amonett, BD Anderson, D Arkhipkin, GS Averichev, SK Badyal, Y Bai, J Balewski, et al. Experimental and theoretical challenges in the search for the quark–gluon plasma: The star collaboration's critical assessment of the evidence from rhic collisions. *Nuclear Physics A*, 757(1-2):102–183, 2005.

[47] K Adcox, Phenix Collaboration, et al. Formation of dense partonic matter in relativistic nucleus-nucleus collisions at rhic: Experimental evaluation by the phenix collaboration. *arXiv preprint nucl-ex/0410003*, 2004.

[48] John Adams, C Adler, MM Aggarwal, Z Ahammed, J Amonett, BD Anderson, M Anderson, D Arkhipkin, GS Averichev, SK Badyal, et al. Particle-type dependence of azimuthal anisotropy and nuclear modification of particle production in a u+ a u collisions at s n n= 200 g e v. *Physical review letters*, 92(5):052302, 2004.

[49] Pasi Huovinen, Peter F Kolb, Ulrich Heinz, PV Ruuskanen, and Sergei A Voloshin. Radial and elliptic flow at rhic: Further predictions. *Physics Letters B*, 503(1-2):58–64, 2001.

[50] Tetsufumi Hirano, Pasi Huovinen, and Yasushi Nara. Elliptic flow in u+ u collisions at s nn= 200 gev and in pb+ pb collisions at s nn= 2.76 tev: Prediction from a hybrid approach. *Physical Review C*, 83(2):021902, 2011.

[51] Peter F Kolb and Ulrich Heinz. Hydrodynamic description of ultrarelativistic heavy-ion collisions. In *Quark–Gluon Plasma 3*, pages 634–714. World Scientific, 2004.

[52] C Adler, Z Ahammed, C Allgower, J Amonett, BD Anderson, M Anderson, GS Averichev, J Balewski, O Barannikova, LS Barnby, et al. Identified particle elliptic flow in a u+ a u collisions at s nn= 130 gev. *Physical Review Letters*, 87(18):182301, 2001.

[53] Mikhail A Stephanov. Qcd phase diagram and the critical point. *International Journal of Modern Physics A*, 20(19):4387–4392, 2005.

[54] BMM Allbrooke, L Asquith, A Cerri, CA Chavez Barajas, I Santoyo Castillo, K Suruliz, MR Sutton, I Vivarelli, et al ATLAS Collaboration, et al. Measurement of the production and lepton charge asymmetry of w bosons in pb+ pb collisions at snn= 2.76 tev with the atlas detector. *The European Physical Journal C-Particles and Fields*, 75(23), 2015.

[55] Frank R Brown, Frank P Butler, Hong Chen, Norman H Christ, Zhihua Dong, Wendy Schaffer, Leo I Unger, and Alessandro Vaccarino. On the existence of a phase transition for qcd with three light quarks. *Physical Review Letters*, 65(20):2491, 1990.

[56] Y Aoki, G Endrődi, Z Fodor, SD Katz, and KK Szabo. The order of the quantum chromodynamics transition predicted by the standard model of particle physics. *Nature*, 443(7112):675–678, 2006.

[57] Asakawa Masayuki and Yazaki Koichi. Chiral restoration at finite density and temperature. *Nuclear Physics A*, 504(4):668–684, 1989.

[58] A Barducci, R Casalbuoni, S De Curtis, Raoul Gatto, and Giulio Pettini. Chiral phase transitions in qcd for finite temperature and density. *Physical Review D*, 41(5):1610, 1990.

[59] A Barducci, R Casalbuoni, S De Curtis, Raoul Gatto, and Giulio Pettini. Chiral-symmetry breaking in qcd at finite temperature and density. *Physics Letters B*, 231(4):463–470, 1989.

[60] A Barducci, Roberto Casalbuoni, Giulio Pettini, and Raoul Gatto. Chiral phases of qcd at finite density and temperature. *Physical Review D*, 49(1):426, 1994.

[61] Jurgen Berges and Krishna Rajagopal. Color superconductivity and chiral symmetry restoration at nonzero baryon density and temperature. *arXiv preprint hep-ph/9804233*, 1998.

[62] MA Halasz, AD Jackson, RE Shrock, Misha A Stephanov, and JJM Verbaarschot. Phase diagram of qcd. *Physical Review D*, 58(9):096007, 1998.

[63] O Scavenius, A Mocsy, IN Mishustin, and DH Rischke. Chiral phase transition within effective models with constituent quarks. *Physical Review C*, 64(4):045202, 2001.

[64] Nikos G Antoniou and AS Kapoyannis. Bootstraping the qcd critical point. *Physics Letters B*, 563(3-4):165–172, 2003.

[65] Yoshitaka Hatta and Takashi Ikeda. Universality, the qcd critical and tricritical point, and the quark number susceptibility. *Physical Review D*, 67(1):014028, 2003.

[66] Philippe De Forcrand and Owe Philipsen. The chiral critical line of nf= 2+ 1 qcd at zero and non-zero baryon density. *Journal of High Energy Physics*, 2007(01):077, 2007.

[67] Z Fodor and SD Katz. The phase diagram of quantum chromodynamics. *arXiv preprint arXiv:0908.3341*, 2009.

[68] Jana Günther, Rene Bellwied, Szabolcs Borsanyi, Zoltan Fodor, Sandor D Katz, Attila Pasztor, and Claudia Ratti. The qcd equation of state at finite density from analytical continuation. In *EPJ Web of Conferences*, volume 137, page 07008. EDP Sciences, 2017.

[69] Harvey Meyer. Lattice qcd at finite density and temperature. In *Sixth International Conference on Quarks and Nuclear Physics*, volume 157, page 009. SISSA Medialab, 2012.

[70] Jean Cleymans, Helmut Oeschler, K Redlich, and S Wheaton. Comparison of chemical freeze-out criteria in heavy-ion collisions. *Physical Review C*, 73(3):034905, 2006.

[71] M Cheng, P Hegde, C Jung, Frithjof Karsch, Olaf Kaczmarek, Edwin Laermann, RD Mawhinney, C Miao, P Petreczky, Christian Schmidt, et al. Baryon number, strangeness, and electric charge fluctuations in qcd at high temperature. *Physical Review D*, 79(7):074505, 2009.

[72] MM Aggarwal, Z Ahammed, AV Alakhverdyants, I Alekseev, BD Anderson, D Arkhipkin, GS Averichev, J Balewski, LS Barnby, S Baumgart, et al. An experimental exploration of the qcd phase diagram: the search for the critical point and the onset of de-confinement. *arXiv preprint arXiv:1007.2613*, 2010.

[73] Michael Mitrovski, NA49 Collaboration, et al. Recent results on strangeness production from na49. *Journal of Physics G: Nuclear and Particle Physics*, 37(9):094003, 2010.

[74] BI Abelev, MM Aggarwal, Z Ahammed, BD Anderson, D Arkhipkin, GS Averichev, J Balewski, O Barannikova, LS Barnby, J Baudot, et al. K/π fluctuations at relativistic energies. *Physical review letters*, 103(9):092301, 2009.

[75] Ashish Pandav, Debasish Mallick, and Bedangadas Mohanty. Effect of limited statistics on higher order cumulants measurement in heavy-ion collision experiments. *Nuclear Physics A*, 991:121608, 2019.

[76] A Bazavov, H-T Ding, P Hegde, Olaf Kaczmarek, Frithjof Karsch, Edwin Laermann, Swagato Mukherjee, Hiroshi Ohno, P Petreczky, E Rinaldi, et al. Skewness and kurtosis of net baryon-number distributions at small values of the baryon chemical potential. *Physical Review D*, 96(7):074510, 2017.

[77] A Bazavov, H-T Ding, P Hegde, Olaf Kaczmarek, Frithjof Karsch, Edwin Laermann, Y Maezawa, Swagato Mukherjee, H Ohno, P Petreczky, et al. Qcd equation of state to o (μ b 6) from lattice qcd. *Physical Review D*, 95(5):054504, 2017.

[78] J Adam, L Adamczyk, JR Adams, JK Adkins, G Agakishiev, MM Aggarwal, Z Ahammed, I Alekseev, DM Anderson, A Aparin, et al. Net-proton number fluctuations and the quantum chromodynamics critical point. *arXiv preprint arXiv:2001.02852*, 2020.

[79] MA Stephanov. Non-gaussian fluctuations near the qcd critical point. *Physical review letters*, 102(3):032301, 2009.

[80] Masayuki Asakawa, Shinji Ejiri, and Masakiyo Kitazawa. Third moments of conserved charges as probes of qcd phase structure. *Physical review letters*, 103(26):262301, 2009.

[81] RV Gavai and Sourendu Gupta. Lattice qcd predictions for shapes of event distributions along the freezeout curve in heavy-ion collisions. *Physics Letters B*, 696(5):459–463, 2011.

[82] Marcus Bleicher, E Zabrodin, Christian Spieles, Steffen A Bass, Christoph Ernst, Sven Soff, L Bravina, Mohamed Belkacem, Henning Weber, Horst Stöcker, et al. Relativistic hadron-hadron collisions in the ultra-relativistic quantum molecular dynamics model. *Journal of Physics G: Nuclear and Particle Physics*, 25(9):1859, 1999.

[83] P Garg, DK Mishra, PK Netrakanti, B Mohanty, AK Mohanty, BK Singh, and N Xu. Conserved number fluctuations in a hadron resonance gas model. *Physics Letters B*, 726(4-5):691–696, 2013.

[84] MA Stephanov. Evolution of fluctuations near qcd critical point. *Physical Review D*, 81(5):054012, 2010.

[85] Marlene Nahrgang, Stefan Leupold, Christoph Herold, and Marcus Bleicher. Nonequilibrium chiral fluid dynamics including dissipation and noise. *Physical Review C*, 84(2):024912, 2011.

[86] M Stephanov and Y Yin. Hydrodynamics with parametric slowing down and fluctuations near the critical point. *Physical Review D*, 98(3):036006, 2018.

[87] Marlene Nahrgang, Marcus Bluhm, Thomas Schäfer, and Steffen A Bass. Diffusive dynamics of critical fluctuations near the qcd critical point. *Physical Review D*, 99(11):116015, 2019.

[88] R Bellwied, Szabolcs Borsányi, Zoltán Fodor, J Günther, SD Katz, C Ratti, and KK Szabo. The qcd phase diagram from analytic continuation. *Physics Letters B*, 751:559–564, 2015.

[89] Akihiko Monnai, Swagato Mukherjee, and Yi Yin. Phenomenological consequences of enhanced bulk viscosity near the qcd critical point. *Physical Review C*, 95(3):034902, 2017.

[90] Gabriel S Denicol, Charles Gale, Sangyong Jeon, Akihiko Monnai, Björn Schenke, and Chun Shen. Net-baryon diffusion in fluid-dynamic simulations of relativistic heavy-ion collisions. *Physical Review C*, 98(3):034916, 2018.

[91] J Steinheimer, S Schramm, and H Stöcker. An effective chiral hadron–quark equation of state. *Journal of Physics G: Nuclear and Particle Physics*, 38(3):035001, 2011.

[92] Jussi Auvinen, Jonah E Bernhard, Steffen A Bass, and Iurii Karpenko. Investigating the collision energy dependence of η/s in the beam energy scan at the bnl relativistic heavy ion collider using bayesian statistics. *Physical Review C*, 97(4):044905, 2018.

[93] Fernando G Gardim, Frédérique Grassi, Pedro Ishida, Matthew Luzum, Pablo S Magalhães, and Jacquelyn Noronha-Hostler. Sensitivity of observables to coarse-graining size in heavy-ion collisions. *Physical Review C*, 97(6):064919, 2018.

[94] Szabolcs Borsanyi, Gergely Endrődi, Zoltan Fodor, Antal Jakovac, Sandor D Katz, Stefan Krieg, Claudia Ratti, and Kalman K Szabo. The qcd equation of state with dynamical quarks. *Journal of High Energy Physics*, 2010(11):77, 2010.

[95] Szabolcs Borsányi, Zoltan Fodor, Christian Hoelbling, Sandor D Katz, Stefan Krieg, and Kalman K Szabo. Full result for the qcd equation of state with 2+ 1 flavors. *Physics Letters B*, 730:99–104, 2014.

[96] Alexei Bazavov, Tanmoy Bhattacharya, Carleton DeTar, H-T Ding, Steven Gottlieb, Rajan Gupta, P Hegde, UM Heller, Frithjof Karsch, Edwin Laermann, et al. Equation of state in (2+ 1)-flavor qcd. *Physical Review D*, 90(9):094503, 2014.

[97] Szabolcs Borsányi, Z Fodor, J Guenther, K-H Kampert, SD Katz, T Kawanai, TG Kovacs, SW Mages, A Pasztor, F Pittler, et al. Calculation of the axion mass based on high-temperature lattice quantum chromodynamics. *Nature*, 539(7627):69–71, 2016.

[98] CR Allton, S Ejiri, SJ Hands, Olaf Kaczmarek, Frithjof Karsch, Edwin Laermann, Ch Schmidt, and L Scorzato. Qcd thermal phase transition in the presence of a small chemical potential. *Physical Review D*, 66(7):074507, 2002.

[99] CR Allton, M Döring, S Ejiri, SJ Hands, Olaf Kaczmarek, Frithjof Karsch, Edwin Laermann, and K Redlich. Thermodynamics of two flavor qcd to sixth order in quark chemical potential. *Physical Review D*, 71(5):054508, 2005.

[100] RV Gavai and Sourendu Gupta. Qcd at finite chemical potential with six time slices. *Physical Review D*, 78(11):114503, 2008.

[101] Subhasish Basak, Alexei Bazavov, Claude Bernard, Carleton DeTar, Walter Freeman, Steven Gottlieb, Urs M Heller, JE Hetrick, John Laiho, Ludmila Levkova, et al. Qcd equation of state at non-zero chemical potential. *arXiv preprint arXiv:0910.0276*, 2009.

[102] Olaf Kaczmarek, Frithjof Karsch, Edwin Laermann, C Miao, Swagato Mukherjee, Peter Petreczky, Christian Schmidt, Wolfgang Söldner, and Wolfgang Unger. Phase boundary for the chiral transition in (2+ 1)-flavor qcd at small values of the chemical potential. *Physical Review D*, 83(1):014504, 2011.

[103] Sz Borsanyi, G Endrődi, Zoltán Fodor, SD Katz, S Krieg, C Ratti, and KK Szabo. Qcd equation of state at nonzero chemical potential: continuum results with physical quark masses at order μ 2. *Journal of High Energy Physics*, 2012(8):53, 2012.

[104] Prasad Hegde, BNL-Bielefeld-CCNU Collaboration, et al. The qcd equation of state to o (μb4) from lattice qcd. *Nuclear Physics A*, 931:851–855, 2014.

[105] Massimo DElia, Giuseppe Gagliardi, and Francesco Sanfilippo. Higher order quark number fluctuations via imaginary chemical potentials in n f= 2+ 1 qcd. *Physical Review D*, 95(9):094503, 2017.

[106] Peter Braun-Munzinger, Johanna Stachel, and Christof Wetterich. Chemical freeze-out and the qcd phase transition temperature. *Physics Letters B*, 596(1-2):61–69, 2004.

[107] Chiho Nonaka and Masayuki Asakawa. Hydrodynamical evolution near the qcd critical end point. *Physical Review C*, 71(4):044904, 2005.

[108] Burkhard Kampfer, M Bluhm, H Schade, R Schulze, and D Seipt. Do we know eventually p (e)? *arXiv preprint arXiv:0708.3322*, 2007.

[109] Riccardo Guida and Jean Zinn-Justin. 3d ising model: the scaling equation of state. *Nuclear Physics B*, 489(3):626–652, 1997.

[110] P Schofield, JD Litster, and John T Ho. Correlation between critical coefficients and critical exponents. *Physical Review Letters*, 23(19):1098, 1969.

[111] JJ Rehr and ND Mermin. Revised scaling equation of state at the liquid-vapor critical point. *Physical Review A*, 8(1):472, 1973.

[112] Paolo Cea, Leonardo Cosmai, and Alessandro Papa. Critical line of 2+ 1 flavor qcd: Toward the continuum limit. *Physical Review D*, 93(1):014507, 2016.

[113] Claudio Bonati, Massimo DElia, Marco Mariti, Michele Mesiti, Francesco Negro, and Francesco Sanfilippo. Curvature of the chiral pseudocritical line in qcd: Continuum extrapolated results. *Physical Review D*, 92(5):054503, 2015.

[114] R Bellwied, S Borsanyi, Z Fodor, SD Katz, A Pasztor, C Ratti, and KK Szabo. Fluctuations and correlations in high temperature qcd. *Physical Review D*, 92(11):114505, 2015.

[115] Szabolcs Borsanyi, Zoltan Fodor, Sandor D Katz, Stefan Krieg, Claudia Ratti, and Kálman Szabó. Fluctuations of conserved charges at finite temperature from lattice qcd. *Journal of High Energy Physics*, 2012(1):138, 2012.

[116] Paolo Alba, Rene Bellwied, Szabolcs Borsányi, Zoltan Fodor, Jana Günther, Sandor D Katz, Valentina Mantovani Sarti, Jacquelyn Noronha-Hostler, Paolo Parotto, Attila Pasztor, et al. Constraining the hadronic spectrum through qcd thermodynamics on the lattice. *Physical Review D*, 96(3):034517, 2017.

[117] Tanmoy Bhattacharya, Michael I Buchoff, Norman H Christ, H-T Ding, Rajan Gupta, Chulwoo Jung, Frithjof Karsch, Zhongjie Lin, RD Mawhinney, Greg McGlynn, et al. Qcd phase transition with chiral quarks and physical quark masses. *Physical review letters*, 113(8):082001, 2014.

[118] The code on which this work is based can be downloaded at. `https://www.bnl.gov/physics/best/resources.php`, 2018.

[119] Stefan Floerchinger and Mauricio Martinez. Fluid dynamic propagation of initial baryon number perturbations on a bjorken flow background. *Physical Review C*, 92(6):064906, 2015.

[120] Paolo Parotto, Marcus Bluhm, Debora Mroczek, Marlene Nahrgang, J Noronha-Hostler, Krishna Rajagopal, Claudia Ratti, Thomas Schäfer, and Mikhail Stephanov. Qcd equation of state matched to lattice data and exhibiting a critical point singularity. *Physical Review C*, 101(3):034901, 2020.

[121] P Braun-Munzinger, A Rustamov, and J Stachel. Bridging the gap between event-by-event fluctuation measurements and theory predictions in relativistic nuclear collisions. *Nuclear Physics A*, 960:114–130, 2017.

[122] Xiaofeng Luo, Bedangadas Mohanty, and Nu Xu. Baseline for the cumulants of net-proton distributions at star. *Nuclear Physics A*, 931:808–813, 2014.

[123] Szabolcs Borsanyi, Zoltan Fodor, Jana N Guenther, Sandor K Katz, Attila Pasztor, Israel Portillo, Claudia Ratti, and KK Szabó. Higher order fluctuations and correlations of conserved charges from lattice qcd. *Journal of High Energy Physics*, 2018(10):205, 2018.

[124] Claudia Ratti. Lattice qcd and heavy ion collisions: a review of recent progress. *Reports on Progress in Physics*, 81(8):084301, 2018.

[125] Renato Critelli, Jorge Noronha, Jacquelyn Noronha-Hostler, Israel Portillo, Claudia Ratti, and Romulo Rougemont. Critical point in the phase diagram of primordial quark-gluon matter from black hole physics. *Physical Review D*, 96(9):096026, 2017.

[126] MA Stephanov. Sign of kurtosis near the qcd critical point. *Physical review letters*, 107(5):052301, 2011.

[127] Maneesha Sushama Pradeep and Mikhail Stephanov. Universality of the critical point mapping between ising model and qcd at small quark mass. *Physical Review D*, 100(5):056003, 2019.